Control of Magnetic Behavior in Molecular Clathrate based on Metal-organic Framework

芳野, 遼

https://hdl.handle.net/2324/4495996

出版情報：Kyushu University, 2021, 博士（理学）, 課程博士
バージョン：

Control of Magnetic Behavior in Molecular Clathrate based on Metal−organic Framework

Haruka Yoshino

September, 2021

Department of Chemistry

Graduate School of Science

Kyushu University

Contents

General Introduction

1. Porous Coordination Polymers (PCPs) or Metal-Organic Frameworks (MOFs)

Coordination polymers (CPs) with infinite coordination structures consist of organic/inorganic ligands and metal ions. CPs have been studied since the early 1960s.$^{1–3}$ The ordering framework and porous structure of the CPs have attracted attention from research fields involving molecular magnets and porous materials. Recently, crystalline porous materials, such as porous coordination polymers (PCPs) or metal–organic frameworks (MOFs), have attracted much attention in the fields of materials science, industrial science, and crystal engineering. MOFs are synthesized by the self-assembly of metal ions or clusters as versatile nodes and organic ligands as bridging linkers; they exhibit a variety of physical and chemical properties based on their component properties and periodically ordered porous structures (Fig. 1). Moreover, the number of studies on MOFs has rapidly increased in this decade owing to their potential for applications (e.g., storage, separation, and catalysis).$^{4–9}$ MOFs possess various characteristics: (i) structural diversity based on the combination of ligand binding direction and metal ion geometry; (ii) simple synthesis by self-assembly; (iii) the regular, designable, and flexible framework mainly composed of coordination bonds using host–guest interactions, for example, hydrogen and metal–metal bonds, π–π, CH–π, van del Waals, and electrostatic interactions; (iv) the reversible conversion of structure in response to guest uptake and release; and (v) the physical and chemical properties of the framework.

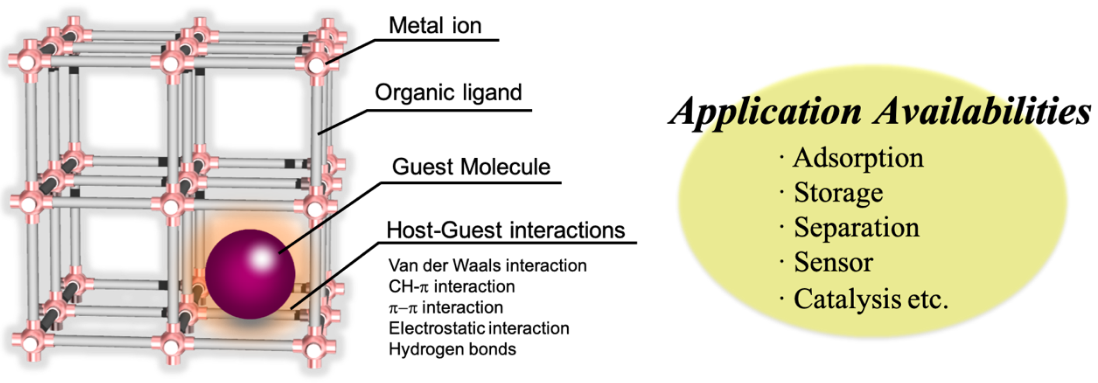

Fig. 1 Schematic illustration of metal-organic frameworks (MOFs) and their application abilities

2. Magnetic Ordering in MOFs

In the late 1980s, a rational synthetic strategy for molecular magnets assembled with paramagnetic molecules was presented.[10,11] Long-range magnetic ordering was achieved by the formation of the desired assembled structure by arranging paramagnetic centers using the appropriate bridging ligands for a magnetic exchange interaction. Because magnetic ordering is a three-dimensional (3D) phenomenon, it is essential to design a framework to propagate the 3D magnetic interaction. After establishing the basic synthetic strategy, in the late 1990s, Kahn and co-workers found that some molecular magnets exhibited drastic changes in structure and magnetic behavior due to the adsorption/desorption of water.[12,13] These guest-responsive magnetic materials are named "*molecular magnetic sponge*." Subsequently, molecular magnets were developed into multifunctional materials that exhibited magnetic properties and porosity. Several rational designs of magnetic MOFs with regular pores have been suggested, and the number of the designs has increased in the past few years, *e.g.,* Prussian blue analog $Co^{II}_3[Cr^{III}(CN)_6]_2{\cdot}nH_2O$ (Fig. 2),[14] $\{[Cu_3(ptmtc)_2(py)_6(EtOH)_2(H_2O)]\}$ (ptmtc = polychlorinated triphenylmethyl tricarboxylic acid radical),[15] $[Ni(dipn)]_3[Fe(CN)_6]_2{\cdot}12H_2O$ (dipn = *N*,*N*-di(3-aminopropyl)amine).[16] These MOFs exhibit reversible magnetic switching in response to desolvation/resolvation and can be developed to produce guest-responsive switching in sensory and memory devices.[17,18]

One of the rational strategies for the formation of porous magnets is based on a framework that provides paramagnetic centers located on the sides and corners of the inner pore, where the side and corner correspond to a connector and linker for the framework, respectively. From this viewpoint, the hexacyanometalate anion, $[M(CN)_6]^{n-}$, is a suitable linker because it provides a relatively long side (ca. 10 Å) for the inner pore and forms monodentate cyanide bridges for effective magnetic interaction and structural flexibility. Ohba and Ōkawa et al reported the first Ni(II)–Fe(III)$(CN)_6$ molecular magnet: $\{[Ni(en)_2]_3[Fe(CN)_6]_2{\cdot}2H_2O\}$ (en = ethylenediamine). This compound was prepared by reacting $[Ni(en)_2Cl_2]$ and $K_3[Fe(CN)_6]$ in water and was identified as a paramagnet based on zero-field-cooled and field-cooled magnetization measurements.[19,20] The molecular magnets derived from $[Ni^{II}(di/triamine)_2]^{2+}$ and $[Fe^{III}(CN)_6]^{3-}$ have been rationally synthesized, and their magnetic nature has been evaluated (Fig. 3)[19–24]

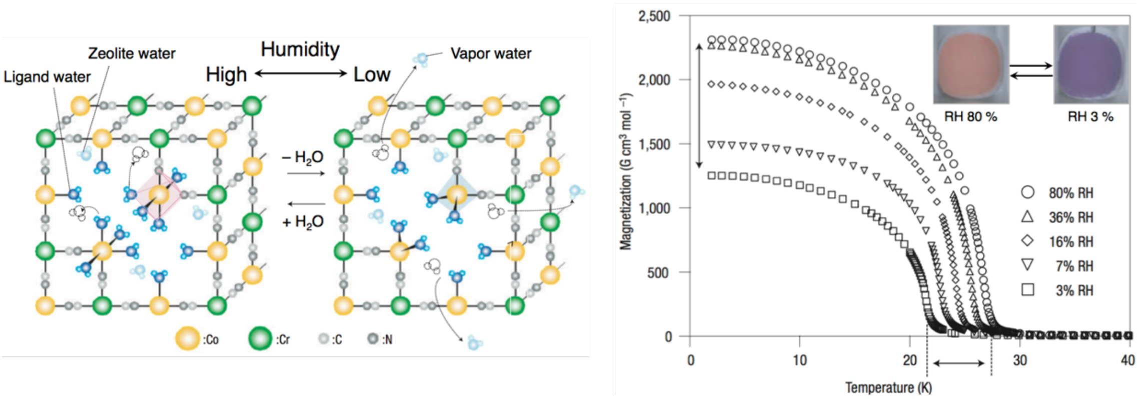

Fig. 2. Schematic variation of Co^{II} coordination geometry in Co$^{II}_3$[Cr^{III}(CN)$_6$]$_2$ between six- and four-coordinate in response to the adsorption and desorption of water molecules on the CoN$_2$O$_4$ coordination motif and their sample color; magnetization curves.[14]

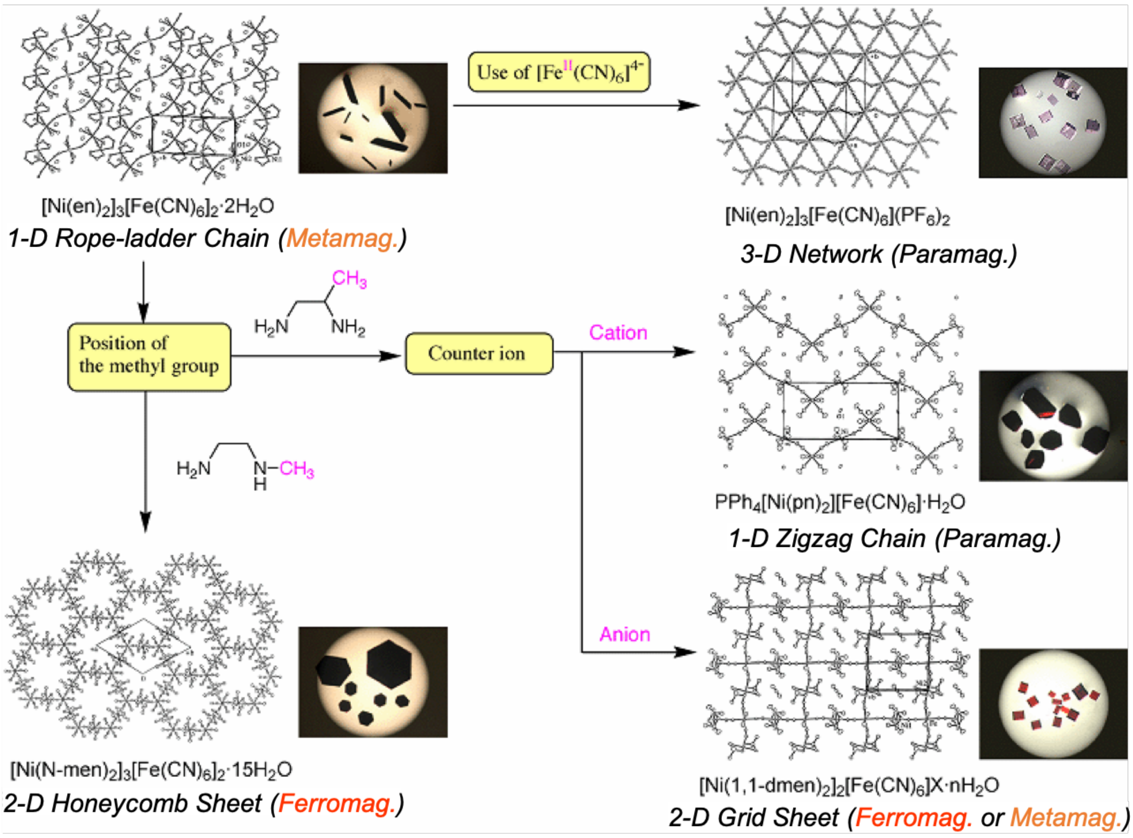

Fig. 3. Rational synthesis of the molecular magnets derived from [Ni^{II}(di/triamine)$_2$]$^{2+}$ and [Fe^{III}(CN)$_6$]$^{3-}$.[19–24]

3. Spin crossover (SCO) in MOFs

Magnetic-switchable materials have attracted considerable interest because of their potential applications as memory and sensor devices, etc., using interchangeable states.[25] Spin crossover (SCO) behavior is one of the fascinating phenomena that was first reported in 1931.[26] The SCO behavior is exhibited by $3d^4$–$3d^7$ metal complexes: they can exist in two different switchable spin states driven by external stimuli, such as temperature, pressure, light irradiation, and magnetic fields.[27–30] The SCO phenomenon is explained based on ligand field theory.[31,32] In Fe^{II} ($3d^6$) compounds in octahedral geometry, the electron configuration can be switched between paramagnetic high-spin (HS, $t_{2g}^4e_g^2$, and S = 2) and diamagnetic low-spin (LS, $t_{2g}^6e_g^0$, and S = 0) states (Fig. 4(a)). Importantly, the difference in the zero-point energies for the HS and LS states ($\Delta E^0_{HL} = E^0_{HS} - E^0_{LS}$) can be located within a range of thermal energies if the ligand field is appropriate. Hence, MOFs with infinite coordination structures are suitable candidates to obtain strong cooperativity because their structural tunability involving various host–guest interactions, such as π–π interactions and hydrogen bonding, can be incorporated into the framework.

Additionally, the effective propagation of spin-state change in solids, i.e., the high cooperativity of SCO-active materials, is primarily governed by elastic interactions between the spin-state-switchable metal ions through linker ligands and the packing structure. Compared with discrete metal complexes, MOFs have the potential to be a good platform for SCO materials with high cooperativity using an infinite framework structure. Additionally, the systematic modification capability of the components is another advantage for developing various compounds. Therefore, the rational choice of ligands is an important factor in designing SCO-MOFs with desirable switchable magnetic behavior. Thus far, many SCO-MOFs have been developed, in which the magnetic properties are influenced by temperature, pressure, and guest molecules. For instance, Kepert and co-workers reported that $\{Fe_2(azpy)_4(NCS)_4\cdot guest\}$ (azpy = *trans*-4,4'-azopyridine) displayed SCO behaviors followed by the reversible exchange of guest molecules adsorbed through hydrogen bonds with the framework. This was the first example of the modulation of the SCO behavior in MOFs with guest adsorption.[33] Furthermore, enhanced cooperativity sometimes affords an abrupt spin transition (ST) and a magnetically bistable property (e.g., hysteresis phenomenon; Fig. 4(b)).[31] O. Kahn and co-workers reported the design of a molecular material showing a hysteresis loop around the room temperature using $\{[Fe(Htrz)_3](ClO_4)_2\}$ (Htrz = 1,2,4-1H-triazole; Fig. 5).[34]

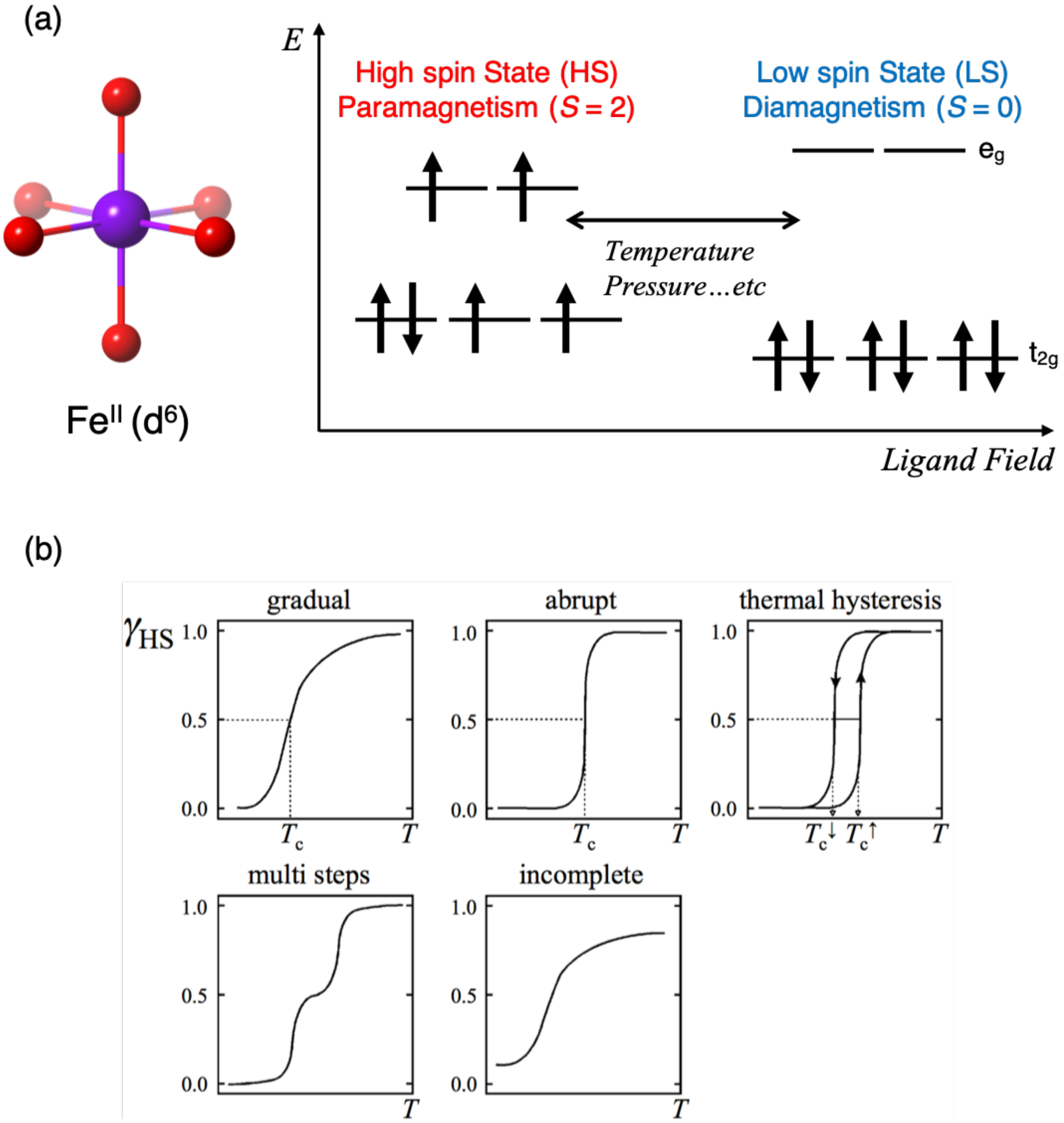

Fig. 4(a) Electronic configurations of d^6 transition metal with octahedral geometry in the HS and LS states. (b) Schematic illustration of SCO behaviors. The horizontal axis shows the temperature, and the vertical axis shows the fraction of the HS states.[31]

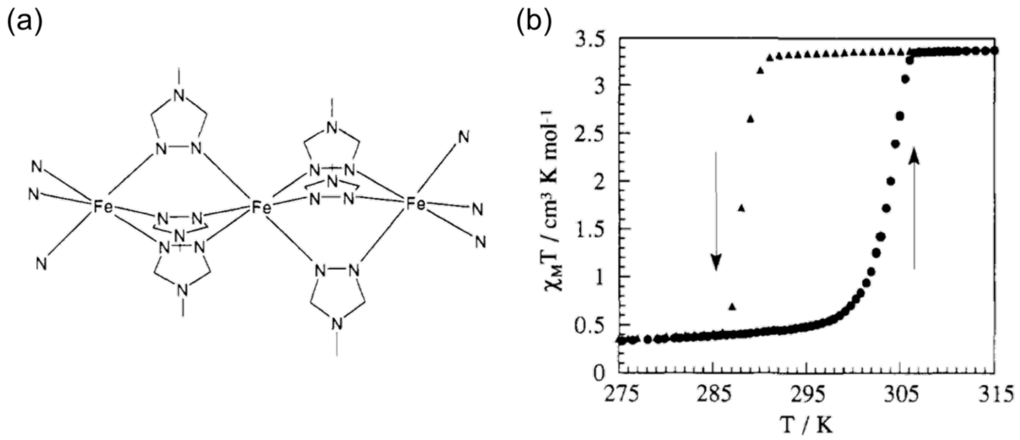

Fig. 5(a) Schematic Structure of $[Fe(Htrz)_3](ClO_4)_2$. (b) $\chi_M T$ *vs* T plots for $[Fe(H\text{-}trz)_{2.85}(NH_2\text{-}trz)_{0.15}](ClO_4)_2$ in both the warming (●) and cooling (▲) modes.[34]

Hofmann-type MOFs are one of the best-known and studied SCO-potential systems with a regular infinite-coordination structure. The first Hofmann-type compound, $\{Ni(NH_3)_2[Ni(CN)_4]\cdot Guest\}$, was reported by Hofmann and Küspert in 1897; the compound can accommodate guest molecules that exist between the layers (Fig. 6(a)).[35–37] Moreover, the first Hofmann-type MOF showing SCO behavior, $\{Fe^{II}(py)_2[Ni^{II}(CN)_4]\}$ (py = pyridine), was reported by Kitazawa and co-workers in 1996 (Fig. 6(b)).[38] This MOF exhibited a cooperative SCO behavior with a thermal hysteresis width of 9 K ($T_c^{\uparrow}$= 186 K, $T_c^{\downarrow}$= 195 K). However, guest adsorption did not occur because of its closed packing structure with strong π–π stacking between axial pyridine co-ligands.

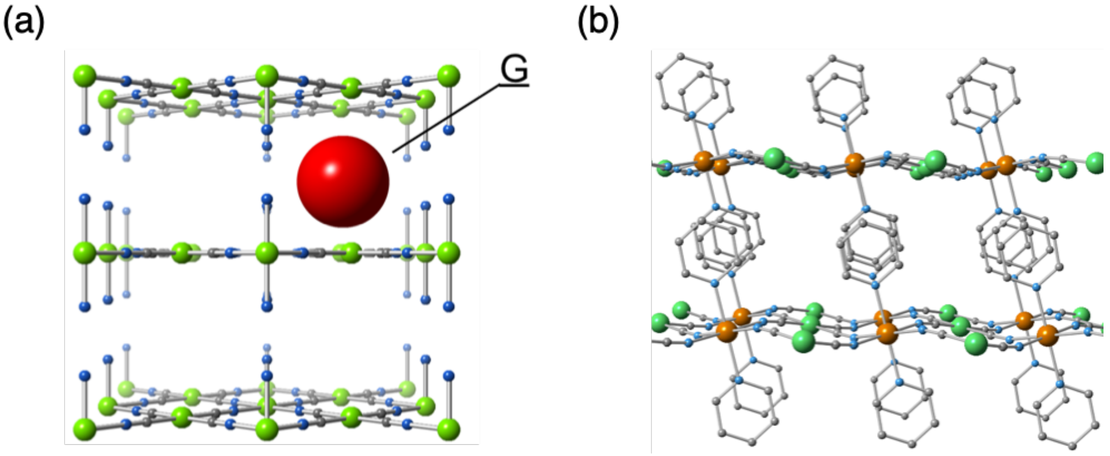

Fig. 6(a). Crystal structure of $\{Ni(NH_3)_2[Ni(CN)_4]\cdot 2G\}$ (G = benzene, pyrrole, thiophene, furan),[35–37] where C, N, Ni atoms are colored in gray, blue, and light green, respectively. (b) Crystal structure of $\{Fe(py)[Ni(CN)_4]\}$ (py = pyridine),[38] where C, N, Fe, Ni atoms are colored in gray, light blue, orange, and green, respectively.

Kepert and co-workers successfully coupled porosity and magnetic behavior using a flexible 2D Hofmann MOF: $\{Fe^{II}(bztrz)_2[Pd^{II}(CN)_4]\}$ (bztrz = (*E*)-1-phenyl-*N*-(1,2,4-triazol-4-yl)methanimine; Fig. 7).[39] The environment of Fe ions in the framework changed remarkably with guest adsorption, affording various magnetic properties, depending on the type and ratio of the guest molecules. However, the development of efficient guest-responsive magnetic MOFs remains challenging. There is a large temperature gap between the guest adsorption/desorption and ST temperature.

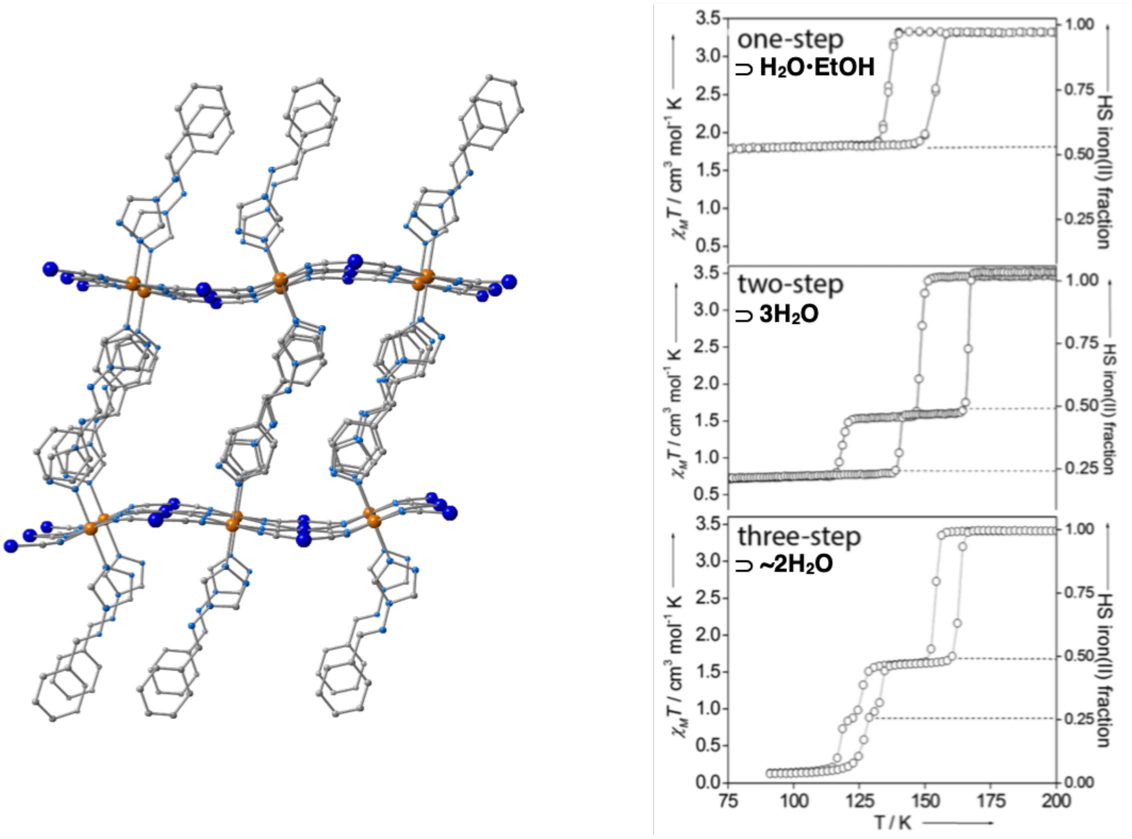

Fig. 7. Crystal structure of $\{Fe^{II}(bztrz)_2[Pd^{II}(CN)_4]\}$ and its guest-tunable magnetic behavior.[39]

To obtain a high ST temperature and porous function, a pillared-layer Hofmann-type MOF, {Fe(pz)[M(CN)$_4$]} (**1**; pz = pyrazine, M = Ni, Pd, Pt; Fig. 8(a)), was reported by Real and co-workers.[40] This 3D structure possesses 2D cyanide-bridged layers consisting of octahedral $Fe^{II}N_6$ and square-planar $[M(CN)_4]^{2-}$ units. The structural conversion of **1** between HS and LS induces a drastic change in the void space by over 30%. Moreover, the activated sample of **1** exhibits a cooperative spin transition ST at room temperature with a hysteresis of approximately 20 K at room temperature ($T_c^{\uparrow}$ = 304 K, $T_c^{\downarrow}$ = 285 K; Fig. 8(b)). The framework of **1** provides two guest-interactive sites in the pores (Fig. 9). One is the π–π interaction by pz as a pillar ligand, and the other is in the unsatisfied metal center of Pt, which is called "open metal sites" (OMS). These guest-interactive sites play an important role in the chemical response of **1**.

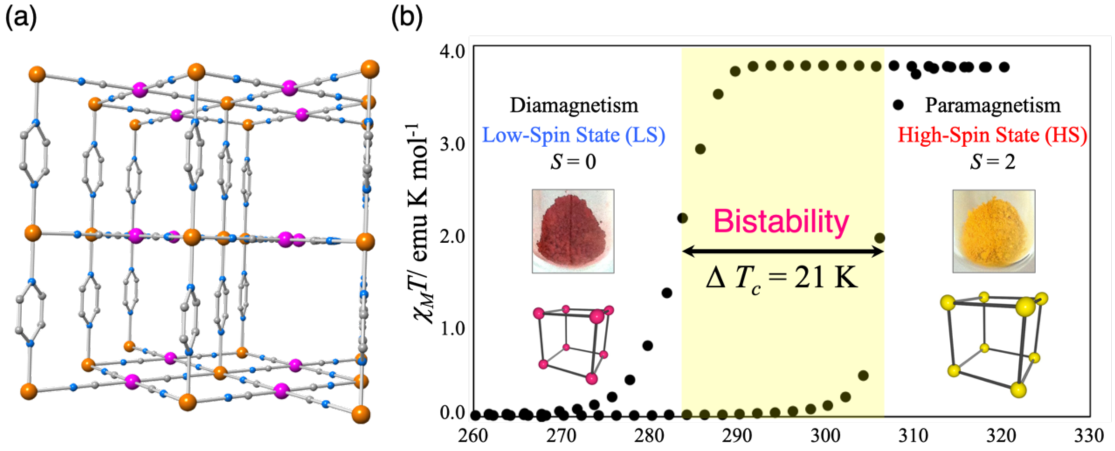

Fig. 8(a) Crystal structure of {Fe(pz)[Pt(CN)$_4$]} (**1**), where C, N, Fe, and Pt atoms are colored in gray, blue, orange, and purple, respectively. (b) Magnetic behavior of **1**.

Furthermore, Ohba and Real reported that **1** showed the reversible chemo-switching of the spin-state of Fe(II) coupled with guest adsorption.[41] Further, **1** exhibited reversible ST behavior with color changes between yellow (HS) and reddish purple (LS) in association with guest molecule adsorption at room temperature. In most cases, the framework of **1** was stabilized in the HS state, and the structure was expanded (e.g., benzene, toluene, alcohol, and five-membered-ring organic solvents). Conversely, CS_2, acrylonitrile (AcCN), and acetonitrile (CH_3CN) were stabilized in the LS state (Fig. 10). Due to the stimuli-responsive properties of **1**, it can be applied as a chemical sensor. The magnetic properties of **1** were modified through the uptake and release of liquid guest molecules; however, gaseous molecules, such as O_2, N_2, and CO_2, could not induce a change in the magnetic behavior because of the weak interaction with the framework.

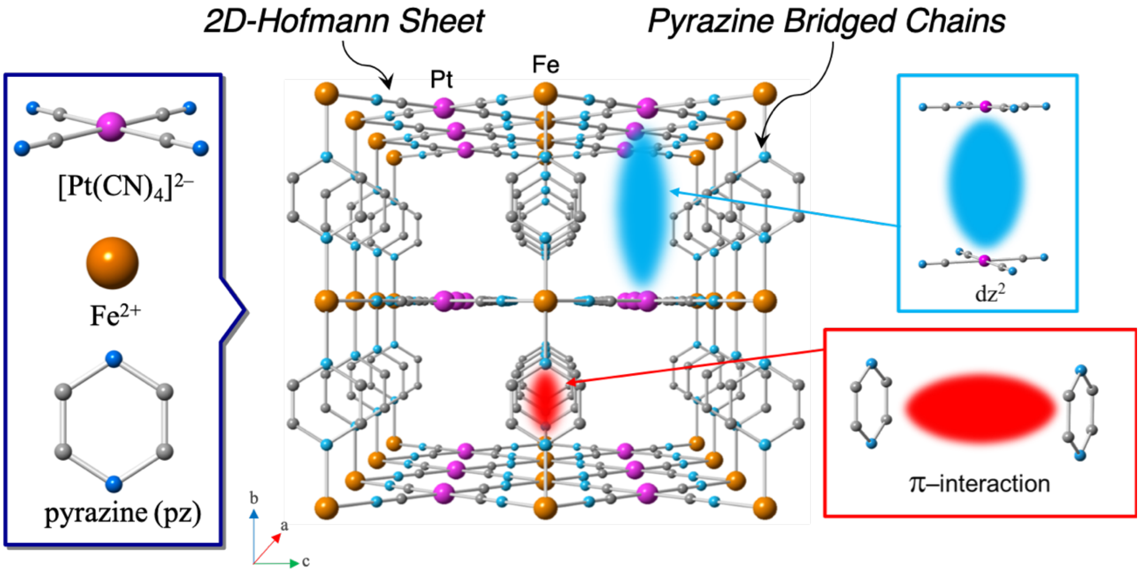

Fig. 9 Guest-interactive sites in **1**.

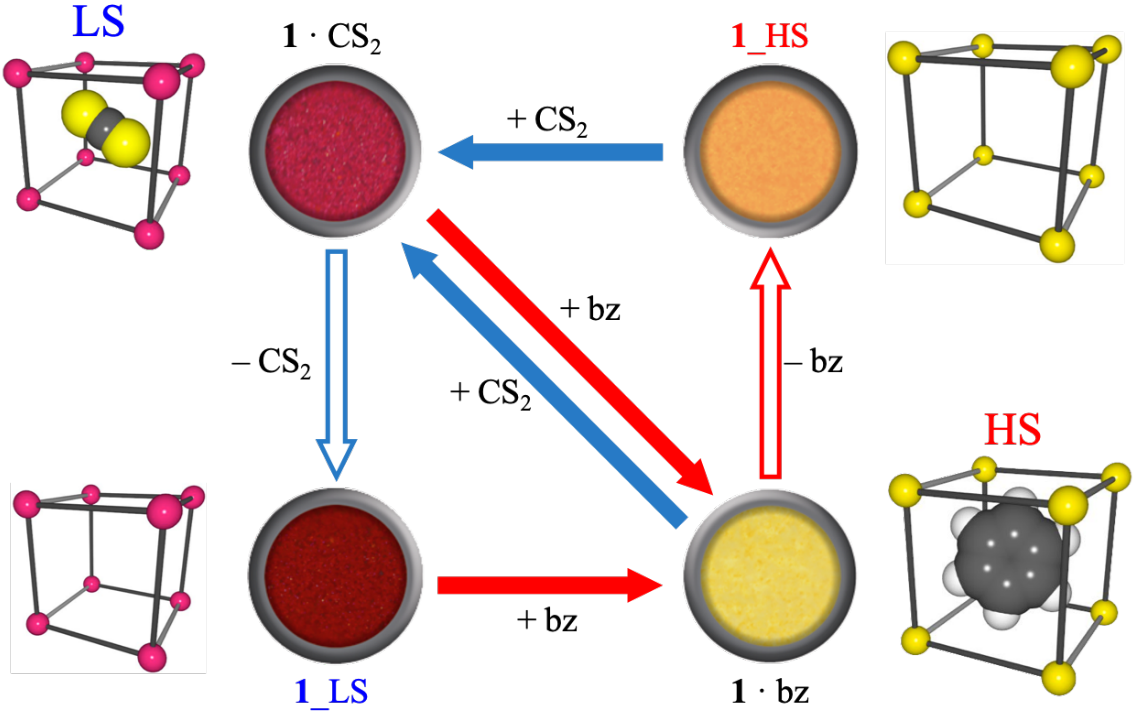

Fig. 10 Reversible chemo-switching of the spin state of **1** relating with guest adsorption and desorption.

4. Gas-responsive Magnetic MOFs

Chemo-switchable magnetic materials have attracted much attention because of their potential applications. Magnetic materials showing magnetic variability with guest molecules have been significantly investigated.[42–47] In particular, the development of highly sensing materials for gas molecules, such as carbon dioxide (CO_2), N_2, O_2, hydrocarbons, and carbon monoxide (CO), is one of the crucial challenges in the field of molecular science.[48–50] Several strategies for constructing gas-switchable magnetic materials have been explored.[51–54] For instance, Long et al. demonstrated that Fe_2Cl_2(bbta) (H_2bbta = 1*H*,5*H*- benzo(1,2-*d*:4,5-*d*)bistriazole) with unsaturated iron(ii) sites exhibited a spin-state transition driven by a threshold CO pressure, resulting in large CO separation capacities with only small changes in temperature (Fig. 11).[53]

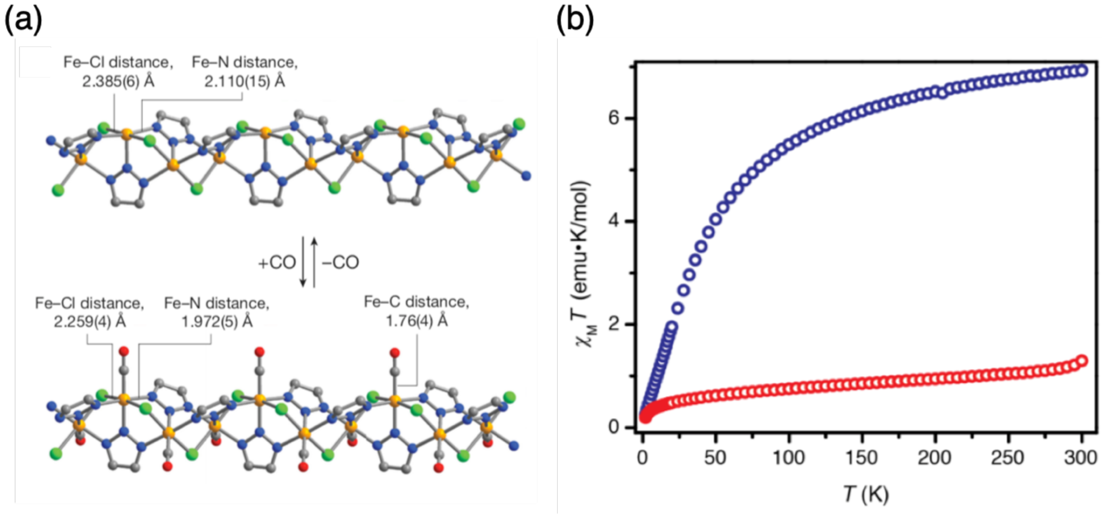

Fig. 11(a) Portions of the structures of Fe_2Cl_2(bbta) (upper) and the CO-adsorbed state of Fe_2Cl_2(bbta); the selected bond lengths are indicated. The grey, green, orange, blue, and red spheres represent C, Cl, Fe, N, and O atoms, respectively; H atoms are omitted for clarity. The numbers in parentheses are the estimated standard deviation in the final digit of each number. (b) $\chi_M T$ *vs* T plots collected for Fe_2Cl_2(bbta) (blue) and CO-adsorbed state of Fe_2Cl_2(bbta) (red) collected at 1 T.[53]

Miyasaka et al. successfully designed a CO_2-responsive MOF $[\{Ru_2(F_3PhCO_2)_4\}_2TCNQ(OEt)_2]\cdot 3DCM$ (F_3PhCO^{2-}, 2,4,6-trifluorobenzoate; DCM, dichloromethane) based on paddlewheel-type ruthenium(ii) dimers, as electron donors, coordinated in-plane to 2,5-diethoxy-7,7,8,8-tetracyanoquinodimethane ($TCNQ(OEt)_2$) units, as the electron acceptor. This porous magnet undergoes an in-plane electron transfer and a structural transition to adopt a paramagnetic form with CO_2 adsorption (Fig. 12).[54] An effective approach to induce a conversion in the magnetic phase is the manipulation of magnetic interaction in the framework through a drastic structural change and guest adsorption. However, establishing promising guidelines for the material design of gas molecules remains challenging at this stage because of the weak interaction with MOFs, as well as technical difficulties.

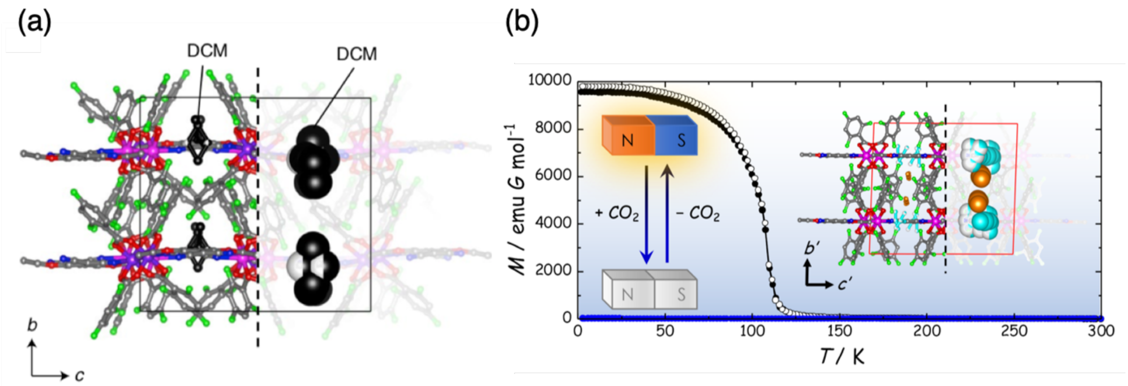

Fig. 12(a) Packing views of $\{Ru_2(F_3PhCO_2)_4\}_2TCNQ(OEt)_2]\cdot 3DCM$ along the *a* crystallographic axis. (b) The CO_2 pressure dependence of *M*–*T* curves at Hdc = 1 kOe for $[\{Ru_2(F_3PhCO_2)_4\}_2TCNQ(OEt)_2]$.[54]

5. Purpose of this research

The precise control of the magnetic properties of guest-responsive MOFs is of considerable importance in the development of novel functional molecular devices. Conventionally, external stimuli (*e.g.,* temperature, light, and pressure) have been employed to modulate the magnetic properties of the framework. We explored the conventional approach of manipulating the magnetic properties of the frameworks using their choice of structural components, such as metal ions and organic ligands. Furthermore, guest molecules are incorporated into the pores; they are used as a third component for controlling a range of magnetic behaviors. The MOFs that confined the guest molecules are called clathrates. The clathrates interact with the guest molecules through weak host–guest interactions (e.g., van der Walls interaction), and the degree of freedom for the motion of the guest molecules is partially maintained, significantly affecting the Gibbs free energy of the system, as an entropic contribution. The motion of the guest molecules and the host–guest interaction in such clathrates strongly depend on the type of molecule, density (number of guest molecules per pore), and external stimuli, such as temperature, pressure, and light. Therefore, the guest molecules should be a significant factor for controlling the functions and physical properties of the MOF-based clathrates. In other words, by confining the guest molecules, a potential function-controller is incorporated into the system, and a new degree of freedom is provided in the design of functional materials: novel clathrate systems.

The guest molecules in MOFs perform two important roles: (i) they work as a third component that changes the magnetic profiles of the host framework, (ii) they introduce chemical sensitivity to external stimuli to switch the spin states of the framework. The guest-adsorbed molecule clathrates often display guest-dependent magnetic behavior. The host–guest interactions operating in the clathrates influence the important factors that govern the entire magnetic property in the framework (*e.g.,* the magnetic interaction for porous magnets, ligand field strength of magnetic centers, and cooperativity of the frameworks). Notably, various guest factors, such as size, shape, flexibility, chemical properties, adsorbed amounts, and pore dynamics, induce guest-dependent magnetic behaviors, even when the same host framework is employed. Thus, the clarification of the correlation between the host–guest interactions and magnetic behaviors of the clathrates is a crucial challenge in the field of material engineering. Resultantly, novel host–guest systems with unprecedented magnetic behavior are designed.

Here, we summarize the current knowledge about the synergetic change in the magnetic behavior in molecular clathrates based on guest-responsive magnetic MOFs.

In Chapter 1, we discussed the rational design of cyanide-based amorphous MOFs and their coordination geometry changes involving amorphous–crystalline transformation upon water adsorption. The local symmetry of metal ions in amorphous MOFs was discussed based on $L_{2,3}$- and K-edge XAFS analyses and magnetic behavior (Fig. 13).[55]

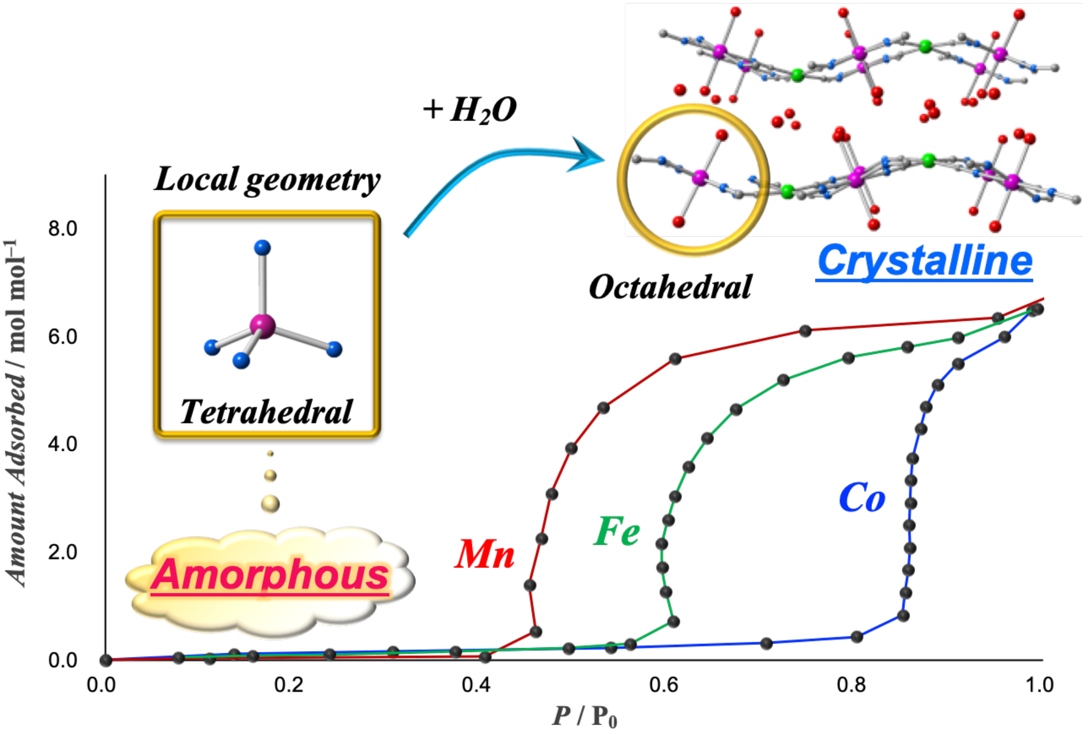

Fig. 13 Schematic illustration of the metal-tunable water adsorption behavior and reversible amorphous–crystalline transition along with the change in coordination geometry for central metal ions.

In Chapter 2, we describe the design of two types of flexible porous magnets that show magnetic phase switching via structural changes arising from guest adsorption/desorption. Dianions are employed as pillar ligands, leading to the guest-selective and multi-step guest adsorption behavior. Importantly, the entire magnetic phase of the framework is governed by interlayer magnetic interactions, which were manipulated by the threshold interlayer distance of approximately 10 Å (Fig. 14(a)).[56] Furthermore, we achieved CO_2-induced magnetic phase switching from antiferromagnetic to ferromagnetic phases using a novel double-layer-type porous magnet. The detailed magneto-structural correlation was investigated using various in-situ physical property measurements, and novel gas-responsive magnetic systems were designed (Fig. 14(b)).

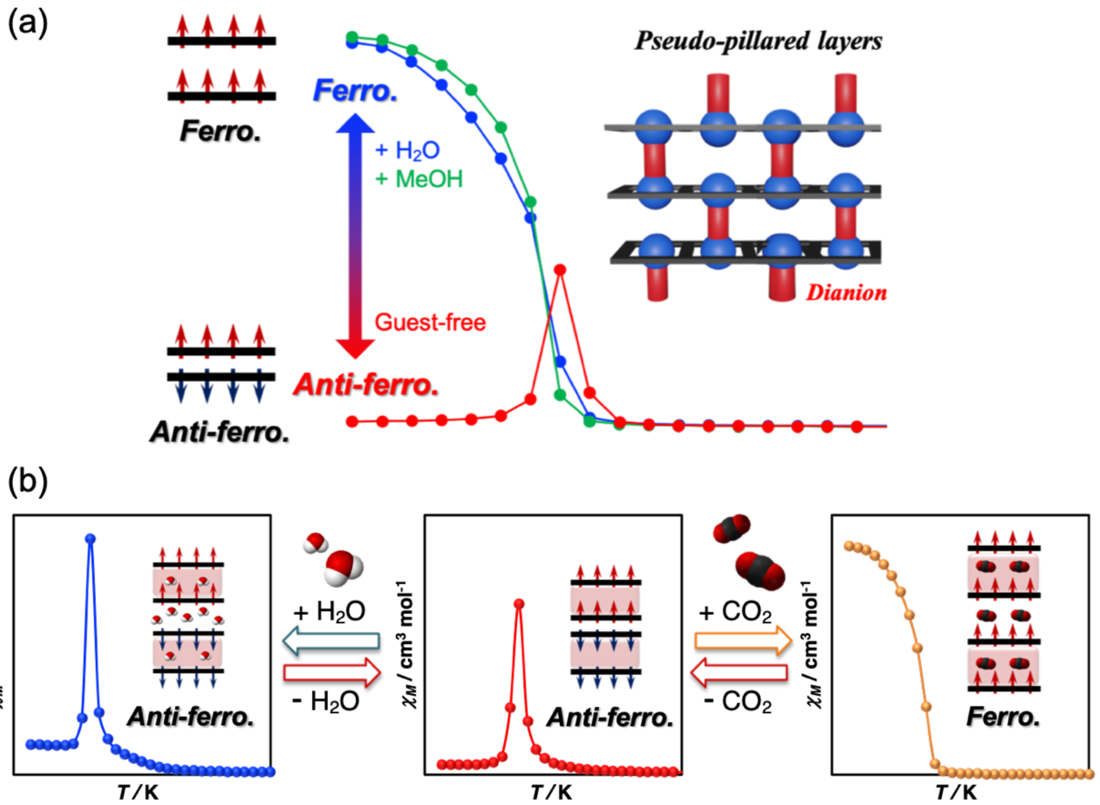

Fig. 14 (a) Schematic illustration of magnetic phase switching prompted by the changes in the interlayer distance arising from guest adsorption/desorption in a flexible porous magnet with pseudo-pillar-dianions. (b) Schematic illustration of CO_2-induced magnetic phase conversion in a double-layer-type porous magnet.

In Chapter 3, we successfully induced multi-step spin state changes and non-equilibrium state in alkane clathrate ($\mathbf{1}\supset C_nH_{2n+2}$; $n = 1-4$), based on a magnetically bistable Hofmann-type MOF {Fe(pz)[Pt(CN)$_4$]} (**1**). For $\mathbf{1}\supset C_2H_6$ and $\mathbf{1}\supset C_3H_8$, the $\chi_M T$ value decreased during the heating process. This might be caused by the change in the density of alkanes in the pore ($\mathbf{1}\supset C_2H_6$) and the existence of thermodynamically and kinetically stable phases governed by the scan rate for the magnetic measurement. Several mechanisms have been suggested to produce guest-switchable magnetic materials. However, to the best of our knowledge, there are no reports on achieving synergistic physical property changes induced by the dynamic behaviors of the guest molecules confined in the pores of MOFs. Therefore, our study provides new insights into the rational design of gas-responsive MOFs (Fig. 15).

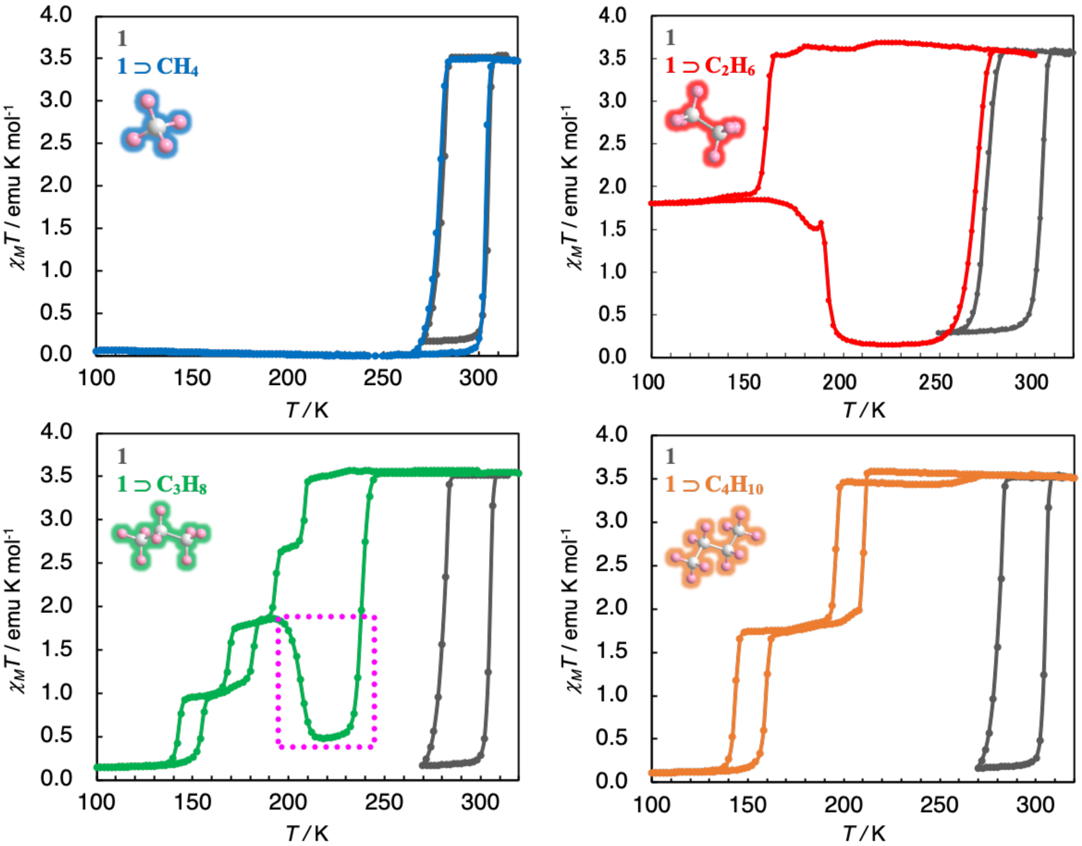

Fig. 15 Multiple spin state changes and non-equilibrium state in alkane clathrate based on {Fe(pz)[Pt(CN)$_4$]} (**1**).

References

1. S. Kitagawa, R. Kitaura, S. Noro, *Angew. Chem. Int. Ed.* 2004, **43**, 2334–2375.
2. Batten, S. R.; Robson, R., *Angew. Chem. Int. Ed.*, 1998, **37**, 1460−1494.
3. James, S. L., *Chem. Soc. Rev.*, 2003, **32**, 276−288.
4. S. Kitagawa, K. Uemura, *Chem. Soc. Rev.*, 2005, **34**, 109-119.
5. O. M. Yaghi, M. O'Keeffe, N. W. Ockwig, H. K. Chae, M. Eddaudi, J. Kim, *Nature*, 2003, **423**, 705-714.
6. J. L. C. Rowsell, O. M. Yaghi, *Micropor. Mesopor. Mater.*, 2004, **73**, 3-14.
7. M. O'Keeffe, M. Eddaoudi, H. Li, T. Reineke, O. M. Yaghi, *J. Solid State Chem.*, 2000, **152**, 3-20.
8. J. L. C. Rowsell, O. M. Yaghi, *Angew. Chem. Int. Ed.*, 2005, **44**, 4670-4679.
9. G. Férey, *Chem. Soc. Rev.*, 2008, **37**, 191-214.
10. S. R. Chittipeddi, J. S. Miller, H. Rommelmann, S. R. Chittipeddi, J. H. Zhang, W. M. Reiff, A. J. Epstein, *J. Am. Chem. Soc.*, 1987, **109**, 769−781.
11. A. Caneschi, D. Gatteschi, R. Sessoli, P. Rey, *Inorg. Chem.*, 1988, **27**, 1756−1761.
12. Kahn, O.; Larionova, J.; Yakhmi, J. V., *Chem. Eur. J.* 1999, **5**, 3443−3449.
13. Larionova, J.; Chavan, S. A.; Yakhmi, J. V.; Frøystein, A. G.; Sletten, J.; Sourisseau, C.; Kahn, O., *Inorg. Chem.*, 1997, **36**, 6374−6381.
14. S. Ohkoshi, K. Arai, Y. Sato, K. Hashimoto, *Nat. Mater.*, 2004, **3**, 857-861.
15. D. Maspoch, D. Ruiz-Molina, K. Wurst, N. Domingo, M. Cavallini, F. Biscarini, J. Tejada, C. Rovira, J. Veciana, *Nat. Mater.*, 2003, **2**, 190-195.
16. N. Yanai, W. Kaneko, K. Yoneda, M. Ohba, S. Kitagawa, *J. Am. Chem. Soc.*, 2007, **129**, 3496-3497.
17. O. Kahn, C. J. Martinez, *Science*, 1998, **279**, 44-48.
18. O. Kahn, J. Kröber, C. Jay, *Adv. Mater.*, 1992, **4**, 718-728.
19. M. Ohba, N. Maruono, H. Ōkawa, T. Enoki, and J.-M. Latour, *J. Am. Chem. Soc.*, 1994, **116**, 11566-11567.
20. C. -D. Wu, A. Hu, L. Zhang, and W. Lin, *J. Am. Chem. Soc.*, 2005, **127**, 8940-8941.
21. M. Ohba, K. Yoneda, and S. Kitagawa, *Cryst. Eng. Comm.*, 2010, **12**, 159-165.
22. M. Ohba, H. Ōkawa, *Coord. Chem. Rev.*, 2000, **198**, 313-328.
23. P. Dechambenoit and J. R. Long, *Chem. Soc. Rev.*, 2011, **40**, 3249-3265.
24. N. Usuki, M. Ohba, and H. Ōkawa, *Bull. Chem. Soc. Jpn.*, 2002, **75**, 1693-1698.
25. A. Bousseksou, G. Molnár, L. Salmon, W. Nicolazzi, *Chem. Soc. Rev.* 2011, **40**, 3313–3335.
26. L. Cambi, A., Cagnasso, *Atti. Accad. Naz. Lincei*, 1931, **13**, 809−813.

27. P. Gütlich, A. Hauser, H. Spiering, *Angew. Chem. Int. Ed. Engl.*, 1994, **33**, 2024-2054.
28. P. Gütlich, V. Ksenofontov, A. B. Gaspar, *Coord. Chem. Rev.*, 2005, **249**, 1811-1829.
29. S. Decurtins, P. Gütlich, P. C. Köhler, H. Spiering, A. Hauser, *Chem. Phys. Lett.*, 1984, **105**, 1-4.
30. A. Bousseksou, F. Varret, M. Goiran, K. Boukheddaden, J. P. Tuchagues, *Top. Curr. Chem.*, 2004, **235**, 65-84.
31. P. Gütlich, A. Hauser, H. Spiering, *Angew. Chem. Int. Ed.*, 1994, **33**, 2024−2054.
32. M. A. Halcrow, *Chem. Soc. Rev.*, 2011, **40**, 4119−4142.
33. G. J. Halder, C. J. Kepert, B. Moubaraki, K. S. Murray, J. D. Cashion, *Science*, 2002, **298**, 1762–1765.
34. J. Krober, E. Codjovi, O. Kahn, F. Groliere, C. Jay, *J. Am. Chem. Soc.*, 1993, **115**, 9810-9811.
35. K. A. Hofmann, F. A. Küspert , *Z. Anorg. Allg. Chem.,* 1897, **15**, 204-224.
36. H. M. Powell, J. H. Rayner, *Nature*, 1949, **163**, 566-567.
37. H. M. Powell, J. H. Rayner, *J. Chem. Soc.,* 1952, 319-328.
38. T. Kitazawa, Y. Gomi, M. Takahashi, M. Takeda, M. Enomoto, A. Miyazaki and T. Enoki, *J. Mater. Chem.,* 1996, *6*, 119-121.
39. M. J. Murphy, K. A. Zenere, F. Ragon, P. D. Southon, C. J. Kepert, S. M. Neville, *J. Am. Chem. Soc.*, 2017, **193**, 1330-1335.
40. V. Niel, J. M. Martinez-Agudo, M. C. Muñoz, A. B. Gaspar, and J. A. Real, *Inorg. Chem.*, 2001, **40**, 3838–3839.
41. M. Ohba, K. Yoneda, G. Agustí, M. C. Muñoz, A. B. Gaspar, J. A. Real, M. Yamasaki, H. Ando, Y. Nakao, S. Sakaki, S. Kitagawa, *Angew. Chem. Int. Ed.,* 2009, **48**, 4767-4771.
42. W. Kaneko, M. Ohba and S. Kitagawa, *J. Am. Chem. Soc.*, 2007, **129**, 13706–13712.
43. M. H. Zeng, Z; Yin, Y. Tan, W. X. Zhang, Y. P He, M. Kurmoo, *J. Am. Chem. Soc.*, 2014, **136**, 4680–4688.
44. J. Zhang, W. Kosaka, K. Sugimoto and H. Miyasaka, *J. Am. Chem. Soc.*, 2018, **140**, 5644–5652.
45. J. A. R. Navarro, E. Barea, A. R. Diéguez, J. M. Salas, C. O. Ania, J. B. Parra, N. Masciocchi, S. Galli, A. Sironi, *J. Am. Chem. Soc.*, 2008, **130**, 3978–3984.
46. E. D. Bloch, W. L. Queen, R. Krishna, J. M. Zadrozny, C. M. Brown, Jeffrey R. Long, *Science*, 2012, **335**, 1606–1610.
47. E. Coronado, M. G. marqués, G. M. Espallargas, L. Brammer, *Nat. Commun.*, 2012, **3**, 828.
48. T. M. McDonald, J. A. Mason, X. Kong, E. D. Bloch, D. Gygi, A. Dani, V. Crocella,

F. Giordanino, S. O. Odoh, W. Drisdell, B. Vlaisavljevich, A. L. Dzubak, R. Poloni, S. K. Schnell, N. Planas, K. Lee, T. Pascal, L. F. Wan, D. Prendergast, J. B. Neaton, B. Smit, J. B. Kortright, L. Gagliardi, S. Bordiga, J. A. Reimer, J. R. Long, *Nature*, 2015, **519**, 303–308.

49. S. Krause, V. Bon, I. Senkovska, U. Stoeck, D. Wallacher, D. M.Többens, S. Zander, R. S.Pillai, G. Maurin, F. X. Coudert, S. Kaskel, *Nature*, 2016, **532**, 348–352.
50. R. A. Potyrailo, *Chem. Rev*, 2016, **116**, 11877–11923.
51. W. Kosaka, Z. Liu, J. Zhang, Y. Sato, A. Hori, R. Matsuda, S. Kitagawa and H. Miyasaka, *Nat. Commun.*, 2018, **9**, 5420.
52. E. Coronado, M. Giménez-Marqués, G. Mínguez Espallargas, F. Rey and I. J. Vitórica-Yrezábal, *J. Am. Chem. Soc.*, 2013, **135**, 15986–15989.
53. D. A. Reed, B. K. Keitz, J. Oktawiec, J. A. Mason, T. Runčevski, D. J. Xiao, L. E. Darago, V. Crocellà, S. Bordiga, J. R. Long, *Nature*, 2017, **550**, 96–100.
54. J. Zhang W. Kosaka, Y. Kitagawa, H. Miyasaka, *Nat. Chem.*, 2021, **13**, 191-199.
55. H. Yoshino, K. Yamagami, H. Wadati, H. Yamagishi, H. Setoyama, S. Shimoda, A. Mishima, B. Le Ouay, R. Ohtani, M. Ohba, *Inorg. Chem.,* 2021, **60***,* 3338-3344.
56. H. Yoshino, N. Tomokage, A. Mishima, B. Le Ouay, R. Ohtani, W. Kosaka, H. Miyasaka, M. Ohba, *Chem. Commun.,* 2021 **57***,* 5211-5214.

Chapter 1

Coordination Geometry Changes in Amorphous Cyanide-bridged Metal−Organic Frameworks upon Water Adsorption

Abstract

Metal-organic frameworks (MOFs) with amorphous state have attracted much attention because of their various functionalities. Here, we report tunable water adsorption in a series of amorphous cyanide-bridged MOFs with different central metals ($M[Ni(CN)_4]$: **MNi**; M = Mn, Fe, Co). All the compounds adsorb up to six water molecules at a certain vapor pressure (P_{ads}) and convert to crystalline two-dimensional (2-D) Hofmann-type MOFs, $M(H_2O)_2[Ni(CN)_4]\cdot 4H_2O$ (**MNi-H$_2$O**; M = Mn, Fe, Co). The P_{ads} of **MnNi**, **FeNi**, and **CoNi** for water adsorption is P/P_0 = 0.4, 0.6, and 0.9, respectively. Amorphous functions of these materials prevented structural elucidation using X-ray crystallography techniques; however, the local-scale structures around the N-coordinated M^{2+} centers were evaluated by $L_{2,3}$-, K-edge X-ray absorption fine structure (XAFS) and magnetic measurements. In the hydration process, the coordination environment of central metals varied from tetrahedral to octahedral geometry, resulting in important reorganization of the MOF local structure. In contrast, $Ni[Ni(CN)_4]$ (**NiNi**) with square-planar Ni^{2+} centers did not show significant structural change, and therefore abruptly adsorbed water molecules in the low- humidity region. We demonstrated that the changes in the bond lengths and coordination geometry are related to the adsorption profiles of the cyanide-bridged MOFs.

Introduction

Metal-organic frameworks (MOFs) based on metal ions and bridging organic ligands[1-5] show various functional properties such as magnetism,[6-8] conductivity,[9-11] catalysis,[12-14] and luminescence[15-17] properties. The structural designability of MOFs arises from the diversity of their crystal structures in which rational strategies are proposed by changing the metal ion species and introducing substituents onto the ligands.[18-21] Cyanide-bridged MOFs involving cyanometallates are advantageous for rational construction of functional MOFs because various metal ions can be combined with cyanometallates, lead to versatile functional platforms such as Prussian blue-type and Hofmann-type compounds.[22-27]

MOFs area has expanded rapidly by the survey of crystalline materials. More recently, liquids and amorphous glasses have attracted much attention because of their potential for applications.[28-31] Famous MOF families such as UiO-66 [$Zr_6O_4(OH)_4(O_2C\text{-}C_6H_4\text{-}CO_2)_6$] and zeolitic imidazolate frameworks (ZIFs) have been changed into non-crystalline states by ball-millings, melt-quenching, and annealing, providing novel structure related physical property that dramatically enhance the magnetic properties, luminescence, proton conductivity, and porous nature.[32-39] However, precise characterization of non-crystalline materials is one of the most challenges for the design of functional materials with amorphous phase. By definition, the amorphous materials prevent from using the crystallographic techniques for structural elucidation. Effective approaches such as pair distribution function (PDF) analysis derived from X-ray total scattering have been developed to obtain structural insight into these materials. For example, this technique can be applied to the investigation of the switching for the proton conductor $[Zn(HPO_4)(H_2PO_4)_2](ImH_2)_2$ (ImH_2 = imidazolium).[40] However, one major drawback of PDF analysis is the complex signal processing; it displays the all interatomic distances within the material. Numerical simulations have also employed for considering the local deformations of MOFs such as MOF-5, MOF-74, and SNU-200. The decrease in the crystallinity upon exposure to humidity enhance the ability of methane adsorption.[41] From this perspective, the potential applications of low-crystalline MOFs have been expanded. However, the elcidation of the structural nature is still difficult, which prevents investigation of the detailed mechanisms of the structural changes induced by external or chemical stimuli. Also, the structural-related physical properties of cyanide-bridged amorphous MOFs remain largely unexplored thus far.

Herein, we rationally prepared various cyanide-bridged MOFs with amorphous state of type $M[Ni(CN)_4]$ (**MNi**; M = Mn, Fe and Co) and demonstrated the relationships between the local structures of the metal centers and water adsorption behaviors. $L_{2,3}$-, and K-edge X-ray absorption fine structure (XAFS) spectroscopy is powerful method to directly establish bond lengths and the geometries of the central metals in the amorphous phase. The slight differences in the bond lengths lead to the tunable water adsorption profiles, which is expounded by exploring the structural transformation from amorphous to the crystalline hydrated states.

Experimental Section

Materials

All chemicals were used without further purification. $M(H_2O)_2[Ni(CN)_4]\cdot 4H_2O$ (**MNi-H_2O**; M = Mn, Fe, Co, Ni) were synthesized according to a previously reported method.[24-27]

*$Mn(H_2O)_2[Ni(CN)_4]\cdot 4H_2O$ (**MnNi-H_2O**)*

A solution of $K_2[Ni(CN)_4]\cdot H_2O$ (198.7 mg, 0.767 mmol) in H_2O (100 mL) was added to a solution of $MnCl_2\cdot 4H_2O$ (151.8 mg, 0.767 mmol) in H_2O (80 mL) at room temperature. White powder samples were obtained after stirring for 24 h. Yield: 64.5%.

*$Fe(H_2O)_2[Ni(CN)_4]\cdot 4H_2O$ (**FeNi-H_2O**)*

***FeNi-H_2O** was prepared as a white powder sample in a similar method to that used for **MnNi-H_2O**, except for the use of $Fe(NH_4)_2(SO_4)_2\cdot 6H_2O$ (300.4 mg, 0.766 mmol) in degassed H_2O (80 mL). Yield: 70.1%.*

*$Co(H_2O)_2[Ni(CN)_4]\cdot 4H_2O$ (**CoNi-H_2O**)*

***CoNi-H_2O** was prepared as a white powder sample in a similar method to that used for **MnNi-H_2O**, except for the use of $CoCl_2\cdot 6H_2O$ (180.4 mg, 0.758 mmol). Yield: 74.5%.*

*$Ni(H_2O)_2[Ni(CN)_4]\cdot 4H_2O$ (**NiNi-H_2O**)*

***NiNi-H_2O** was prepared as a white powder sample in a similar method to that used for **MnNi-H_2O**, except for the use of $NiCl_2\cdot 6H_2O$ (180.4 mg, 0.759 mmol). Yield: 72.6%.*

*$M[Ni(CN)_4]$ (**MNi**)*

*The dehydrated powder samples of **MNi** were prepared by heating **MNi-H_2O** under vacuo at 400 K for 3 h.*

Physical Measurements

IR spectra were collected on a JASCO FT/IR-4200 spectrophotometer. PXRD patterns of **MNi-H_2O** were recorded with a Rigaku Ultima IV spectrometer using a reflection-free sample holder. In situ PXRD measurements under vacuo for **MNi** were conducted with a glass capillary connected to a homemade adsorption device. Thermal gravimetric analysis (TGA) was conducted using a Perkin Elmer STA6000 instrument in the temperature range of 300–930 K under N_2 atmosphere (heating rate: 5°C min^{-1}). The magnetic properties of **MNi-H_2O** and **MNi** were investigated using a Quantum Design MPMS-XL5R SQUID in the temperature range of 4–400 K under an applied DC magnetic field of 1000 Oe. Water adsorption and desorption isotherms were obtained using a BELSORP-MAX volumetric adsorption equipment (Microtrac BEL Corp.) at 298 K. The samples were dehydrated by heating at 400 K for 3 h before the measurements.

$L_{2,3}$-edge X-ray absorption fine structure (XAFS) measurements of **MNi** (M = Mn, Fe, and Co) were performed at BL-11 of Synchrotron Radiation Center in Ritsumeikan University (SR center). The $L_{2,3}$-edge XAFS spectra of M were obtained at room temperature in the partial electron yield (PEY) mode with a photon energy resolution of ~500 meV. The varied-line-spacing plane gratings used for the measurement were supplied with monochromatic light with a photon energy of $h\nu$ = 40−1000 eV. A microchannel plate (MCP) for detecting the Auger and secondary electrons was set at an angle of 45° below the direction of photon propagation. A voltage of −550 V was used to the gold mesh installed in front of the MCP for the $L_{2,3}$-edge measurements due to the strong background caused by the C, N, and O K-edge absorptions in the spectra, Sample preparation was carried out in an Ar-filled glovebox to prevent H_2O adsorption of atmospheric water. The sample was transported to a vacuum chamber by using a transfer vessel. The photon energy for each sample was calibrated relative to top of the L_3-edge peak of Mn_2O_3 (641.5 eV), α-Fe_2O_3 (709.7 eV), and $LiCoO_2$ (780.3 eV), respectively.

K-edge absorption near-edge structure (XANES) and extended X-ray absorption fine structure (EXAFS) measurements of **MNi-H_2O** and **MNi** (M = Mn, Fe, and Co) were carried out at BL-11 of the SAGA Light Source (SAGA-LS). A Si(111) double crystal monochromator was installed in the range of $h\nu$ = 2.1–23 keV with a photon energy resolution (dE/E) of 10^{-4} – 10^{-3}. The XANES and EXAFS spectra were recorded with the transmission mode at room temperature by two ionization chambers. The absorbance ($-\log(I_1/I_0)$) was estimated from the incident X-ray intensity (I_0) and the transmitted X-ray intensity (I_1). Mixture of He 50%/N_2 50% and Ar 15%/N_2 85% was employed as ionization gases for I_0 and I_1, respectively. The calibration of photon energy was performed by using a 3*d* transition metal foil at room temperature. The samples were diluted with high-purity boron nitride for the appropriate concentration for XAFS measurement. The samples were sealed in a polyethylene bag. Fourier-transform spectra were obtained using the k^2-weighted EXAFS spectra in which the *K*-edge XAFS profiles were processed using Athena and Artemis software.[42]

Amorphous MNi formation by dehydration of MNi-H$_2$O

The crystalline powders of Hofmann-type M(H$_2$O)$_2$[Ni(CN)$_4$]·4H$_2$O (**MNi-H$_2$O**; M = Mn, Fe, Co) species were synthesized according to a previously reported method.[24-27] Figure 1(a) displays the crystal structure of **CoNi-H$_2$O**. **MNi-H$_2$O** formed flexible two-dimensional (2D) cyanide-bridged layer structures based on the square-planar [Ni(CN)$_4$]$^{2-}$ with octahedral M^{2+}, in which two water molecules coordinate to the axial sites of M^{2+}.The four water molecules are located between layers as crystal solvents. The powder X-ray diffraction (PXRD) patterns of **MNi-H$_2$O** showed that the all **MNi-H$_2$O** have isostructural with slight systematic shifts in the diffraction peak positions, indicating the effect of the different ionic radii of M^{2+} (Figure 1(b)).

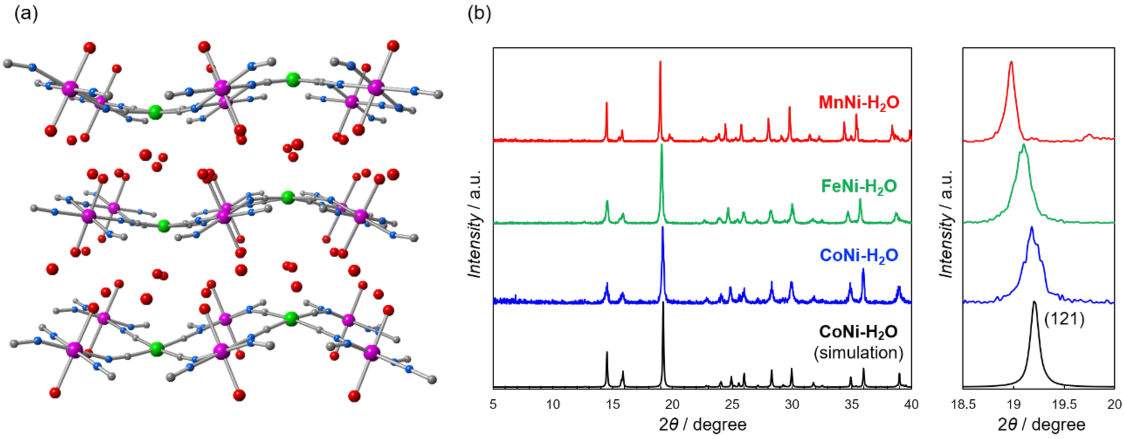

Fig. 1(a) Crystal structure of **CoNi-H$_2$O**. Atomic code: Co, purple; Ni, green; C, grey; N, blue; O, red. H atoms of H$_2$O molecules are omitted for clarity. (b) PXRD patterns of **MNi-H$_2$O** (M = Mn, Fe, Co).

The FT-IR spectra of **MNi-H$_2$O** exhibit the stretching mode of bridging CN$^-$ ligands around 2180 cm^{-1} and broad bands of water around 1600 and 3000–3600 cm^{-1} (Figure 2). Thermogravimetric analysis (TGA) suggested that the incorporated six water molecules in **MNi-H$_2$O** were removed below 170°C (Figure 3). The dehydrated forms, **MNi**, was prepared by heating **MNi-H$_2$O** at 400 K under vacuo. Although **MNi** showed low crystalinity (Figure 4), IR spectra of **MNi** indicated that the cyanide-bridged structure maintained after rehydration treatment and the stretching bands of CN$^-$ were confirmed at 2162 cm^{-1} for **MnNi**, 2164 cm^{-1} for **FeNi**, and 2178 cm^{-1} for **CoNi** (Figure 5), respectively.

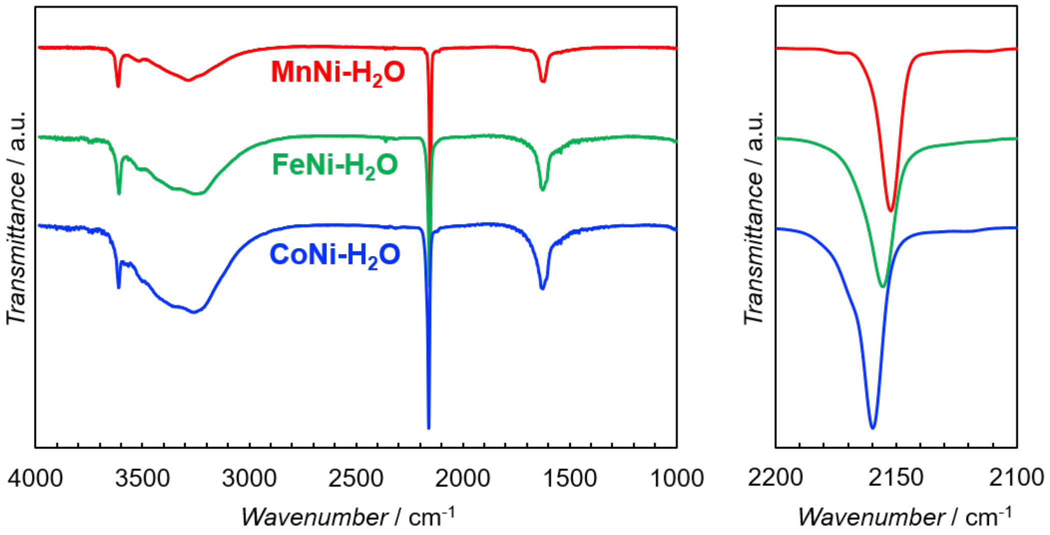

Fig. 2 IR spectra of **MNi-H$_2$O**

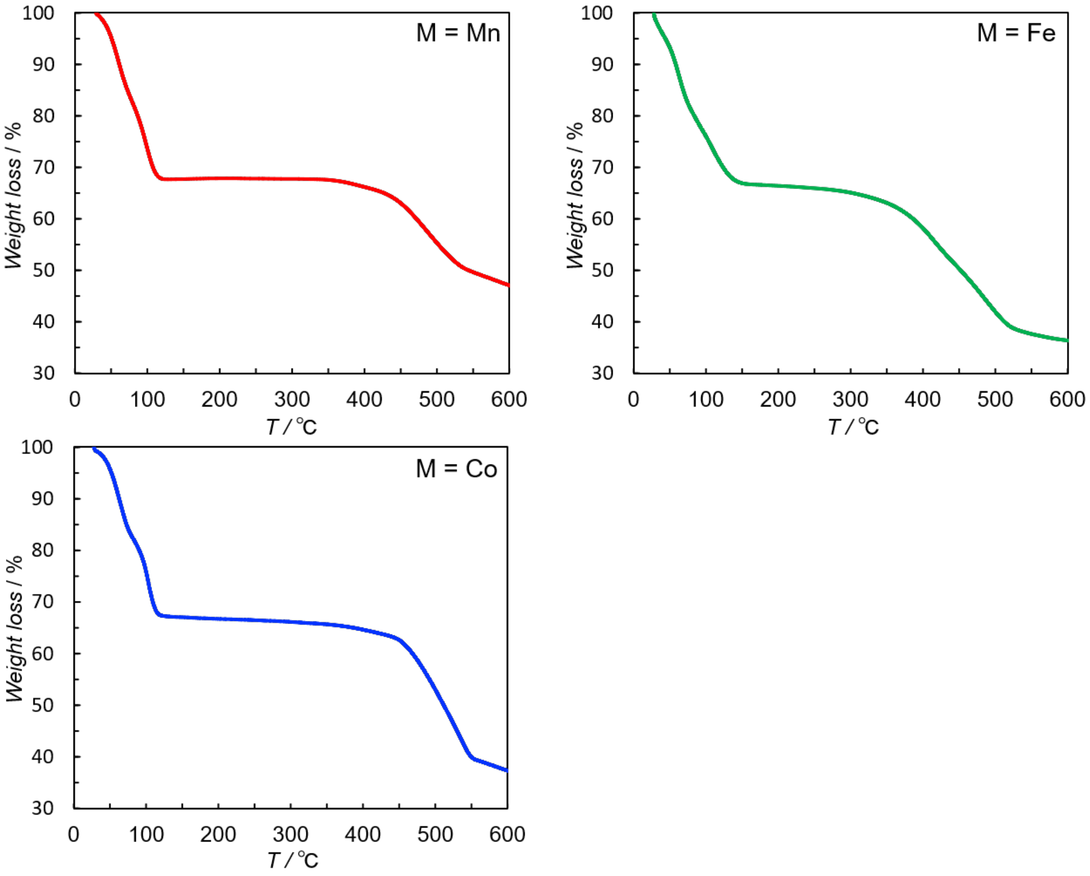

Fig. 3 TGA curves of **MNi-H$_2$O** (M = Mn, Fe, Co).

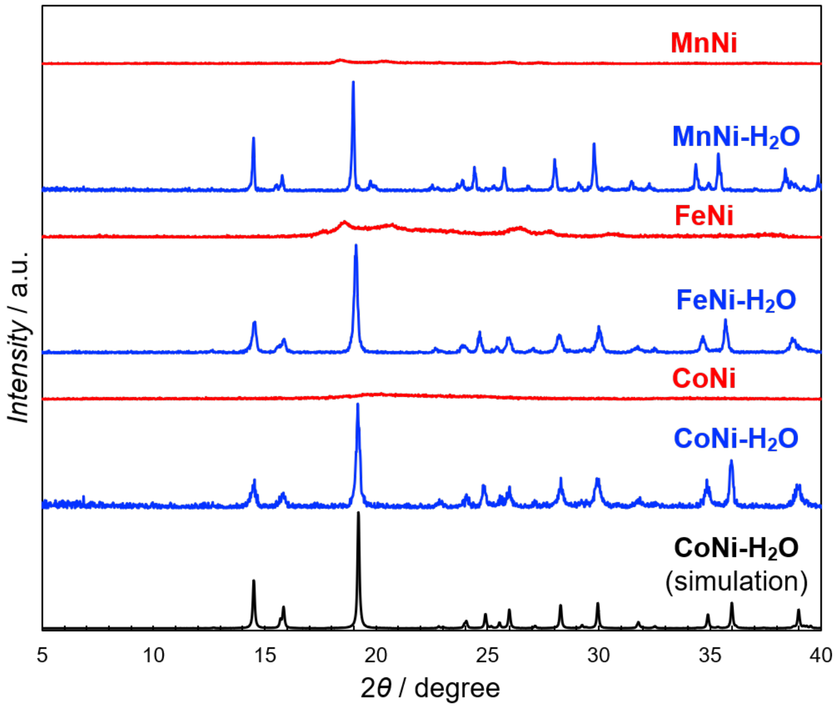

Fig. 4 PXRD patterns of **MNi-H_2O** (blue) and **MNi** (red), and a simulated pattern of **CoNi-H_2O** (black). [25]

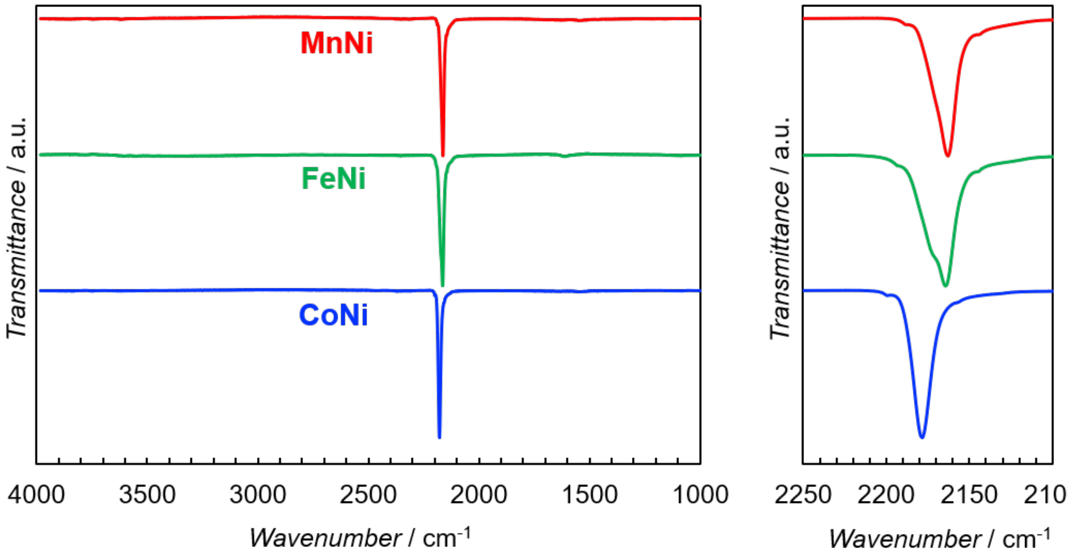

Fig. 5 IR spectra of **MNi** (M = Mn, Fe, Co).

$L_{2,3}$- and *K*-edge XAFS spectroscopy

$L_{2,3}$-edge XAFS measurements were performed to reveal the local coordination structures of the central metals (non-nickel metals) due to the difficulty of crystallographic structural analysis for amorphous **MNi**. The information about the local coordination geometry around the M^{2+} sites can be obtained through $L_{2,3}$-edge XAFS by allowing survey of the element-selective 3*d* local electronic structures arising from the Coulombic interaction between the 2*p* core-holes and the 3*d* valence electrons via $2p \rightarrow 3d$ ($L_{2,3}$-edge) absorption process.[43,44] The Co $L_{2,3}$-edge XAFS spectra of **CoNi** in the partial electron yield (PEY) mode is shown in Figure 6.

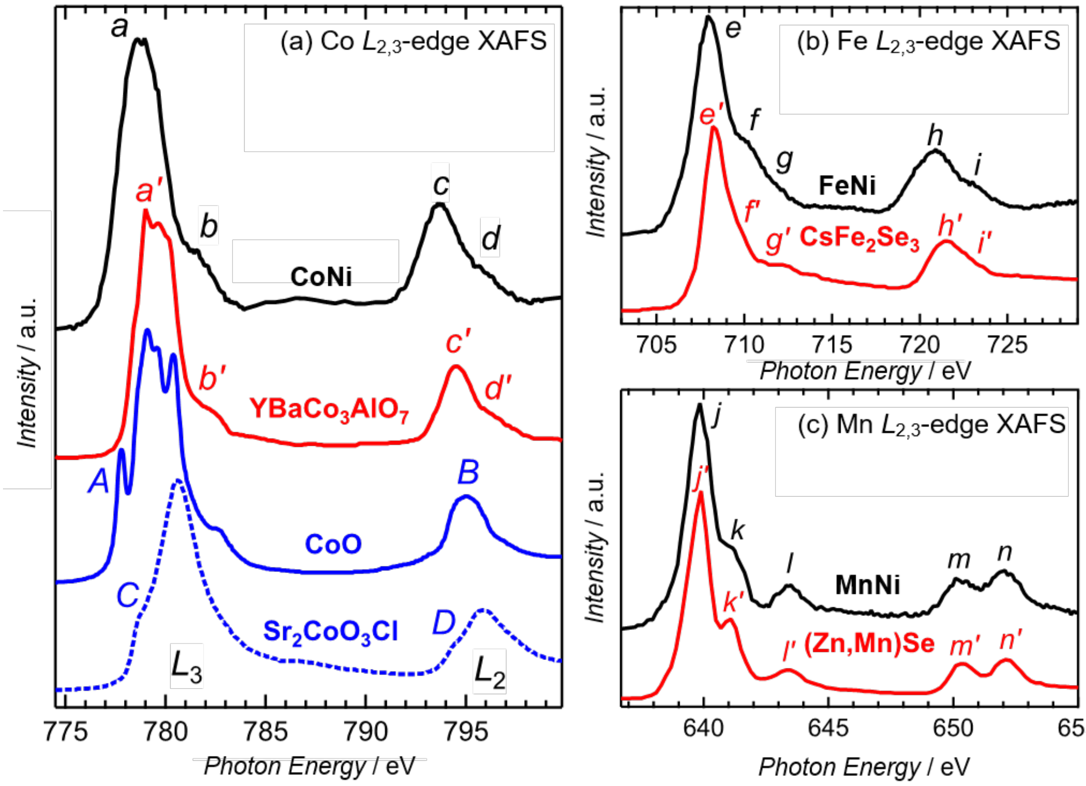

Fig. 6 $L_{2,3}$-edge XAFS spectra of (a) **CoNi** (black), $YBaCo_3AlO_7$ (red),[45] CoO (blue solid line),[46] and Sr_2CoO_3Cl (blue dashed line).[47] (b) **FeNi** (black) and $CsFe_2Se_3$ (red).[48] (c) **MnNi** (black) and (Zn,Mn)Se (red).[49]

The double-peak structures corresponding to the Co 2*p* core-hole spin-orbit coupling were observed as L_3 (*a* and *b*; $h\nu \approx 779$ eV) and L_2 (*c* and *d*; $h\nu \approx 794$ eV) edges, indicating that the Co^{2+} centers in **CoNi** formed a tetrahedral geometry. Moreover, comparison with a reference sample, $YBaCo_3AlO_7$, with a tetrahedral Co^{2+} geometry exhibited the similar L_3 and L_2 edges.[45] The reference samples of CoO (octahedral Co^{2+}; *A* and *B*)[46] and Sr_2CoO_3Cl (octahedral Co^{3+}; *C* and *D*)[47] showed different electronic structures. The change in the coordination geometry from octahedral in **CoNi-H_2O** to tetrahedral in **CoNi** was also supported by their magnetic properties. The $\chi_M T$ value of **CoNi** was smaller than **CoNi-H_2O** due to the smaller orbital contribution of tetrahedral Co^{2+} (Figure 7). Furthermore, the Mn and Fe $L_{2,3}$-edge XAFS spectra suggested that the Mn and Fe centers in **MnNi** and **FeNi** also formed tetrahedral geometry (Figure 6(b) and 6(c)). The main peaks assigned to L_3 (Fe = 708, 710, 712 eV; *e-g*, Mn = 640, 641, 643 eV; *j–l*) and L_2 (Fe = 721, 723 eV; *h* and *i*, Mn = 650, 652 eV; *m* and *n*), which were good agreement with the tetrahedral geometries of Fe^{2+} and Mn^{2+} (Figure 6(b) and 6(c) also involve the spectra for $CsFe_2Se_3$ (tetrahedral Fe^{2+}; *e'–i'*)[48] and (Zn,Mn)Se (tetrahedral Mn^{2+}; *j'–n'*)[49]).

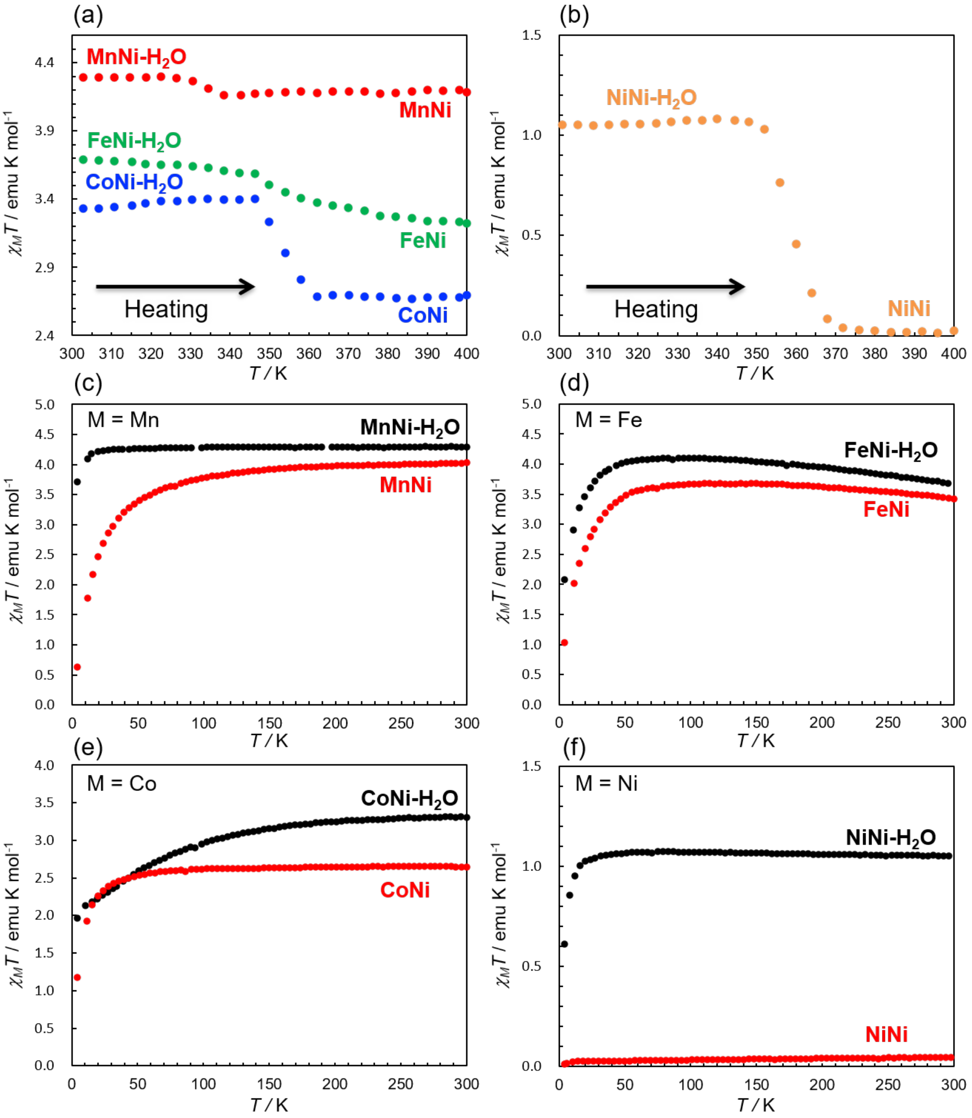

Fig. 7 $\chi_M T$ *vs* T plots in the heating process (300–400K) for (a) **MNi-H_2O** (M = Mn, Fe, Co) and (b) **NiNi-H_2O**. $\chi_M T$ *vs* T plots of **MNi-H_2O** and **MNi** for M = (c) Mn, (d) Fe, (e) Co, (f) Ni.

K-edge XANES and EXAFS measurements were conducted for further investigation of the local structures in **MNi**. The *K*-edge XAFS spectra provides the efficient information of local structures around metal ions via the 1*s*→4*p* excitation process.[50-53] The pre-edge peaks were observed in the XANES spectra of **MNi** (M = Mn, Fe, and Co) at 6538 eV (Mn), 7110 eV (Fe), and 7707 eV (Co), demonstrating the tetrahedral geometry lacking the inversion symmetry (Figure 8).

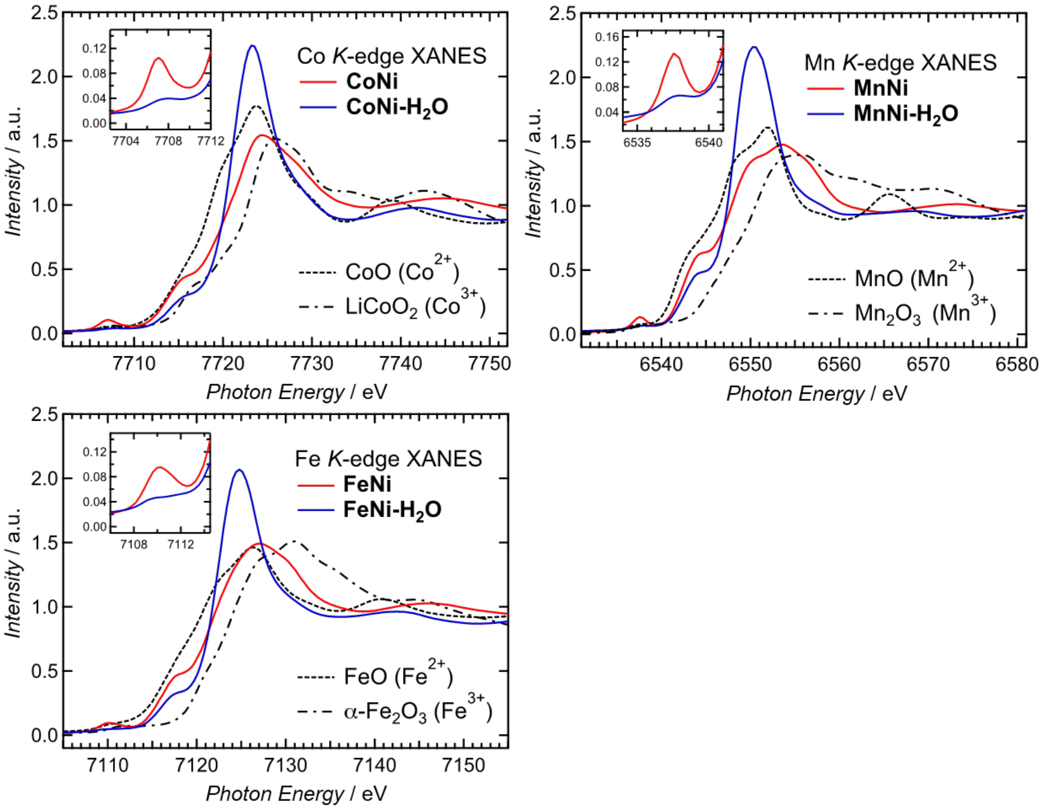

Fig. 8 *K*-edge XANES spectra of MNi-H$_2$O, MNi (M = Mn, Fe, Co) and reference samples of CoO (Co^{2+}), LiCoO$_2$ (Co^{3+}), MnO (Mn^{2+}), Mn$_2$O$_3$ (Mn^{3+}), FeO (Fe^{2+}), and α-Fe$_2$O$_3$ (Fe^{3+})

The systematic trend of the bond lengths around central metals was revealed by the EXAFS data shown in Figure 9(a). The Fourier-transformed spectra exhibited the characteristic triple-peaks originated from the distances between the central metal (M) and the neighboring N ($d_{\text{M-N}}$), C ($d_{\text{M-C}}$), and Ni ($d_{\text{M-Ni}}$) atoms of the $[Ni(CN)_4]^{2-}$ units, respectively (Figure 9(b)). These assignments are supported by the close *K*-edge EXAFS spectra with triple-peaks in the interdigitated Hofmann-type 2D-MOF of type $Fe(pyridine)_2[Ni(CN)_4]$.[54] Importantly, the values of $d_{\text{M-N}}$ decreased in the order: $d_{\text{Co-N}} < d_{\text{Fe-N}} < d_{\text{Mn-N}}$, corroborating the peak shift of the bridging CN^- bands confirmed in the IR data (Figure 5).

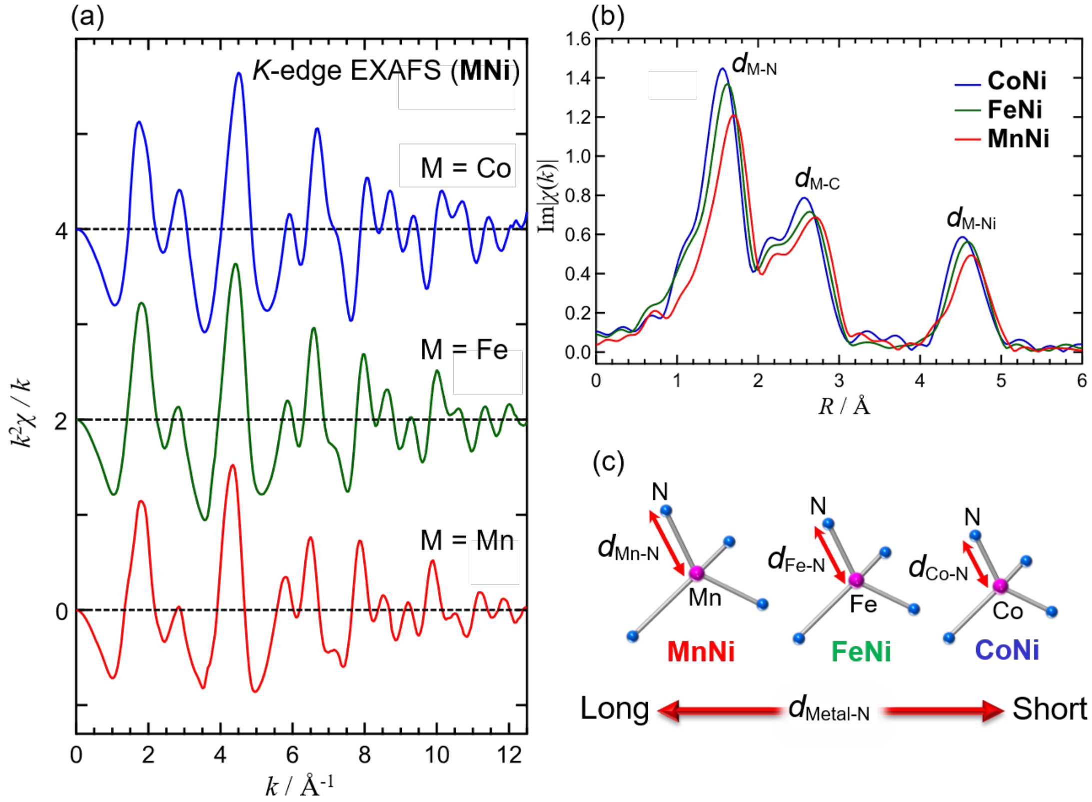

Fig. 9 (a) *K*-edge XAFS spectra of **MNi** (M = Mn, Fe, and Co), (b) Fourier-transformed spectra. (c) Schematic illustration of the distance between the central metals (M) and the neighboring N atom of CN^- ligand ($d_{\text{M-N}}$).

Metal-dependent Water Adsorption Behavior

Finally, we demonstrated the impact of differences in the coordination environment involving the bond lengths for **MNi** series on the water adsorption behaviors.

The water adsorption behaviors were compared to those of the control material $Ni[Ni(CN)_4]$ (**NiNi**), having a hydrated form of type $Ni(H_2O)_2[Ni(CN)_4]\cdot4H_2O$ (**NiNi-H$_2$O**) identical that of the other **MNi-H$_2$O** materials. Notably, the local geometry of the N-coordinated Ni^{2+} centers of **NiNi** retained a square-planar geometry after dehydration treatment.[55] We could investigate the structural impacts arising from different local structures of M^{2+} on the water adsorption behaviors by using **NiNi**. Figure 10 showed that the all **MNi** adsorbed approximately six water molecules at 298 K along with re-forming the crystalline **MNi-H$_2$O** (Figure 11); however, the adsorption profiles strongly depended on the central metals. The one-step abrupt water adsorption at a certain vapor pressure (P_{ads}) was observed in M = Mn, Fe and Co compounds. However, **NiNi** displayed two-step adsorption from the low-vapor pressure region. Hence, the one-step water adsorption property was attributed to the tetrahedral metal centers in amorphous **MNi** (M = Mn, Fe and Co).

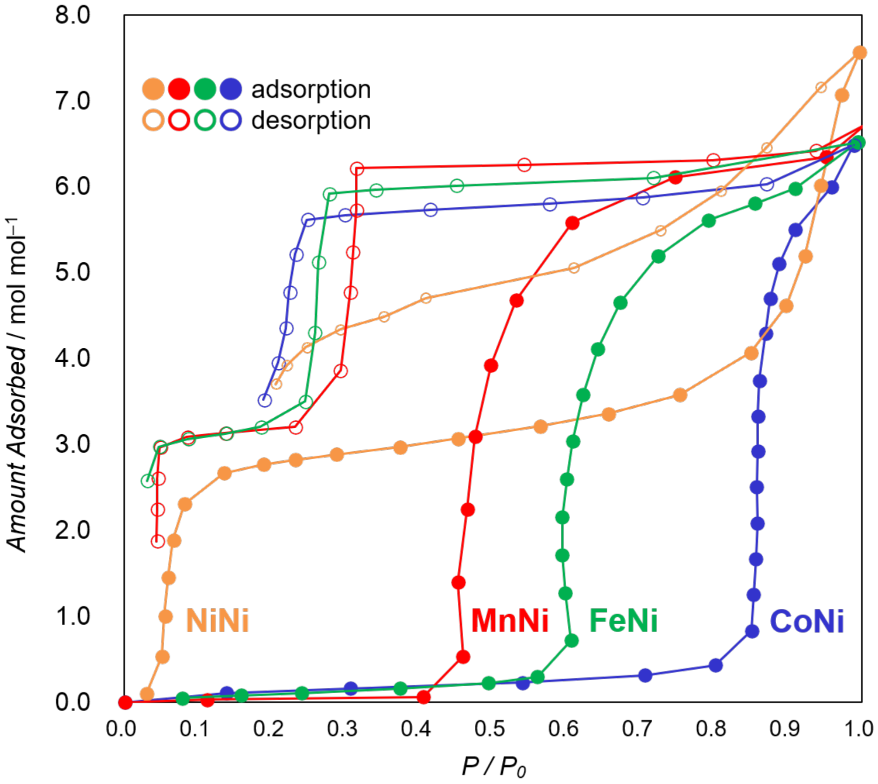

Fig. 10 H_2O adsorption/desorption isotherms of **NiNi** (orange), **MnNi** (red), **FeNi** (green), and **CoNi** (blue) at 298 K. The filled and open circles display the adsorption and desorption processes, respectively.

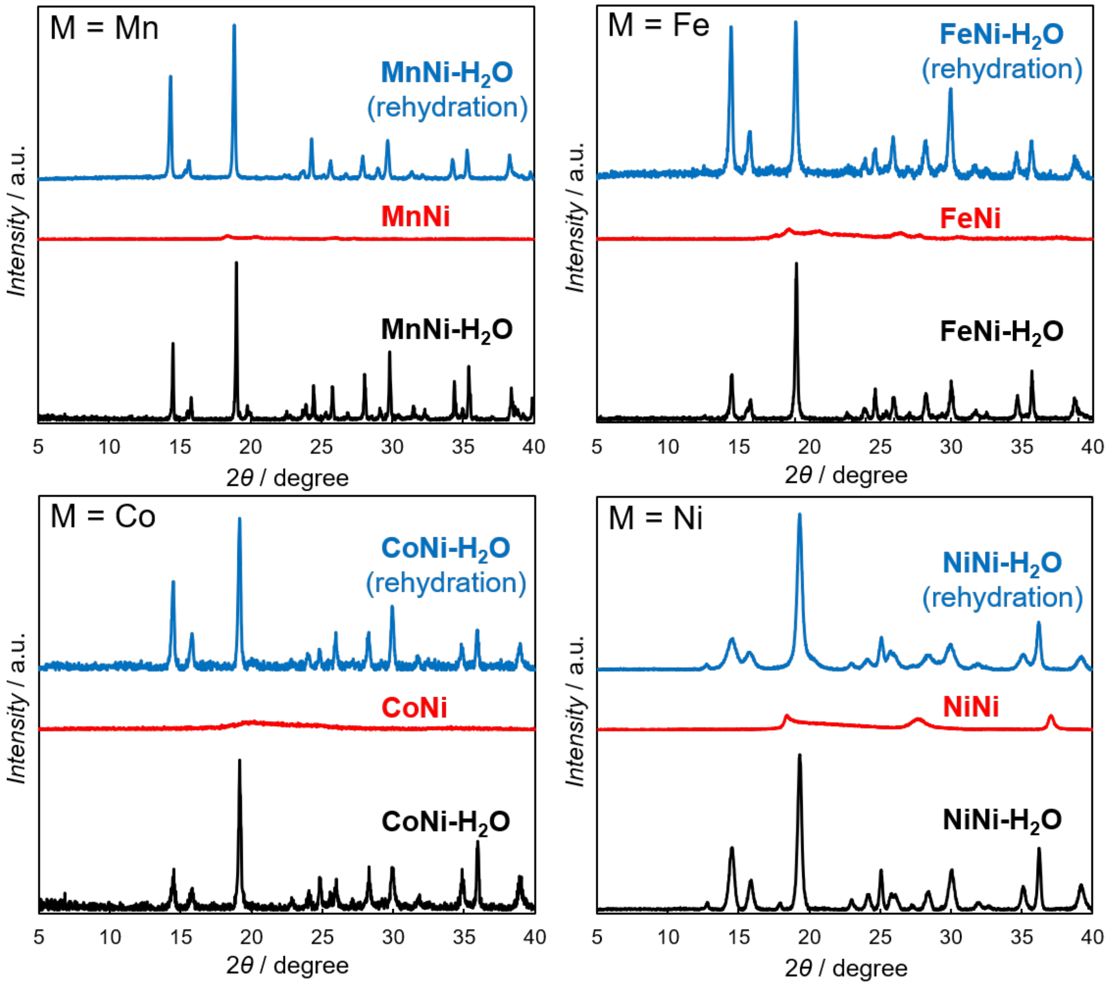

Fig. 11 PXRD patterns of **MNi-H_2O** (black), **MNi** (red), and **MNi-H_2O** (rehydration; blue).

Importantly, crystalline materials with square-planar and tetrahedral centers adopting a similar 3D-sphalerite type structure have been reported (named as Fe[Pd(CN)$_4$] (**FePd**))[56] and Zn[M(CN)$_4$] (M = Ni, Pd, Pt).[57] Also, **FePd** showed one-step water adsorption behavior originating from a reversible single-crystal to single-crystal transformation from the 3D structure with tetrahedral Fe^{2+} to 2D Hofmann-layers with octahedral Fe^{2+} in Fe(H$_2$O)$_2$[Pd(CN)$_4$]·4H$_2$O (**FePd-H$_2$O**) involving cleavage and reforming of the cyanide bridges (Figure 12).[56]

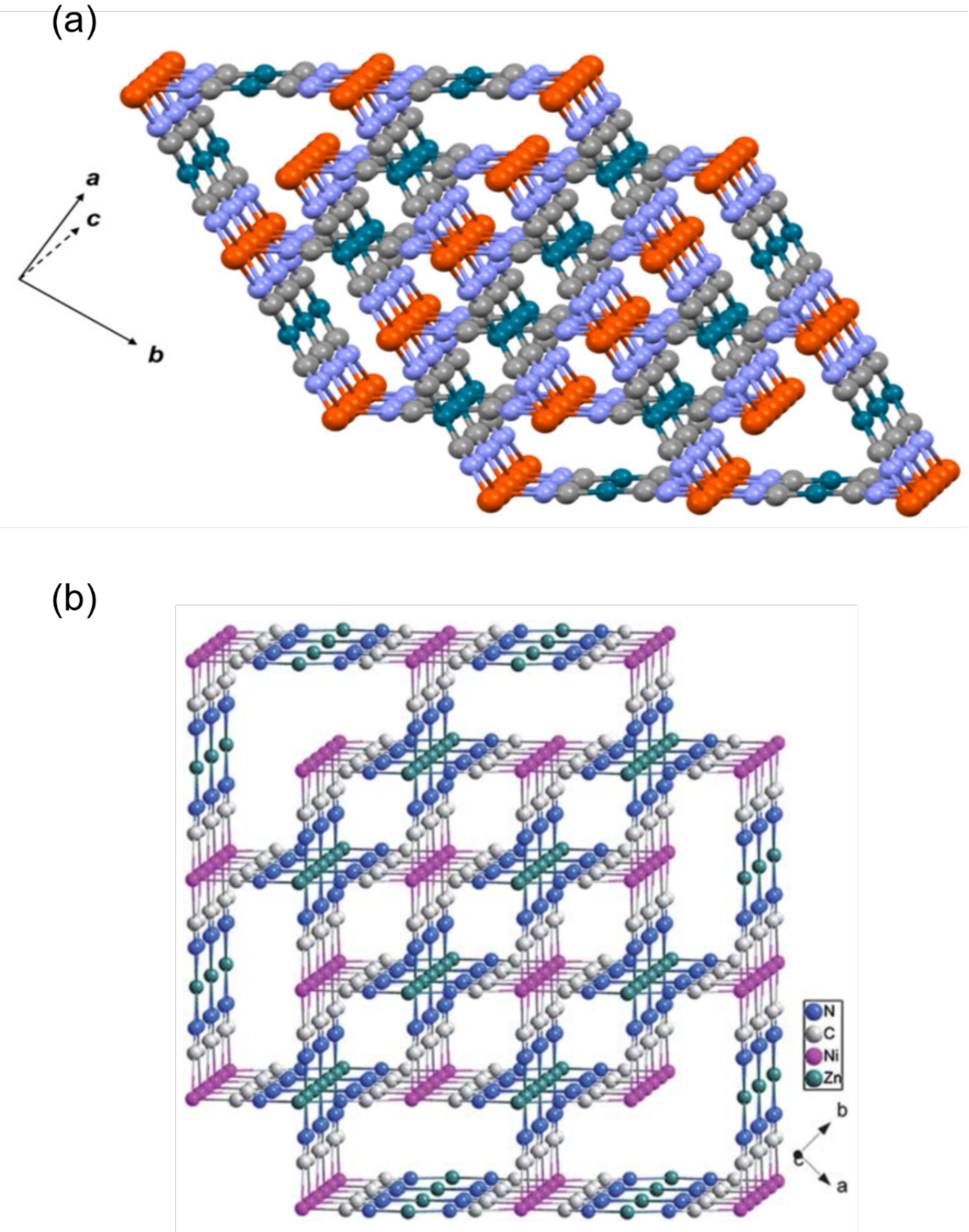

Fig. 12 Crystal structure of (a) Fe[Pd(CN)$_4$] and (b) Zn[Ni(CN)$_4$]

Thus, the water-driven amorphous–crystalline transformation of **MNi** plausibly involve the similar change in the local structure around the M^{2+} centers except for M = Ni. The coordinative water adsorption with amorphous–crystalline changes and the ensuing lattice water adsorption would be observed as one-step adsorption because **MNi** with tetrahedral structure do not possess interstitial adsorption sites. Moreover, the P_{ads} of **MNi** was related to the local structure of the M^{2+} centers, where the values of P_{ads} increased as the $d_{\mathrm{M\text{-}N}}$ became shorter. That is, smaller $d_{\mathrm{M\text{-}N}}$ values give rise to higher activation energies in the amorphous–2D structural changes because of hard breaking of the cyanide bridge.[58-60] Additionally, **MNi** showed no structural transformations for other guests such as MeCN, THF, and MeOH vapor (Figure 13).

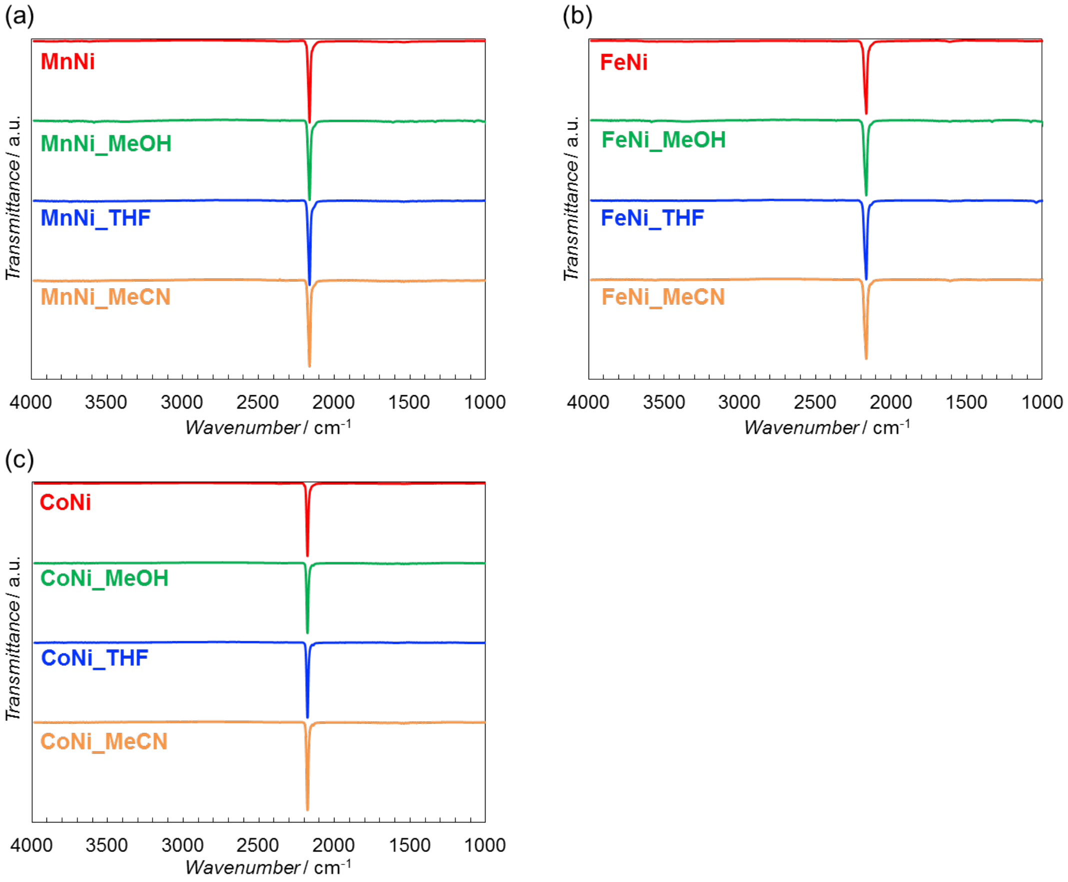

Fig. 13 IR spectra of MNi under saturated MeOH, THF, and MeCN vapors for M = (a) Mn, (b) Fe, (c) Co.

The suggested mechanism of the water adsorption behaviors in **MNi** is also supported by the result of **NiNi**, showing the two-step water adsorption. In the first step, intermediate state of $Ni(H_2O)_2[Ni(CN)_4]\cdot H_2O$ was formed with the coordination of water molecules to square-planar Ni^{2+} sites.[55] Then second adsorption step was observed around $P/P_0 = 0.9$. Thus, the resultant two-step adsorption behavior in **NiNi** was driven by the formation of the intermediate stable structure, which required smaller activation energy than those of the other **MNi** systems with corresponding tetrahedral geometry (Figure 14).

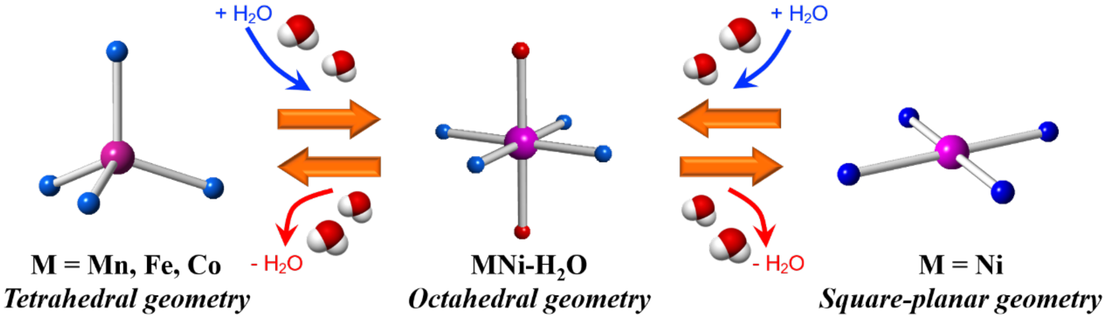

Fig. 14 Schematic illustration of the differences in the adsorption process for **MNi** analogues (M = Mn, Fe, Co, and Ni).

Conclusion

We described the rational design of cyanide-based amorphous metal-organic frameworks (MOFs) M[Ni(CN)$_4$] (**MNi**; M = Mn, Fe, Co) through regulating the water adsorption properties by changing the central metals. All three compounds of **MNi** showed an abrupt water adsorption up to six water molecules at a certain vapor pressure (P_{ads}) and undergo conversion to crystalline Hofmann-type MOFs, M(H$_2$O)$_2$[Ni(CN)$_4$]·4H$_2$O (**MNi-H$_2$O**; M = Mn, Fe, Co). Although the amorphous properties of these materials prevented structural elucidation using X-ray crystallography techniques, $L_{2,3}$- and K-edge XAFS analyses revealed that the P_{ads} for water adsorption is related by the tetrahedral M^{2+} centers and bond length in amorphous **MNi**. In contrast, Ni[Ni(CN)$_4$] (**NiNi**) with square-planar Ni^{2+} centers did not undergo significant structural transformation, and therefore abruptly adsorbed water in the low-pressure region. The number of investigations of amorphous MOFs has increased rapidly because of their potential for applications; however, the strict interpretation of structure–property relationship of amorphous MOFs is still difficult at this stage. From this perspective, this work finally highlights the control of guest adsorption properties arising from the local structure in amorphous phases can provide new insights into the rational design of functional amorphous materials.

References

1 S. Kitagawa, R. Kitaura, S. Noro, *Angew. Chem. Int. Ed.* **2004**, *43*, 2334–2375.

2. O. M. Yaghi, M. O'Keeffe, N. W. Ockwig, H. K, Chae, M Eddaoudi, Kim, J, *Nature* **2003**, *423*, 705–714.

3. J. L. C. Rowsell, O. M. Yaghi, *Angew. Chem. Int. Ed.* **2005**, *44*, 4670–4679.

4. G. Férey, *Chem. Soc. Rev.* **2007**, *37*, 191–214.

5. Z. Chen, P. Li, X. Zhang, P. Li, M. C. Wasson, T. Islamoglu, J. F. Stoddart, O. K. Farha, *J. Am. Chem. Soc.* **2019**, *141*, 2900–2905.

6. M. Ohba, K. Yoneda, G. Agustí, M. C. Muñoz, A. B. Gaspar, J. A. Real, M. Yamasaki, H. Ando, Y. Nakao, S. Sakaki, S. Kitagawa, *Angew. Chem. Int. Ed.* **2009**, *48*, 4767–4771.

7. W. Kosaka, Z. Liu, J. Zhang, Y. Sato, A. Hori, R. Matsuda, S. Kitagawa, H. Miyasaka, *Nat. Commun.* **2018**, *9*, 5420.

8. M. Kurmoo, *Chem. Soc. Rev.* **2009**, *38*, 1353–1379.

9. D. Sheberla, L. Sun, M. A. Blood-Forsythe, S. Er, C. R. Wade, C. K. Brozek, A. Aspuru-Guzik, M. Dincă, *J. Am. Chem. Soc.* **2014**, *136*, 8859–8862.

10. M. Sadakiyo, T. Yamada, H. Kitagawa, *J. Am. Chem. Soc.* **2009**, *131*, 9906–9907.

11. J. G. Park, M. L. Aubrey, J. Oktawiec, K. Chakarawet, L. E. Darago, F. Grandjean, G. J. Long, J. R. Long, *J. Am. Chem. Soc.* **2018**, *140*, 8526–8534.

12. J. Lee, O. K. Farha, J. Roberts, K. A. Scheidt, S. T. Nguyen, J. T. Hupp, *Chem. Soc. Rev.* **2009**, *38*, 1450–1459.

13. J. S. Seo, D. Whang, H. Lee, S. I. Jun, J. Oh, Y. J. Jeon, K. Kim, *Nature* **2000**, *404*, 982–986.

14. K. D. Vogiatzis, E. Haldoupis, D. J. Xiao, J. R. Long, J. I. Siepmann, L. Gagliardi, *J. Phys. Chem. C* **2016**, *120*, 18707–18712.

15. N. Yanai, K. Kitayama, Y. Hijikata, H. Sato, R. Matsuda, Y. Kubota, M. Takata, M. Mizuno, T. Uemura, S. Kitagawa, *Nat. Mater.* **2011**, *10*, 787–793.

16. M. Wang, L. Guo, D. Cao, *Anal. Chem.* **2018**, *90*, 3608–3614.

17. B. R. Varju, S. A. Wollschlaeger, D. B. Leznoff, *Chem. – Eur. J.* **2019**, *25*, 9017–9025.

18. M. Sadakiyo, T. Yamada, K. Kato, M. Takata, H. Kitagawa, *Chem. Sci.* **2016**, *7*, 1349–1356.

19. H. Furukawa, J. Kim, N. W. Ockwig, M. O'Keeffe, O. M. Yaghi, *J. Am. Chem. Soc.* **2008**, *130*, 11650–11661.

20. L. Hamon, C. Serre, T. Devic, T. Loiseau, F. Millange, G. Férey, G. D. Weireld, *J. Am. Chem. Soc.* **2009**, *131*, 8775–8777.

21. Y. Kamakura, A. Hikawa, H. Yoshikawa, W. Kosaka, H. Miyasaka, D. Tanaka, *Chem. Commun.* **2020**, *56*, 9106–9109.
22. S. Ohkoshi, K. Arai, Y. Sato, K. Hashimoto, *Nat. Mater.* **2004**, *3*, 857–861.
23. S. S. Kaye, J. R. Long, *J. Am. Chem. Soc.* **2005**, *127*, 6506–6507.
24. J. Rodríguez-Hernández, A. A. Lemus-Santana, C. N. Vargas, E. Reguera, *Comptes Rendus Chim.* **2012**, *15*, 350–355.
25. T. Niu, G. Crisci, J. Lu, A. J. Jacobson, *Acta Crystallogr. Sect. C* **1998**, *54*, 565–567.
26. O. Reyes-Martinez, E. Torres-García, G. Rodríguez-Gattorno, E. Reguera, *Materials* **2013**, *6*, 1452–1466.
27. A. Alowasheeir, S. Tominaka, Y. Ide, Y. Yamauchi, Y. Matsushita, *CrystEngComm* **2018**, *20*, 6713–6720.
28. C. Orellana-Tavra, M. Köppen, A. Li, N. Stock, D. Fairen-Jimenez, *ACS Appl. Mater. Interfaces* **2020**, *12*, 5633–5641.
29. T. D. Bennett, J.-C. Tan, Y. Yue, E. Baxter, C. Ducati, N. J. Terrill, H. H.-M. Yeung, Z. Zhou, W. Chen, S. Henke, A. K. Cheetham, G. N. Greaves, *Nat. Commun.* **2015**, *6*, 8079.
30. Q. S. Mei, K. Lu, *Prog. Mater. Sci.* **2007**, *52*, 1175–1262.
31. R. Gaillac, P. Pullumbi, K. A. Beyer, K. W. Chapman, D. A. Keen, T. D. Bennett, F.-X. Coudert, *Nat. Mater.* **2017**, *16*, 1149–1154.
32. T. D. Bennett, Y. Yue, P. Li, A. Qiao, H. Tao, N. G. Greaves, T. Richards, G. I. Lampronti, S. A. T. Redfern, F. Blanc, O. K. Farha, J. T. Hupp, A. K. Cheetham, D. A. Keen, *J. Am. Chem. Soc.* **2016**, *138*, 3484–3492.
33. T. D. Bennett, P. J. Saines, D. A. Keen, J.-C. Tan, A. K. Cheetham *Chem. – Eur. J.* **2013**, *19*, 7049–7055.
34. D. Muñoz-Gil, F. M. L. Figueiredo, *Nanomaterials* **2019**, *9*, 1369.
35. S. Liu, Z. Xiang, Z. Hu, X. Zheng, D. Cao, *J. Mater. Chem.* **2011**, *21*, 6649–6653.
36. S. Horike, K. Kadota, T. Itakura, M. Inukai, S. Kitagawa, *Dalton Trans.* **2015**, *44*, 15107–15110.
37. F. Yang, W. Li, B. Tang. *J. Alloys Compd.* **2018**, *733*, 8–14.
38. L. Valenzano, B. Civalleri, S. Chavan, S. Bordiga, M. H. Nilsen, S. Jakobsen, K. P. Lillerud, C. Lamberti, *Chem. Mater.* **2011**, *23*, 1700–1718.
39. T. D. Bennett, T. K. Todorova, E. F. Baxter, D. G. Reid, C. Gervais, B. Bueken, B. V. de Voorde, D. D. Vos, D. A. Keen, C. Mellot-Draznieks, *Phys. Chem. Chem. Phys.* **2016**, *18*, 2192–2201.
40. S. S. Nagarkar, S. Horike, T. Itakura, B. L. Ouay, A. Demessence, M. Tsujimoto, S. Kitagawa, *Angew. Chem. Int. Ed.* **2017**, *56*, 4976–4981.

41. W. Jeong, D.-W. Lim, S. Kim, A. Harale, M. Yoon, M. P. Suh, J. Kim, *Proc. Natl. Acad. Sci.* **2017**, *114*, 7923–7928.
42. B. Ravel, M. Newville, *J. Synchrotron Radiat.* **2005**, *12*, 537–541.
43. H. Wang, G. Peng, L. M. Miller, E. M. Scheuring, S. J. George, M. R. Chance, S. P. Cramer, *J. Am. Chem. Soc.* **1997**, *119*, 4921–4928.
44. M. Al Samarai, A. W. Hahn, A, A. Beheshti, Y.-T. Cui, K. Yamazoe, J. Miyawaki, Y. Harada, O. Rüdiger, S. DeBeer, *ACS Appl. Mater. Interfaces* **2019**, *11*, 38595–38605.
45. N. Hollmann, Z. Hu, M. Valldor, A. Maignan, A. Tanaka, H. H. Hsieh, H.-J. Lin, C. T. Chen, L. H. Tjeng, *Phys. Rev. B*, **2009**, *80*, 085111.
46. C. F. Chang, Z. Hu, H. Wu, T. Burnus, N. Hollmann, M. Benomar, T. Lorenz, A. Tanaka, H.-J. Lin, H. H. Hsieh, C. T. Chen, L. H. Tjeng, *Phys. Rev. Lett.,* **2009**, *102*, 116401.
47. F. Degroot, M. Abbate, J. Vanelp, G. Sawatzky, Y. Ma, C. Chen, F. Sette, *J. Phys.-Condens. Matter* **1993**, *5*, 2277–2288.
48. K. Takubo, Y. Yokoyama, H. Wadati, S. Iwasaki, T. Mizokawa, T. Boyko, R. Sutarto, F. He, K. Hashizume, S. Imaizumi, T. Aoyama, Y. Imai, K. Ohgushi, *Phys. Rev. B* **2017**, *96*, 115157.
49. K. Cho, H. Koh, J. Park, S.-J. Oh, H.-D. Kim, M. Han, J.-H. Park, C. T. Chen, Y. D. Kim, J.-S. Kim, B. T. Jonker, *Phys. Rev. B*, **2001**, *63*. 15520.
50. R. A. D. Pattrick, J. F. W. Mosselmans, J. M. Charnock, K. E. R. England, G. R. Helz, C. D. Garner, D. J. Vaughan, *Geochim. Cosmochim. Acta* **1997**, *61*, 2023–2036.
51. T. Pauporté, Y. Soldo-Olivier, R. Faure, *J. Phys. Chem. B* **2003**, *107*, 8861–8867.
52. A. M. Shahin, F. Grandjean, G. J. Long, T. P. Schuman, *Chem. Mater.* **2005**, *17*, 315–321.
53. J.-W. Xiu, G.-E. Wang, M.-S. Yao, C.-C. Yang, C.-H. Lin, G. Xu, *Chem. Commun.* **2017**, *53*, 2479–2482.
54. J. Okabayashi, S. Ueno, Y. Wakisaka, T. Kitazawa, *Inorganica Chim. Acta* **2015**, *426*, 142–145.
55. S. J. Hibble, A. M. Chippindale, A. H. Pohl, A. C. Hannon, *Angew. Chem. Int. Ed.* **2007**, *46*, 7116–7118.
56. R. Ohtani, H. Matsunari, T. Yamamoto, K. Kimoto, M. Isobe, K. Fujii, M. Yashima, S. Fujii, A. Kuwabara, Y. Hijikata, S. Noro, M. Ohba, H. Kageyama, S. Hayami, *Angew. Chem. Int. Ed.* **2020**, *59* , 19254–19259.
57. A.-H. Yuan, R.-Q. Lu, H. Zhou, Y.-Y. Chen, Y.-Z. Li, *CrystEngComm* **2010**, *12*, 1382–1384.
58. W. Kaneko, S. Kitagawa, M. Ohba, *J. Am. Chem. Soc.* **2007**, *129*, 13706–13712.

59. N. Yanai, W. Kaneko, K. Yoneda, M. Ohba, S. Kitagawa, *J. Am. Chem. Soc.* **2007**, *129*, 3396–3397.
60. M. Ohba, H. Ōkawa, *Chem. Rev.* **2000**, *198*, 313–328.

Chapter 2

Guest-induced Magnetic Phase Switching in Dianion-based Flexible Porous Magnets

Abstract

Novel porous magnets of type $[Ni^{II}(dmen)_2]_2[Fe^{III}(CN)_6](A)_{0.5}\cdot 7H_2O$ (dmen = 1,1-dimethylethylenediamine, A^{2-} = 1,5-anthraquinonedisulfonate ($AQDS^{2-}$; **1_H$_2$O**) or = Azobenzene-4,4'-dicarboxylate ($AZDC^{2-}$; **2_H$_2$O**)) were synthesized. These compounds possessed different packing structures consisting of cationic 2-D layers extended by Fe^{III}-CN-Ni^{II} linkages and A^{2-} weakly interacted the layers as a pillar-anion. **1_H$_2$O** formed a pseudo 3-D pillared-layer type structure, in which the dianions were located at each interlayer space uniformly. In contrast, **1_H$_2$O** possessed a double-layer type framework with different interlayer structure, and $AZDC^{2-}$ weakly linked the layers as a pseudo-pillar-anion. Significant structural changes with guest uptake and release were confirmed by *in situ* powder X-ray diffraction measurements in both compounds. Furthermore, *in situ* magnetic measurements under guest atmosphere revealed that the magnetic phase of **1** and **2** changed depending on the guest molecules. Dehydrated forms of **1** and **2** exhibited metamagnetic behavior around 10 K based on a ferromagnetic intralayer interaction between Ni^{II} and low-spin Fe^{III} and an antiferromagnetic interlayer interaction After adsorbing H_2O and MeOH in **1**, ferromagnetic ordering with shifts of ordering temperature was observed. On the other hand, **2** exhibited two-steps CO_2 adsorption with gate-adsorption around P_{CO2} = 85 kPa. *In situ* magnetic measurements under CO_2 revealed that the ferromagnetic behavior appeared at P_{CO2} = 100 kPa. The flexible framework including the pillar dianions successfully converted the magnetic phase through the interlayer structural change accompanying guest adsorption.

Introduction

Chemo-switchable magnetic materials have attracted much attention because of their potential for applications such as chemical sensors and memory devices.[1-5] Recently, porous materials based on porous coordination polymers (PCPs) or metal-organic frameworks (MOFs) are expected to be stimuli-responsive materials for interlocking porosity-related functions and physical properties based on their highly regular, flexible and designable structures.[6-9] Indeed, the number of reports on MOFs showing magnetic variability for guest molecules have been investigated.[10-17] Several mechanisms of guest-induced magnetic phase conversion have been explored;[18-29] however, establish of promising guideline for magnetic-MOF design to guest molecules remains challenging due to a trade-off relationship between the short intermetallic distances for efficient magnetic interactions and the extended ligand length favorable for porosity.

Herein, we demonstrate the design of novel flexible porous magnets showing magnetic phase conversion through significant structural changes driven by guest molecules. We prepared two types of porous magnets consisting of cationic magnetic layers $[\{Ni^{II}(L)_2\}_2\{Fe^{III}(CN)_6\}]^+$ and dianions as pseudo-pillars. The magnetic layers with monoanions have been reported by our group, in which the magnetic properties of the framework were depended on weak interlayer interactions arising from the interlayer distance.[30] The dianion-based porous magnets were synthesized for the purpose of (i) constructing flexible and porosity-rich magnetic materials, (ii) interconnecting magnetic layers in the ionic MOFs, and (iii) control the interlayer distance with guest molecule. We selected a rigid dianion, 1,5-anthraquinonedisulfonate ($ADQS^{2-}$), as a pseudo-pillar ligand for the abovementioned purposes, and pseudo three-dimensional (3-D) porous magnet was rationally prepared.[31]

Furthermore, we achieved CO_2-induced magnetic phase switching from antiferromagnetic to ferromagnetic phases using a novel double-later type porous magnet. CO_2 is one of the most attracted sensing target because of the environmental problems associated with the increasing concentration of CO_2 in the atmosphere.[32,33] From this perspective, a novel CO_2-responsive porous magnet was synthesized rationally by incorporation of interaction site for CO_2 molecules. We selected a pseudo-pillar dianion, Azobenzene-4,4'-dicarboxylate ($AZDC^{2-}$), because the dipole–quadrupole interactions between polarizable CO_2 molecule and the accessible nitrogen site have been reported.[34-36] Furthermore, theoretical and experimental studies have also been shown that nitrogen donor groups in the framework enhance the CO_2 adsorption capacity and selectivity, indicating the ideal adsorbents for CO_2 capture.[37-52]

Experimental Section

Materials

All chemicals were purchased from commercial sources and used without further purification. Precursor complex, $[Ni^{II}(dmen)_3]Cl_2$ (dmen = 1,1-dimethylethylenediamine, $H_2NC(CH_3)_2CH_2NH_2$) was prepared according to literature method.[30] $[Ni^{II}(dmen)_2]_2[Fe^{III}(CN)_6](AQDS)_{0.5}\cdot 7H_2O$ (**1_H2O**; $AQDS^{2-}$ = 1,5-anthraquinonedisulfonate) and $[Ni^{II}(dmen)_2]_2[Fe^{III}(CN)_6](AZDC)_{0.5}\cdot 7H_2O$ (**2_H2O**; $AZDC^{2-}$ = Azobenzene-4,4'-dicarboxylate) were prepared by following steps.

Single Crystals of $[Ni^{II}(dmen)_2]_2[Fe^{III}(CN)_6](AQDS)_{0.5}\cdot 7H_2O$ (1_H2O)

1_H2O was prepared by a liquid phase diffusion method in a straight tube. A solution of $[Ni^{II}(dmen)_3]Cl_2$ (40 mg, 0.1 mmol) and Na_2AQDS (10.3 mg, 0.025 mmol) in H_2O (10 mL) were added to a solution of $K_3[Fe^{III}(CN)_6]$ (16 mg, 0.05 mmol) in H_2O (10 mL) at room temperature. The solution was allowed to stand for several weeks and the brown crystals were obtained. Yield: 72 %. Elemental analysis (%); Calcd. for $C_{29}H_{45}N_{14}SO_{9.5}Ni_2Fe$: C 36.24, H 6.19, N 20.40; found: C 36.25, H 6.42, N 20.45.

Single Crystals of $[Ni^{II}(dmen)_2]_2[Fe^{III}(CN)_6](AZDC)_{0.5}\cdot 7H_2O$ (2_H2O)

2_H2O was prepared by a liquid phase diffusion method in a straight tube. A solution of $[Ni^{II}(dmen)_3]Cl_2$ (40 mg, 0.1 mmol) and Na_2AZDC (15.7 mg, 0.025 mmol) in H_2O (10 mL) were added to a solution of $K_3[Fe^{III}(CN)_6]$ (16 mg, 0.05 mmol) in H_2O (10 mL) at room temperature. The solution was allowed to stand for several days and the brown crystals were obtained. Yield: 64 %. Elemental analysis (%); Calcd. for $C_{29}H_{54}N_{15}O_3Ni_2Fe$: C 41.76, H 6.53, N 25.19; found: C 41.87, H 6.45, N 24.76.

Powder Samples of 1 and 2

The dehydrated powder samples of **1** and **2** were prepared by heating **1_H2O** and **2_H2O** under vacuum at 400 K for 6 h for **1_H2O** and at 420 K for 12 h for **2_H2O**.

Powder Samples of 1_MeOH

The powder samples of methanol clathrate (**1_MeOH**) were prepared via a vapor diffusion method. The dehydrated powder samples of **1** were placed under MeOH vapor for 3 h.

Physical Measurements

Elemental analyses of carbon, hydrogen and nitrogen for $[Ni^{II}(dmen)_2]_2[Fe^{III}(CN)_6](A)_{0.5}\cdot 7H_2O$ (dmen = 1,1-dimethylethylenediamine, A^{2-} = 1,5-anthraquinonedisulfonate ($AQDS^{2-}$; **1_H_2O**) or = Azobenzene-4,4'-dicarboxylate ($AZDC^{2-}$; **2_H_2O**)) were carried out at the division of graduate school of science in Kyushu University. Infrared (IR) spectra were recorded with a JASCO FT/IR-4200 spectrophotometer with an ATR accessory. Thermal gravimetric analysis (TGA) was performed using a Perkin Elmer STA6000 instrument, in the temperature range of 30–700°C, under N_2 atmosphere (heating rate: 5°C min^{-1}). PXRD patterns at room temperature were collected on a Rigaku Ultima IV spectrometer using a reflection-free sample holder (λ = 1.5418 Å). *In situ* PXRD measurements for dehydrated **1** and **2** were conducted under vacuum with a glass capillary connected to a homemade adsorption equipment. *In situ* variable-pressure powder X-ray structural analysis (VP-PXRD) of **2** was carried out using a Rigaku Smart Lab with Cu−Kα radiation (λ = 1.54178 Å) connected to BELSORP-18PLUS volumetric adsorption equipment. Adsorption and desorption isotherms were acquired using a BELSORP-MAX volumetric adsorption equipment (Microtrac BEL Corp.). The magnetic properties were investigated using a Quantum Design MPMS-XL5R SQUID. The samples were put into a gelatin capsule, placed in a plastic straw, and then fixed to the end of the sample transport rod. *In situ* magnetic measurements were carried out using a Quantum Design MPMS-XL5R SQUID connected to an adsorption device (BELSORP-min II-PR). The samples were put into a homemade sample cell, and then fixed to the end of the sample transport rod. Diamagnetic correction was calculated by using Pascal constant.[53] The molar magnetic susceptibility ($\chi_M = M/H$) were corrected for the diamagnetism of the constituent atoms and the sample tube. The temperature dependence of field cooled magnetization (FCM) curves were measured in the temperature range of 2–30 K under an applied magnetic field of 10 Oe. The field-dependence of magnetization curves were measured in the field range of -5 T to 5 T at 2 K. Temperature dependence of alternating-current (ac) magnetic susceptibilities (χ'_M = in phase, χ''_M = out of phase) were measured in the frequency range of 1–100 Hz under a zero dc field and an oscillating field of 3 Oe.

Single-crystal X-ray diffraction

Single-crystal X-ray diffraction data of **1_H_2O** and **2_H_2O** were collected on a Bulker SMART APEX II ULTRA CCD-detector Diffractometer, a rotating-anode (Bruker Tourbo X-ray source) with graphite-monochromated MoK_α radiation (λ = 0.71073 Å) was used. Computations were carried out on APEX2 crystallographic software package and OLEX2 software.[54] A single crystal was mounted on a polymer film with liquid paraffin and the temperature kept constant under flowing N_2 gas. The structure of **1_H$_2$O** was solved by a standard direct method (XSHELL V6.3.1 crystallographic software package of the Bruker AXS) and expanded Fourier techniques. Full-matrix least-squares refinements were carried out with anisotropic thermal parameters for all non-disordered and non-hydrogen atoms. All of the hydrogen atoms were placed in the measured positions and refined using a riding model. Relevant crystal data collection and refinement data for the crystal structure of **1_H$_2$O** (CCDC 2063060) and **2_H$_2$O** are summarized in Table 1 and Table 2.

Table 1. Crystallographic data and refinement parameter for **1_H_2O**

	1_H_2O CCDC 2063060
Formula	$C_{29}H_{48}N_{14}SO_{11}Ni_2Fe$
Temperature / K	100
Crystal system	Monoclinic
Space group	$P2_1/n$
a / Å	14.205(2)
b / Å	21.812(2)
c / Å	14.694(2)
α / °	90
β / °	90.464(1)
γ / °	90
V / Å^3	4552.7(8)
Z	4
Goodness of Fit	1.046
R_1	4.57
wR_2	13.2

Table 2. Crystallographic data and refinement parameter for **2_H_2O**

	2_H_2O
Formula	$C_{29}H_{52}N_{15}O_9Ni_2Fe$
Temperature / K	196
Crystal system	Triclinic
Space group	$P\overline{1}$
a / Å	10.3404(16)
b / Å	10.4112(16)
c / Å	21.615(3)
α / °	102.089(2)
β / °	97.493(2)
γ / °	96.179(2)
V / Å^3	2234.0(6)
Z	2
Goodness of Fit	1.052
R_1	5.30
wR_2	14.96

Crystal Structure of 1_H_2O and 2_H_2O

Dianion-based porous magnets, $[Ni^{II}(dmen)_2]_2[Fe^{III}(CN)_6](A)_{0.5}\cdot 7H_2O$ (dmen = 1,1-dimethylethylenediamine, A^{2-} = 1,5-anthraquinonedisulfonate ($AQDS^{2-}$; **1_H_2O**) or = Azobenzene-4,4’-dicarboxylate ($AZDC^{2-}$; **2_H_2O**)) were synthesized by slow diffusion of an aqueous solution of $[Ni(dmen)_3]Cl_2$, $K_3[Fe(CN)_6]$ and Na_2AQDS or Na_2AZDC. Powder samples of **1_H_2O** and **2_H_2O** for physical measurements were prepared for characterization by mixing the same components in water. In the synthesis process, the slow dissociation of $[Ni(dmen)_3]^{2+}$ into $[Ni(dmen)_2]^{2+}$ in aqueous solution leads to the growth of crystals in a self-assembling process (Scheme 1).

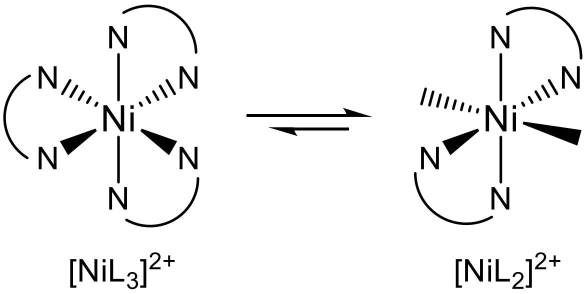

Scheme 1 Dissociation of $[NiL_3]^{2+}$ into $[NiL_2]^{2+}$

Single crystal X-ray diffraction (SCXRD) analysis revealed that **1_H₂O** possessed a pseudo 3-D pillared-layer-type structure derived from cationic two-dimensional (2-D) $[\{Ni^{II}(dmen)_2\}_2\{Fe^{III}(CN)_6\}]^+$ layers and dianions ($AQDS^{2-}$), in which $AQDS^{2-}$ was located between grid-like pillar layers uniformly (Fig. 1, Table 1). Solvent-accessible void space was calculated at 14.7 % by using *PLATON/VOID* software.[55] Thermogravimetric analysis (TGA) of **1_H₂O** indicated the removal of all lattice water molecules in **1_H₂O** below 420 K (Fig. 2). The crystalline powder samples of **1** was obtained by heating **1_H₂O** at 400 K under vacuum. The activation treatment of **1_H₂O** induced a remarkable diffraction peak shifts to higher angles, suggesting the shrinkage of the framework (Fig. 3). The cell parameters of **1** was calculated using FOX and RIETAN-FP software,[55,56] resulting in $a = 13.8370(10)$ Å, $b = 20.268(11)$ Å, $c = 14.594(12)$ Å, $\beta = 90.155(14)°$ at 298 K (Fig. 4).

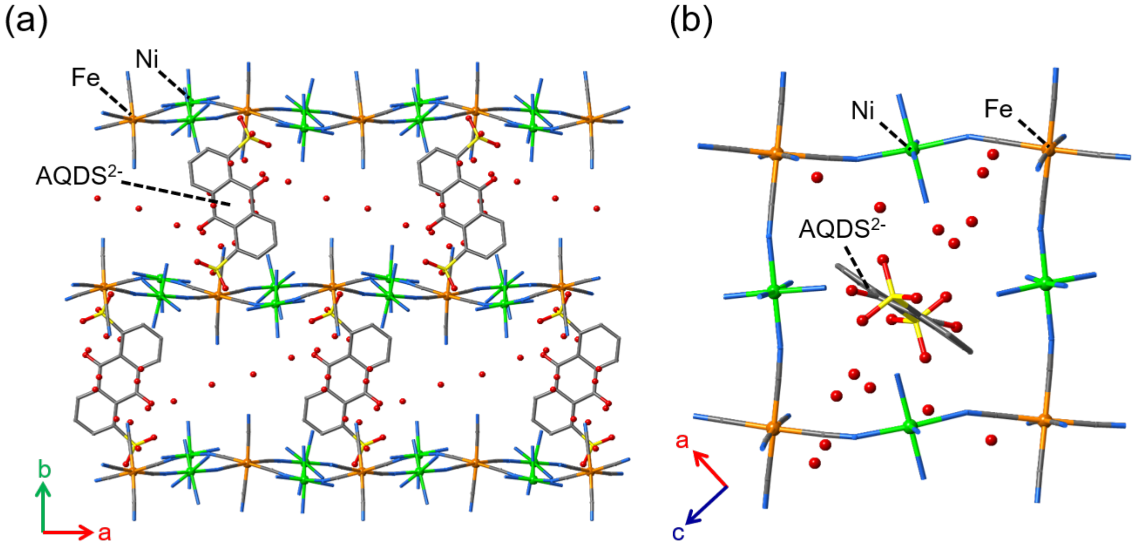

Fig. 1 Crystal structure of **1_H₂O** viewed along the (a) *c*-axis and (b) *b*-axis. Atomic code: Fe, orange; Ni, green; C, grey; N, blue; O, red; S, yellow, respectively. C atoms of dmen and all H atoms are omitted for clarity.

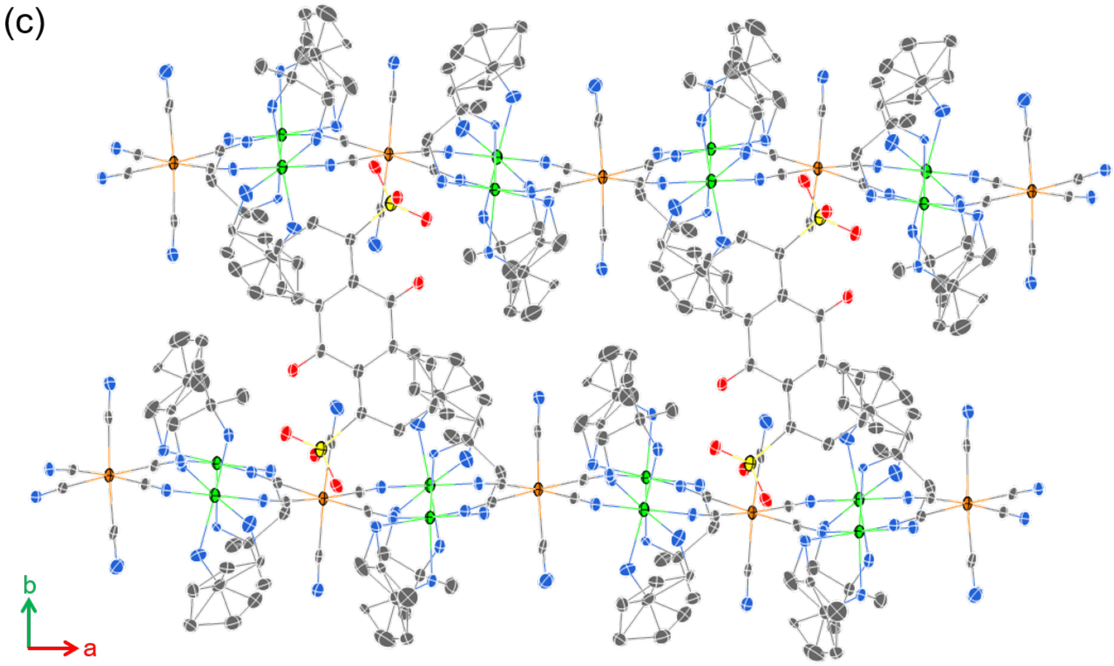

Fig. 1 (c) An ORTEP drawing of the crystal structure for **1_H$_2$O** from a view along c-axis. Atomic code: Fe, orange; Ni, green; C, grey; N, blue; O, red; S, yellow, respectively. Lattice solvents and H atoms are omitted for clarity. Thermal ellipsoids are shown at the 50% probability level.

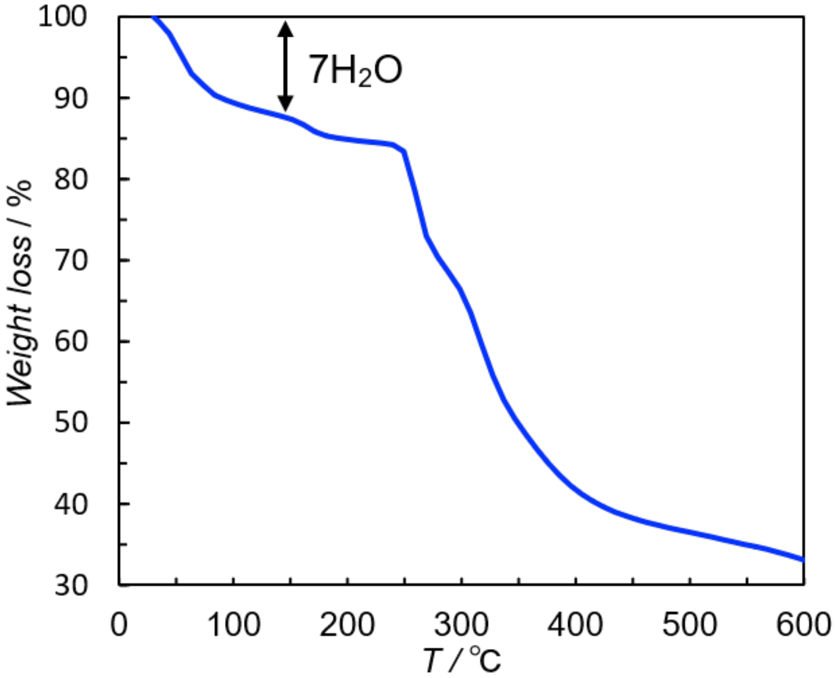

Fig. 2 TGA curve of **1_H$_2$O**

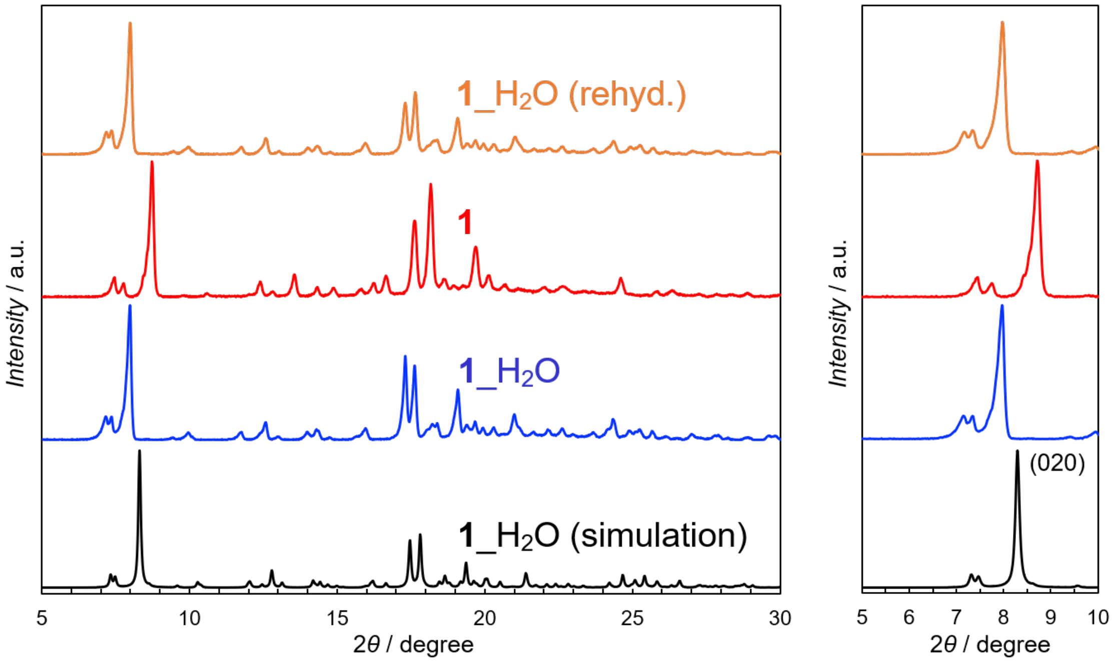

Fig. 3 PXRD patterns of **1_H₂O** (blue), **1** (red), **1_H₂O** (rehyd.) (orange) and simulated pattern of **1_H₂O** (black)

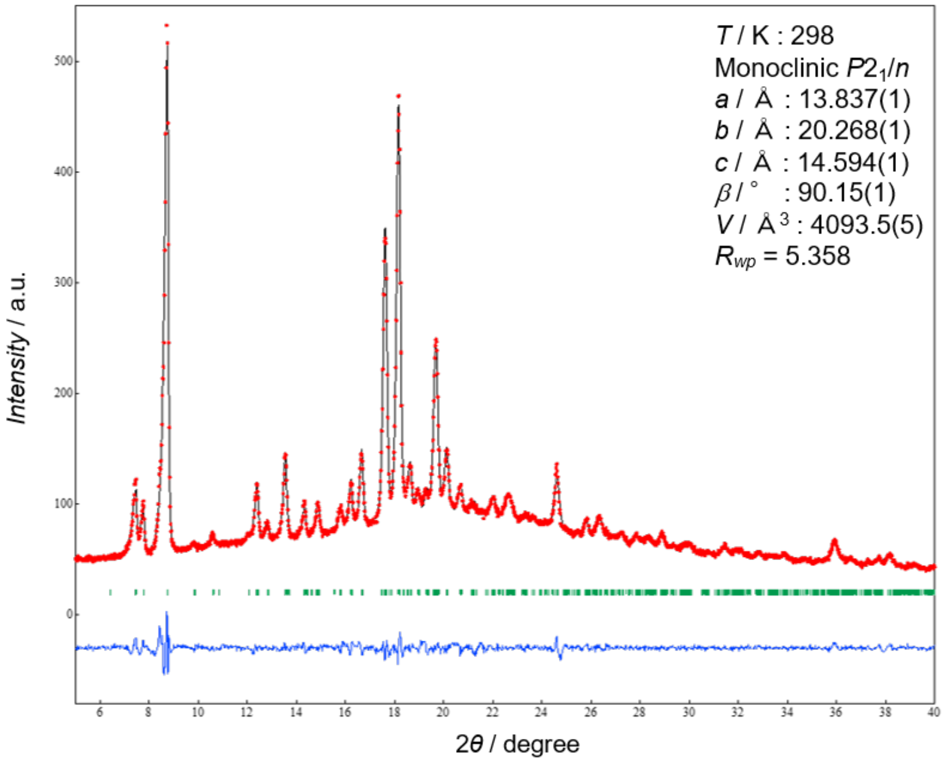

Fig. 4 Le Bail analysis of **1** under vacuum at 298 K with the result of PXRD pattern (λ = 1.5418 Å). Red dots, black line, and blue line represent the observed plots, calculated pattern, and their difference, respectively. Green bars are the calculated positions of the Bragg reflections.

SCXRD analysis revealed that **2_H₂O** formed a double-layer type framework structure in which AZDC^{2-} weakly interact with layers as a pseudo-pillar-anion (Fig. 5, Table 2). TGA of **2_H₂O** suggested that the removal of all lattice water molecules in **2_H₂O** below 420 K (Fig. 6). The crystalline powder samples of **2** was obtained by heating **2_H₂O** at 420 K under vacuum. The activation treatment of **2_H₂O** induced a remarkable diffraction peak shifts to higher angles, suggesting the shrinkage of the framework (Fig. 7). The cell parameters of **1** was calculated using FOX and RIETAN-FP software,[55,56] resulting in a = 10.187(2) Å, b = 10.362(11) Å, c = 20.970(6) Å, α = 102.92(6)°, β = 98.39(4)°, γ = 91.45(6)° at 298 K (Fig. 8).

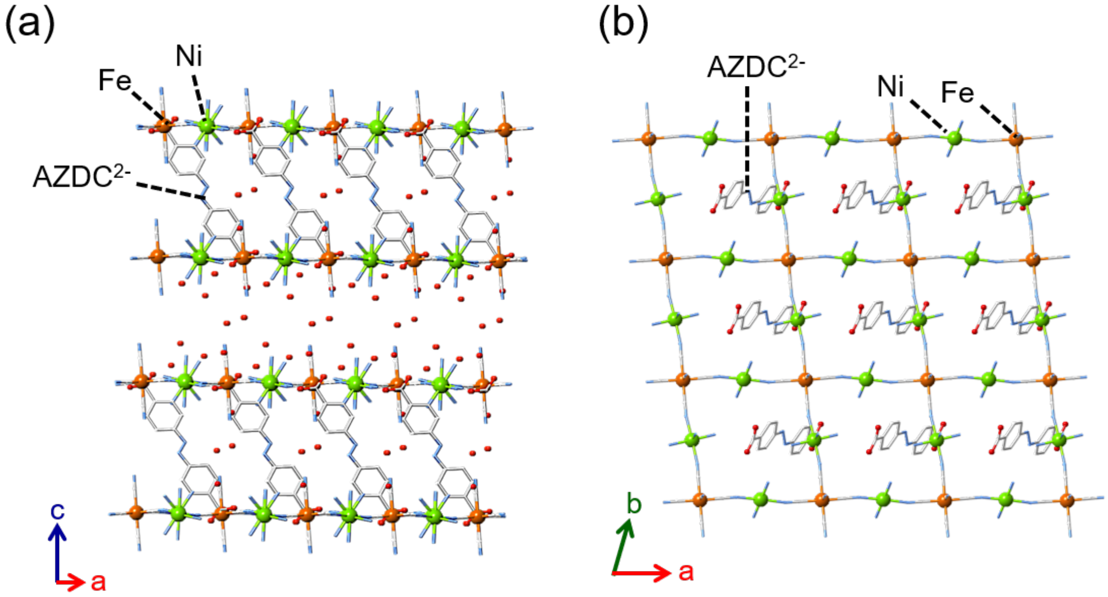

Fig. 5 Crystal structure of **2_H₂O** viewed along the (a) *b*-axis and (b) *c*-axis. Atomic code: Fe, orange; Ni, green; C, grey; N, blue; O, red, respectively. C atoms of dmen and all H atoms are omitted for clarity.

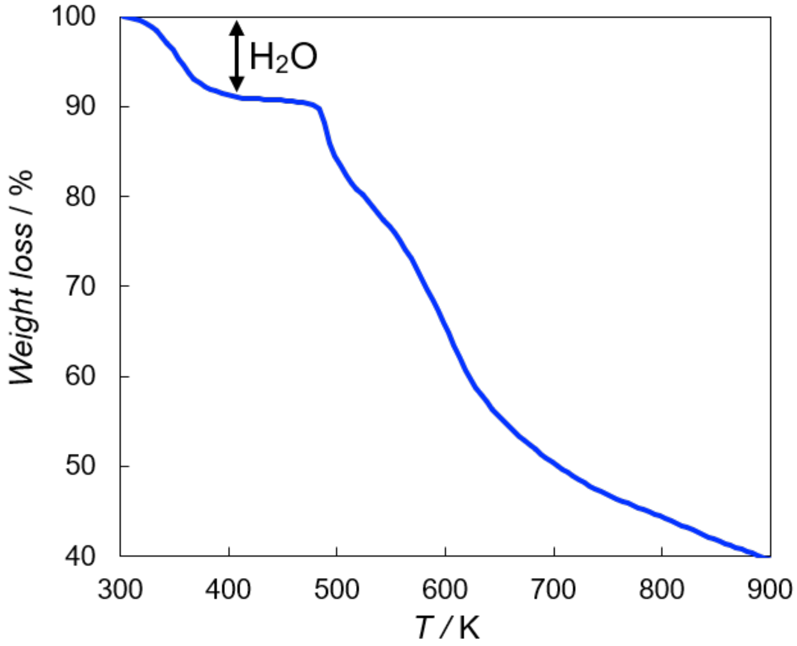

Fig. 6 TGA curve of **2_H$_2$O**

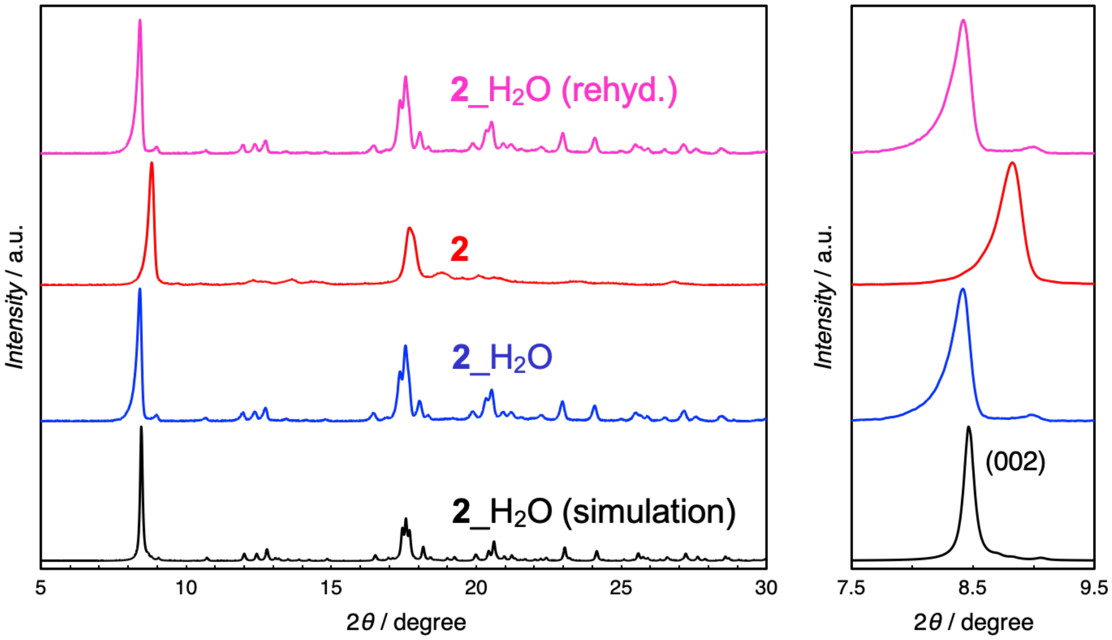

Fig. 7 PXRD patterns of **2_H$_2$O** (blue), **2** (red), **2_H$_2$O** (rehyd.) (pink) and simulated pattern of **2_H$_2$O** (black)

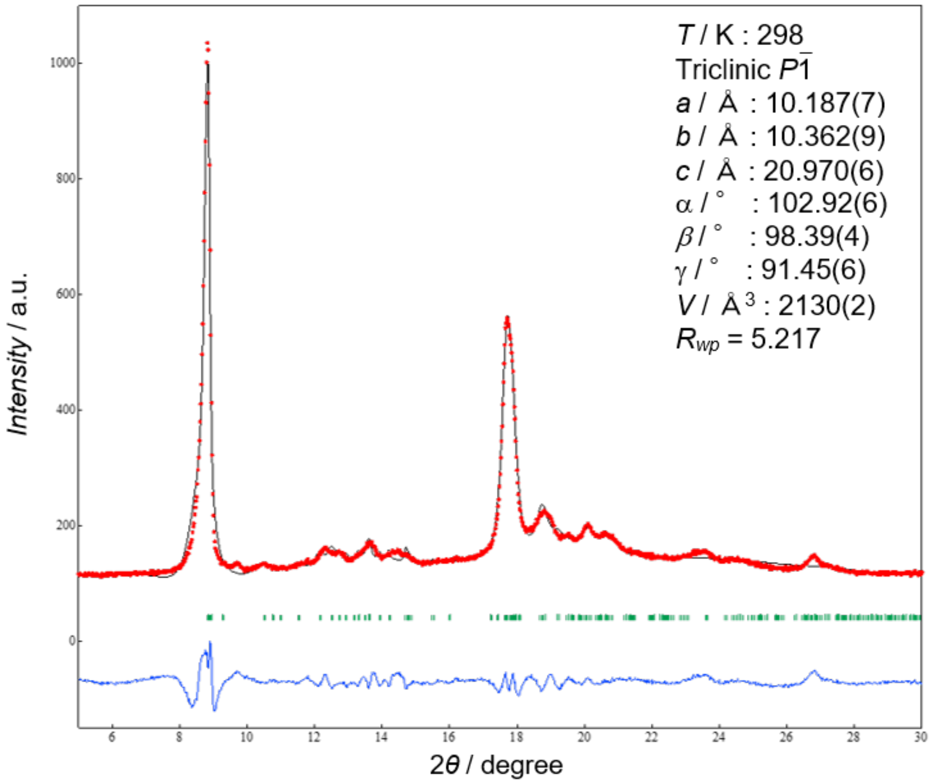

Fig. 8 Le Bail analysis of **2** under vacuum at 298 K with the result of PXRD pattern (λ = 1.5418 Å). Red dots, black line, and blue line represent the observed plots, calculated pattern, and their difference, respectively. Green bars are the calculated positions of the Bragg reflections.

Guest-responsivities of 1 and 2

The guest-responsivities of **1** and **2** was investigated through adsorption, PXRD and magnetic studies. The adsorption and desorption profiles of **1** for H_2O, MeOH, and EtOH at 298 K are shown in Fig. 9. **1** exhibited two-step adsorption behavior for H_2O in which an abrupt adsorption was observed in the initial adsorption process ($P/P_0 < 0.3$). In contrast, the gate-opening behavior was observed in the second phase ($P/P_0 > 0.8$). The saturated amount of adsorbed water was 6.78 mol/mol, collaborating the result of SCXRD analysis (Fig. 1, Table 1). On the other hand, **1** exhibited one-step MeOH adsorption behavior with gate-opening ($P/P_0 = 0.3$), while EtOH was not adsorbed unlike H_2O and MeOH.

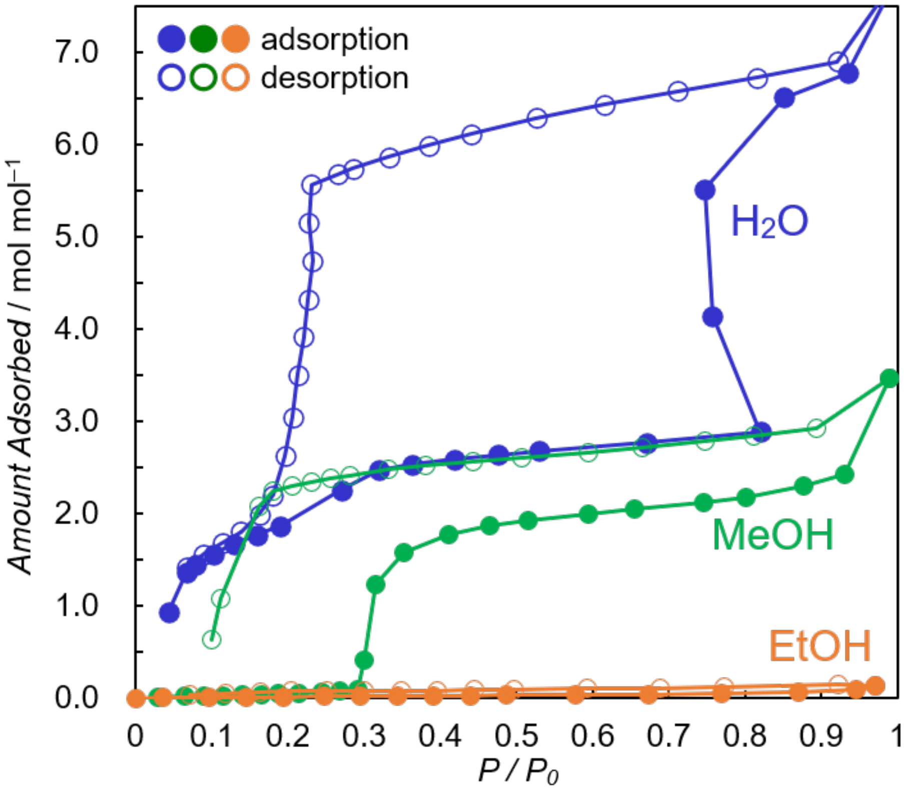

Fig. 9 Adsorption/desorption isotherms of **1** for H_2O (blue), MeOH (green) and EtOH (orange) at 298 K. The filled and open circles display the adsorption and desorption processes, respectively. Solid lines represent a guide for easier viewing.

The differences in adsorption behaviors of **1** were revealed by considering the environment of the guest-accessible pores. The space-filling model of **1_H_2O** indicated that the methyl groups of dmen were exposed on the pore surface, leading to the construction of bottleneck-type pores with narrow entrances for guest molecules (Fig. 10(a)). The size-selective guest adsorption behaviors were caused by the restricted pore size (Fig. 10(b), Fig. 11).[58] Thus, MeOH molecules required a higher vapor pressure compared to H_2O molecules due to the narrow accessible space in **1**. EtOH molecules were not adsorbed due to the size limitation imposed by the narrow entrance. Also, gaseous molecules, such as N_2 and CO_2, were not adsorbed due to weak interaction (Fig. 12).

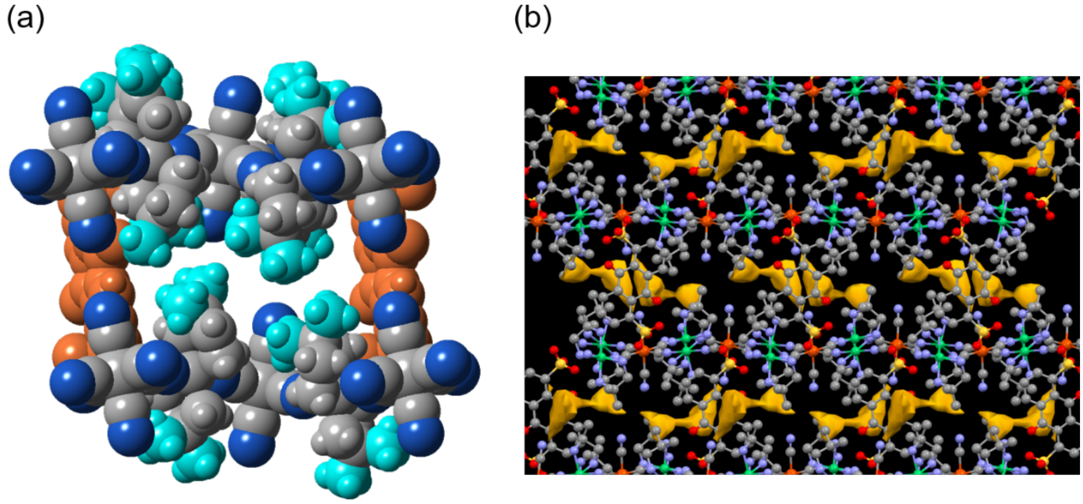

Fig. 10 (a) The space filling model of **1_H_2O** viewed along the *a*-axis. Orange, light blue, blue and grey colours in the framework represent $AQDS^{2-}$, dmen methyls, N atoms of $[Fe(CN)_6]^{3-}$, and the remaining atoms, respectively. H_2O molecules are omitted for clarity. (b) The bottleneck-type pores of **1_H_2O** with guest-accessible surface viewed along the *c*-axis. Atomic code: Fe, orange; Ni, green; C, grey; N, blue; O, red; S, yellow. H and O atoms of H_2O molecules are omitted for clarity.

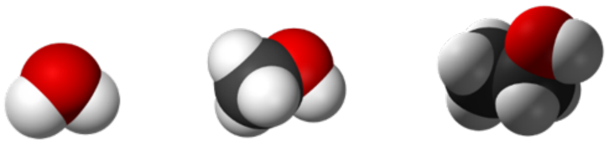

	H_2O	MeOH	EtOH
Kinetic diameter (Å)	2.641	3.626	4.530

Fig. 11 Kinetic diameter of H_2O, MeOH and EtOH[36]

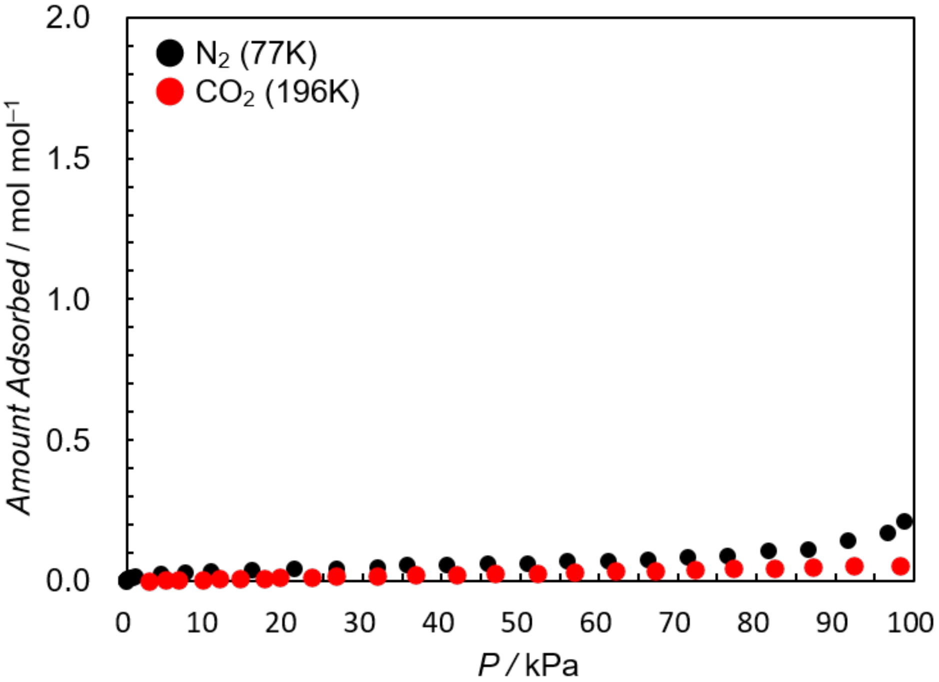

Fig. 12 Adsorption isotherms of **1** for N_2 (black) and CO_2 (red). The filled circles display the adsorption process.

The structural changes with guest adsorption and desorption of **1** were confirmed by PXRD patterns. Rehydrated state of **1** (named as **1_H$_2$O** (rehyd.)) and the methanol-adsorbed state (**1_MeOH**) were obtained by a vapor diffusion method. **1_H$_2$O** (rehyd.) formed a similar structure that of **1_H$_2$O**, suggesting the reversible structural changes dehydration and hydration treatment (Fig. 3). Notably, the (020) plane corresponding to the interlayer distance shifted with water uptake and release (Fig. 13). The interlayer distances (*d*) of were calculated by Bragg's law,[59] resulting in the values of 10.14 Å (**1_H$_2$O**) and 11.08 Å (**1**), respectively (Table 3). Hence, the resultant *d* values reflected the flexibility of the pseudo-pillared-layer structure, leading to gate-opening behavior. **1_MeOH** also showed analogous interlayer expansion, in which the *d* value of **1_MeOH** was 10.89 Å.

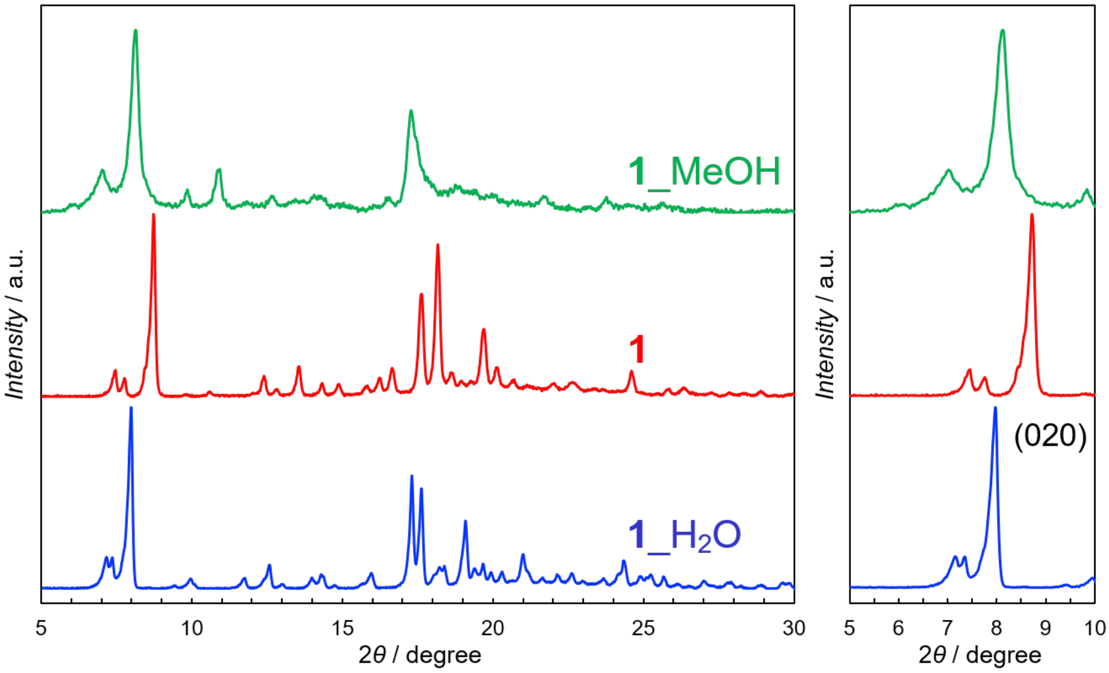

Fig. 13 PXRD patterns of **1_H$_2$O** (blue), **1** (red), and **1_MeOH** (green) at 298 K

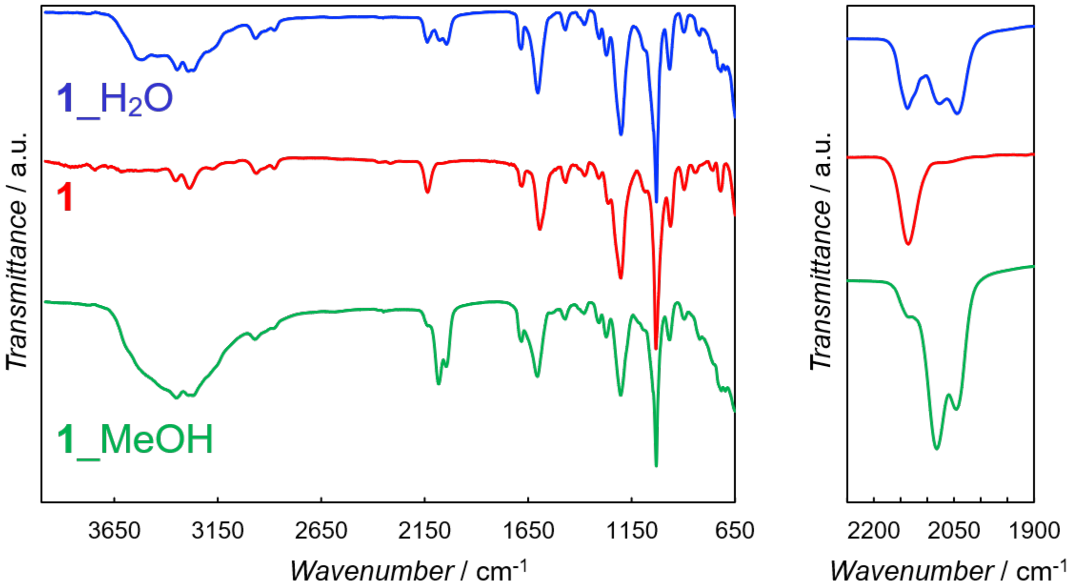

Fig. 14 IR spectra of (a) **1_H$_2$O** (blue), **1** (red), **1_MeOH** (green)

Table 3 Diffraction angles (2*θ*) of the (020) diffraction peak and interlayer distances (*d*) of **1_H$_2$O**, **1**, and **1_MeOH**.

Sample	2θ/degree	d/Å [a]
1_H$_2$O	7.98	11.08
1	8.72	10.14
1_MeOH	8.12	10.89

[a] Interlayer distance (d) was estimated from the equation $d = n\lambda/2\sin\theta$, where n and λ represent an integer and the X-ray wavelength, respectively.

The H_2O-responsivity of **2** was investigated through adsorption, PXRD and magnetic profiles. The adsorption and desorption profiles of **2** for H_2O at 298 K are shown in Fig. 15. **2** displayed an abrupt H_2O adsorption from the low-humidity region, in which the saturated amount of adsorbed H_2O (7.12 mol/mol), collaborating the result of SCXRD analysis (Fig. 5, Table 2). Rehydrated state of **2** (**2_H_2O** (rehyd.)) was obtained via a vapor diffusion method. **2_H_2O** (rehyd.) formed a similar structure that of **2_H_2O**, suggesting the reversible structural changes dehydration and hydration treatment (Fig. 7). Notably, the (002) plane corresponding to the interlayer distance shifted with water uptake and release (Fig. 7).

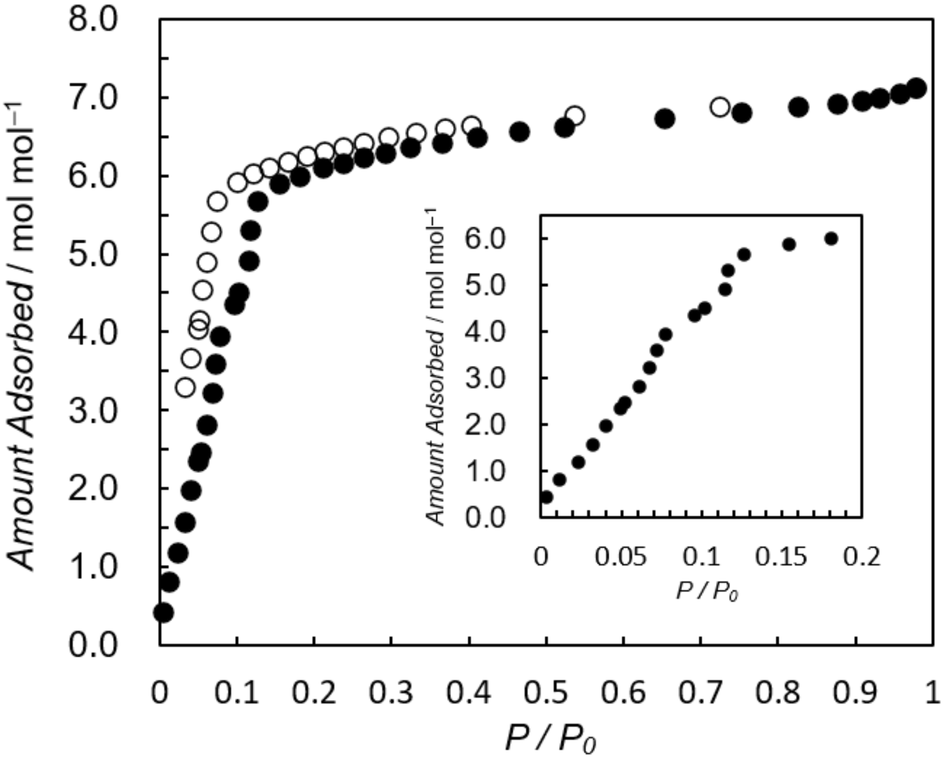

Fig. 15 Adsorption/desorption isotherms of **2** for H_2O at 298 K. The filled and open circles display the adsorption and desorption processes, respectively. Inset: low vapor pressure region.

The CO_2-responsivity of **1** was investigated via adsorption, *in situ* variable-pressure powder X-ray structural analysis (VP-PXRD) and *in situ* magnetic measurements. **1** exhibited two-step CO_2 adsorption with 1st physical adsorption ($P_{CO2} < 50$ kPa) and 2nd gate-opening behavior ($P_{CO2} > 85$ kPa) at 196 K (Fig. 16). Furthermore, hysteric adsorption and desorption profiles indicate that the strong host-guest interaction was operated in the framework.

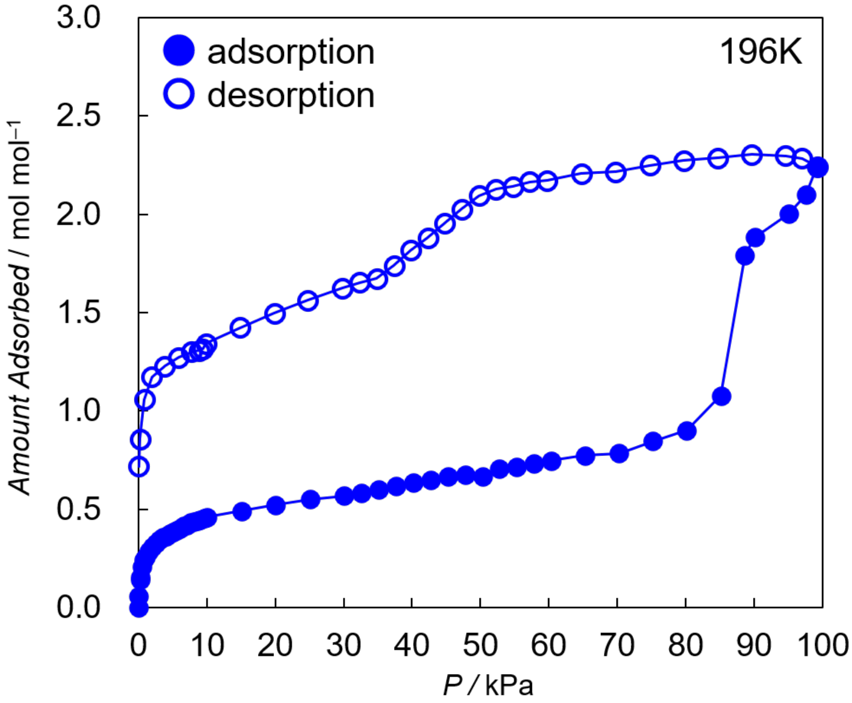

Fig. 16 Adsorption isotherms of **2** for CO_2 at 196 K. The filled and open circles display the adsorption and desorption processes, respectively. Solid lines represent a guide for easier viewing.

CO_2-induced structural changes in **2** were monitored by *in situ* variable-pressure powder X-ray structural measurement (VP-PXRD) at 196 K. **2** was prepared via activation treatment by heating at 420 K for 12 h before the measurements. The PXRD pattern of CO_2-adsorbed sample at $P_{CO2} = 50$ kPa (**2**$\supset$$CO_2$ (50 kPa)) showed the similar to the dehydrated , indicating that the large structural change was not occurred in the 1st CO_2 adsorption process (Fig. 17). In contrast, CO_2-adsorbed state at $P_{CO2} = 100$ kPa (**2**$\supset$ CO_2 (100 kPa)) exhibited the remarkable peak shift to lower angles, demonstrating the interlayer expansion with 2nd CO_2 adsorption step (Fig. 17). The interlayer distances (*d*) of **2**, **2**$\supset$$CO_2$ (50 kPa) and **2**$\supset$$CO_2$ (100 kPa) were calculated by Bragg's law,[59] resulting in the values of 9.71 Å, 10.01 Å and 11.26 Å, respectively (Table 4). Hence, the resultant *d* values reflected the flexibility of the double-layer structure, leading to gate-opening behavior.

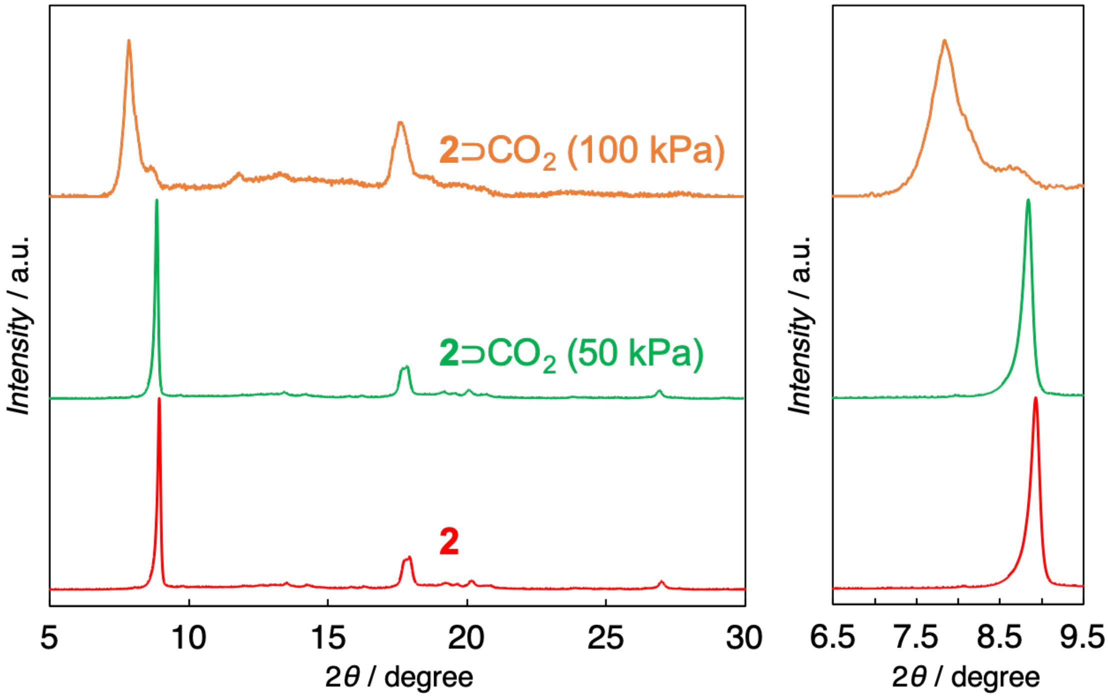

Fig. 17 PXRD patterns of **2** (red), **2**$\supset$CO$_2$ (50 kPa) (green), and **2**$\supset$CO$_2$ (100 kPa) (orange) at 196 K

Table 4 Diffraction angles (2θ) of the (020) diffraction peak and interlayer distances (d) of **2** , **2**$\supset$CO$_2$ (50 kPa), and **2**$\supset$CO$_2$ (100 kPa) at 196 K

Sample	2θ/degree	d/Å [a]
2	8.94	9.71
2$\supset$CO$_2$ (50 kPa)	8.83	10.01
2$\supset$CO$_2$ (100 kPa)	7.85	11.26

[a] Interlayer distance (d) was estimated from the equation $d = n\lambda/2\sin\theta$, where n and λ represent an integer and the X-ray wavelength, respectively.

Guest-induced Magnetic Phase Switching of 1 and 2

Magnetic profiles for **1** and its solvent adsorbed states (**1_H_2O** and **1_MeOH**) were investigated to explore the magnetic response with guest adsorption and desorption. Magnetic susceptibilities (χ_M) were measured under a dc magnetic field of 10 Oe. Temperature dependence of field-cooled magnetization (FCM) for **1**, **1_H_2O**, and **1_MeOH** are shown in Fig. 18(a). For guest-free **1**, the χ_M started to increase sharply at approximately 10 K, reaching a maximum of 82.5 cm^3mol^{-1} at 9 K, and then decreased to 2.9 cm^3mol^{-1} at 2 K upon cooling process. The resultant sharp peak of **1** indicated the occurrence of an antiferromagnetic ordering. Additionally, field dependence of the magnetization (*M*–*H*) curves at 2 K demonstrated that the magnetization value of **1** was 5.13 $N\beta$ at 5 T (Fig. 18(b)), which was consistent with that for two ferromagnetically coupled Ni(II) (S = 2/2) and one low-spin Fe(III) (S = 1/2) ions per $[\{Ni(dmen)_2\}_2\{Fe(CN)_6\}]^+$ unit. Importantly, ferromagnetic interaction based on the strict orthogonality between the magnetic dπ orbitals of the low-spin Fe(III) ion and the dσ orbitals of the Ni(II) ion is worked in the cationic 2-D sheets.[60] On the other hand, **1** exhibited a spin-flip behavior at approximately 250 Oe in the initial magnetization curve (Fig. 18(b) inset), that is, metamagnetic behavior.[61]

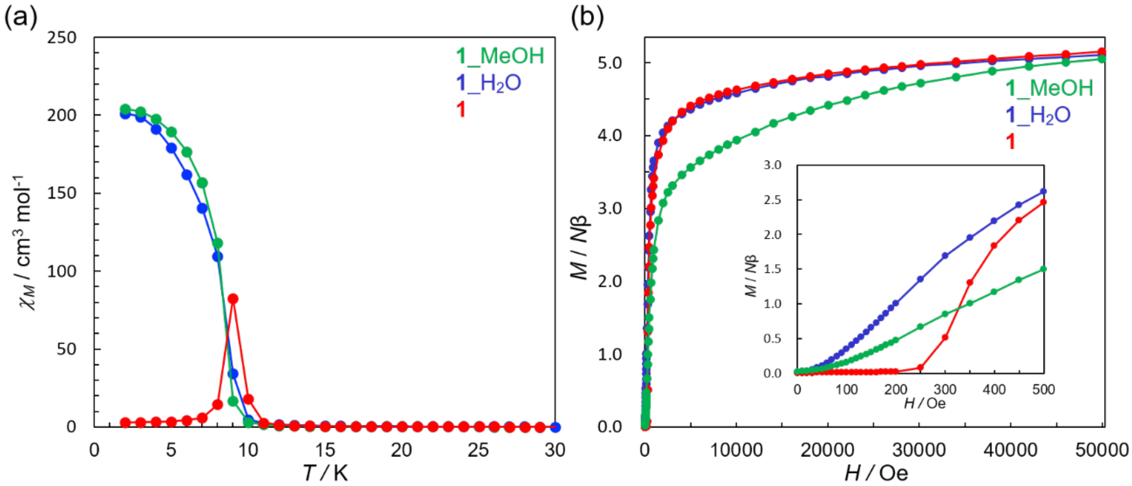

Fig. 18 Magnetic properties of **1** (red), **1_H_2O** (blue), and **1_MeOH** (green). (a) Temperature dependence of χ_M *vs* T plots under an applied magnetic field of 10 Oe. (b) Field dependence of magnetization curves at 2 K. Inset: low-magnetic field region.

Moreover, a magnetic hysteresis loop of **1** showed a coercive field (H_{c}) of 300 Oe in the applied external fields was in the range of -5 T to 5 T at 2 K (Fig. 19), indicating that **1** was categorized as a field-induced ferromagnet. The magnetic profile suggested the strong magnetic anisotropy of **1** due to its structural anisotropy, in which the ferromagnetic ordered spins were preserved by overcoming the antiferromagnetic interlayer interactions. Furthermore, temperature dependence of alternating-current (ac) magnetic susceptibilities (χ'_{M} = in-phase, χ''_{M} = out-of-phase) was measured to confirm the magnetic ordering. Fig. 20 depicts the χ'_{M} *vs.* T and χ''_{M} *vs.* T Plots for **1** in the frequency range of 1–100 Hz under a zero dc field and an oscillating field of 3 Oe. The single distinct peak of **1** without notable frequency dependence indicated that the phase transition temperature of **1** was determined to be 11 K and the long-range ordering of **1** might be caused by the partially produced spin-canted domains.

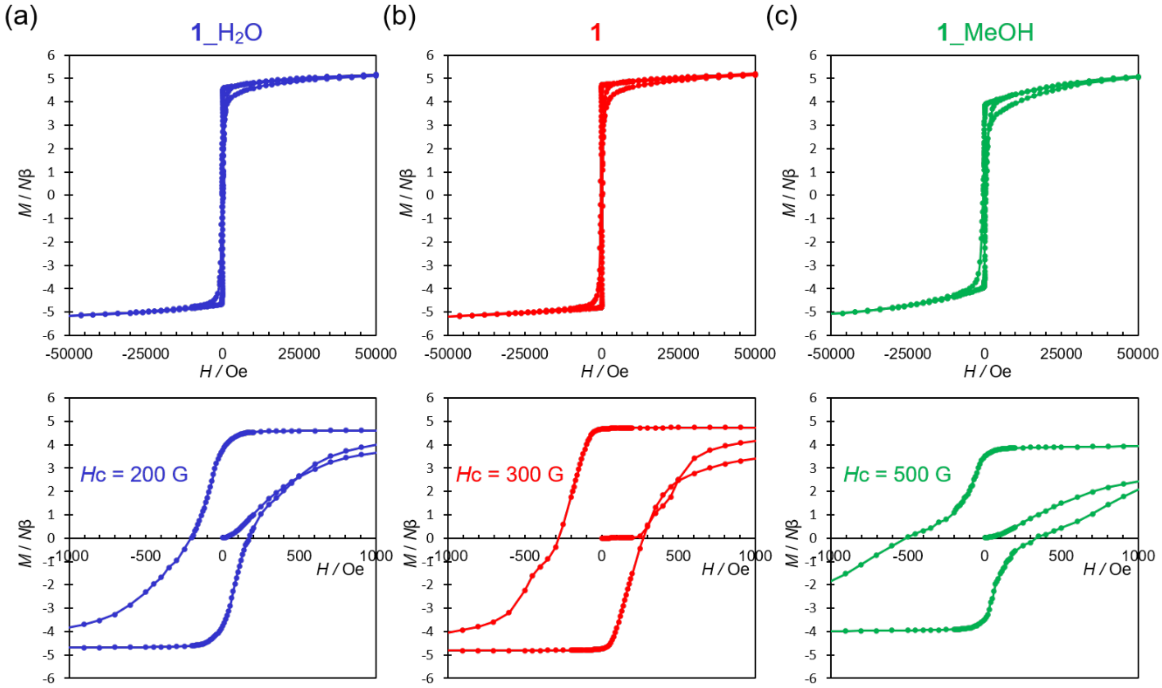

Fig. 19 Magnetic hysteresis curves of (a) **1_H$_2$O** (blue), (b) **1** (red) and (c) **1_MeOH** (green) at 2 K.

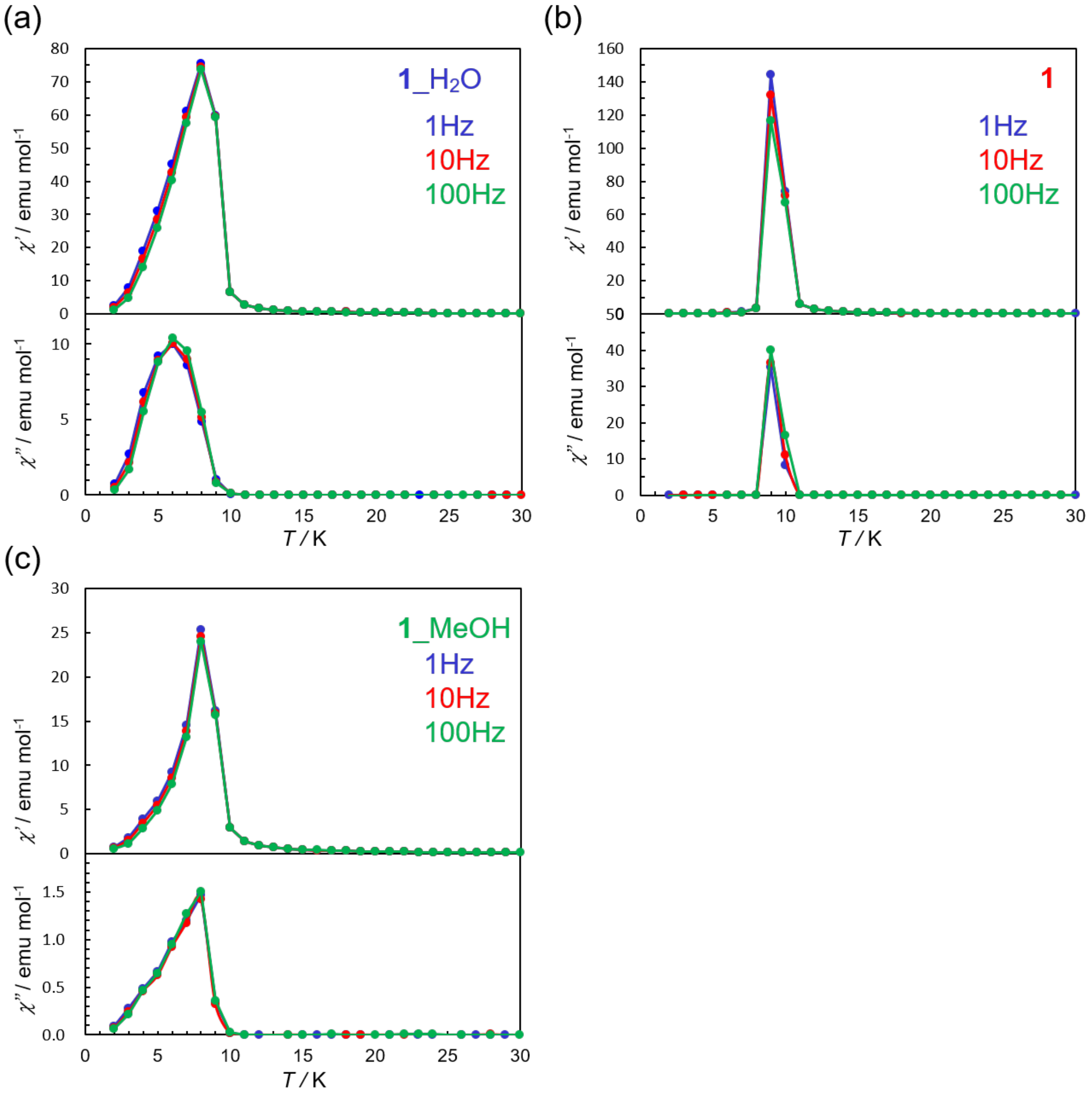

Fig. 20 Temperature dependence of χ'_{M} *vs*. *T* and χ''_{M} *vs*. *T* plots for (a) **1_H₂O**, (b) **1** and (c) **1_MeOH** measured in the frequency range of 1–100 Hz under a zero dc field and an oscillating field of 3 Oe (temperature range: 2–30 K).

In contrast, **1_H₂O** and **1_MeOH** exhibited abrupt increase of χ_M values at approximately 10 K upon cooling in which the maximum values of 201.2 cm^{3}mol^{-1} (**1_H₂O**) and 204.0 cm^3 mol^{-1} (**1_MeOH**) at 2 K, respectively (Fig. 18(a)). The resultant magnetic behaviors of **1_H₂O** and **1_MeOH** indicated the occurrence of a ferromagnetic ordering. Also, temperature dependence of ac magnetic susceptibilities of **1_H₂O** and **1_MeOH** demonstrated that the phase transition temperatures were determined to be 10 K (Figs. 20). **1_H₂O** and **1_MeOH** also possessed a ferromagnetic coupling in the cationic sheets, which was confirmed by the magnetization values of **1_H₂O** and **1_MeOH** at 5 T were 5.11 and 5.05 $N\beta$ (Fig. 18(b)). However, the degree of hysteresis loops with H_c of **1_H₂O** (200 Oe) and **1_MeOH** (500 Oe) were different, indicating the deference in the magnetic anisotropy originating from the intralayer structure (Fig. 21). Furthermore, **1_H₂O** (rehyd) and methanol-re-adsorbed sample (**1_re-MeOH**) showed the same magnetic profiles as **1_H₂O and 1_MeOH** (Fig. 22), indicating the reversible magnetic responsivity of **1**.

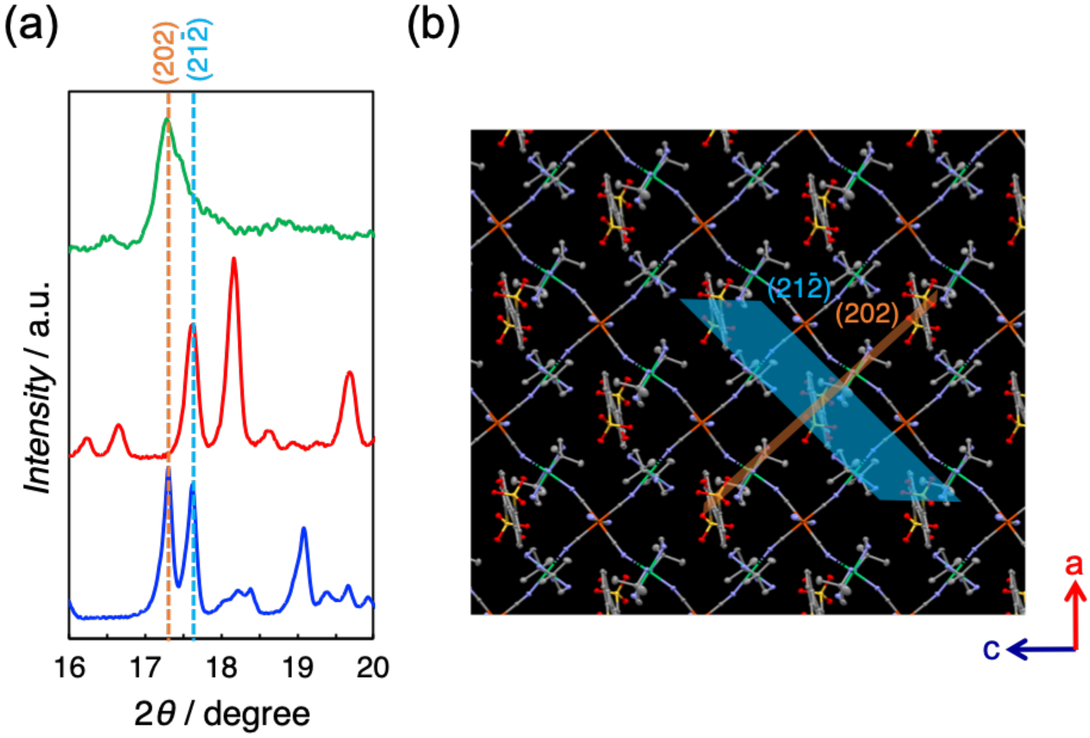

Fig. 21 (a) PXRD patterns of **1_H₂O** (blue), **1** (red) and **1_MeOH** (green). (b) Lattice plane of (202) and (21$\bar{2}$)

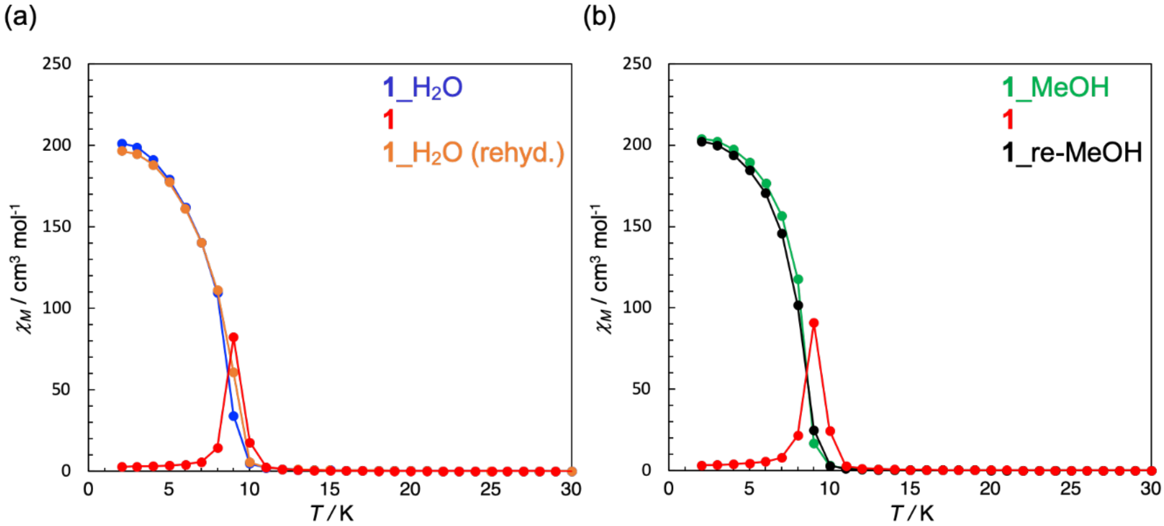

Fig. 22 Temperature dependence of χ_M *vs* T plots for (a) **1_H$_2$O** (blue), **1** (red), **1_H$_2$O** (rehyd.) (orange) and (b) **1_MeOH** (green), **1** (red), **1_re-MeOH** (black) under an applied magnetic field of 10 Oe.

Magnetic profiles for **2** and **2_H$_2$O**, and CO_2-adsorbed states (**2**$\supset CO_2$ (50 kPa) and (**2**$\supset CO_2$ (100 kPa)) were investigated through *in situ* magnetic measurement. Magnetic susceptibilities (χ_M) were measured under a dc magnetic field of 10 Oe. Temperature dependence of field-cooled magnetization (FCM) for **2_H$_2$O** and **2** are shown in Fig. 23. Both **2_H$_2$O** and **2** showed antiferromagnetic transition, in which the χ_M started to increase sharply at approximately 10 K, reaching a maximum of 23.3 cm^{3}mol^{-1} (**2_H$_2$O**, at 9 K) and 16.7 cm^{3}mol^{-1} (**2**, at 11 K), and then decreased to 2.9 cm^{3}mol^{-1} at 2 K upon cooling process. Additionally, *M–H* curves at 2 K demonstrated that the magnetization value of 4.95 $N\beta$ (**2_H$_2$O**) and 5.25 $N\beta$ (**2**) were observed at 5 T, suggesting the ferromagnetic coupling in the cationic 2-D sheet (Fig. 24).

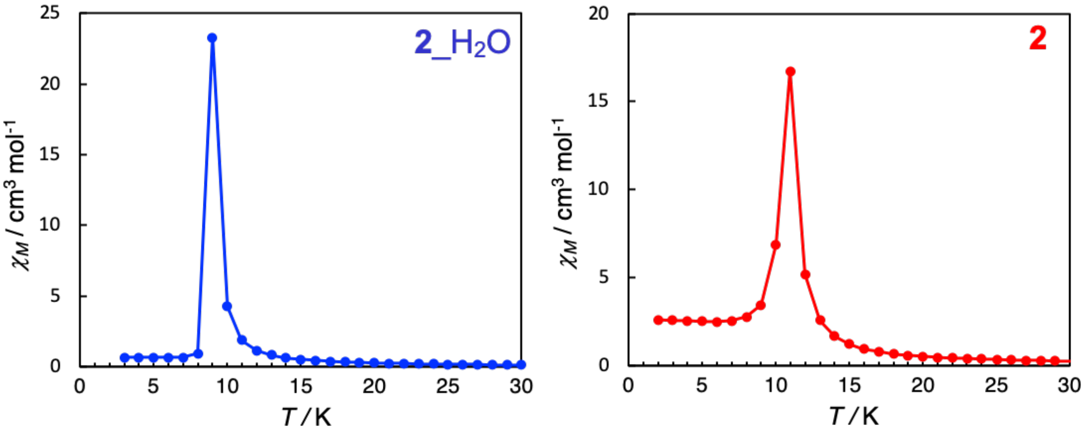

Fig. 23 Temperature dependence of χ_M *vs* *T* plots of **2_H$_2$O** (blue), and **2** (red) under an applied magnetic field of 10 Oe.

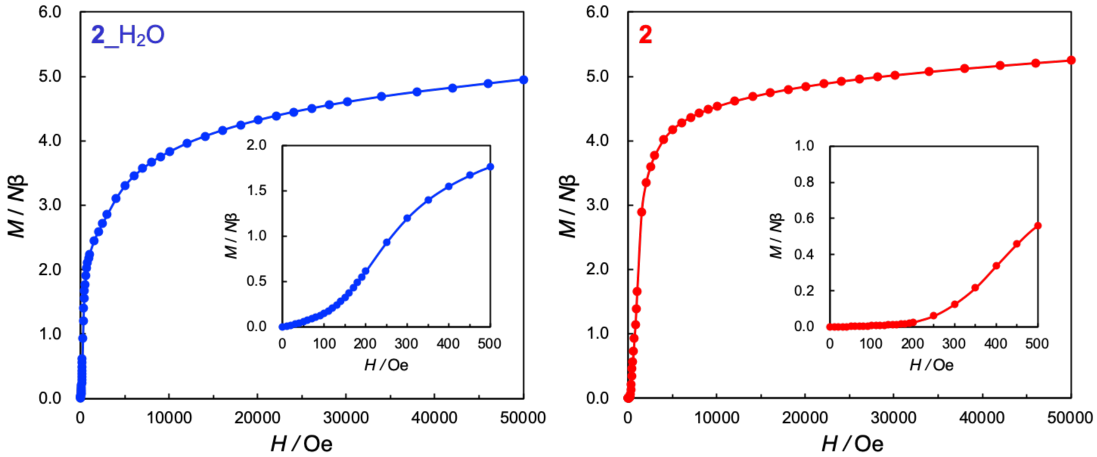

Fig. 24 Field dependence of magnetization curves of **2_H$_2$O** (blue), and **2** (red) at 2 K. Inset: low-magnetic field region.

Magnetic behaviors of the two types of CO_2-adsorbed states were investigated through *in situ* pressure-dependent magnetic measurement under CO_2 at 196 K. *In situ* magnetic measurements were performed using a Quantum Design MPMS-XL5R SQUID connected to an adsorption device (BELSORP-min II-PR). The samples were put into a homemade sample cell, and then fixed to the end of the sample transport rod (Fig. 25).

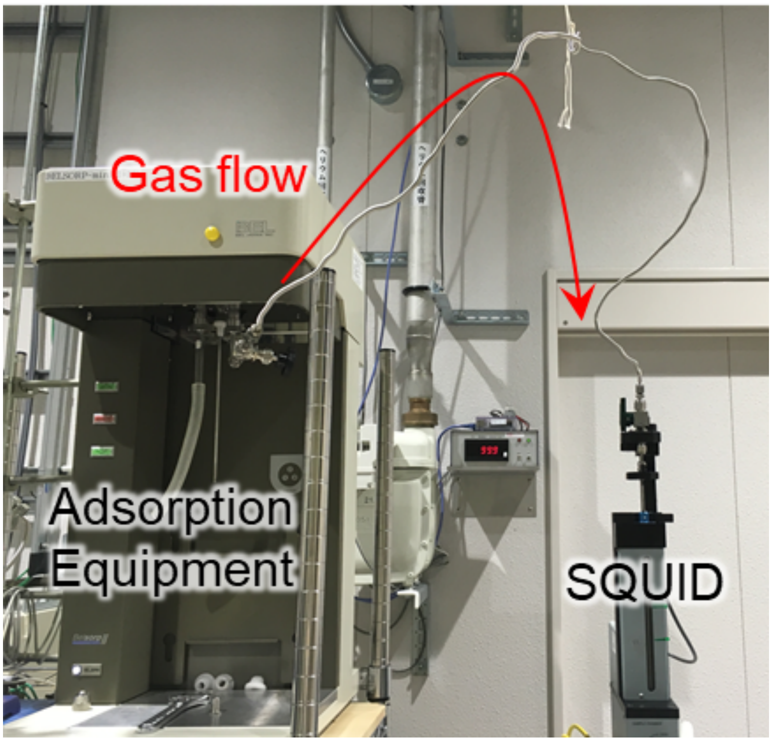

Fig. 25 *In situ* magnetic measurement system

Fig. 26 shows the FCM profiles for **2**, **2**⊃CO_2 (50 kPa) and **2**⊃CO_2 (100 kPa). **1**⊃CO_2 (50 kPa) showed similar magnetic behavior that of **2**, in which the χ_M of **1**⊃CO_2 (50 kPa) started to increase sharply at approximately 10 K, reaching a maximum of 20.15 cm^3mol^{-1} at 11 K, and then decreased to 7.59 cm^3mol^{-1} at 2 K, antiferromagnetic ordering. Moreover, *M*–*H* curve at 2 K of **2**⊃CO_2 (50 kPa) exhibited the magnetization value of 5.29 $N\beta$ at 5 T (Fig. 27). In contrast, **2**⊃CO_2 (100 kPa) displayed an abrupt increase of χ_M value and the maximum value of 164.5 cm^3mol^{-1} at 2 K, suggesting ferromagnetic ordering. Furthermore, temperature dependence of ac magnetic of **2**⊃CO_2 (100 kPa) susceptibilities was measured to confirm the magnetic ordering. Fig. 28 depicts the χ'_M *vs.* *T* Plots for **2**⊃CO_2 (100 kPa) in the frequency range of 1–1000 Hz under a zero dc field and an oscillating field of 3 Oe. The single distinct peak of **2**⊃CO_2 (100 kPa) without notable frequency dependence indicated that the phase transition temperature of **2**⊃CO_2 (100 kPa) was determined to be 11 K and the long-range ordering of **2**⊃CO_2 (100 kPa) might be caused by the partially produced spin-canted domains.

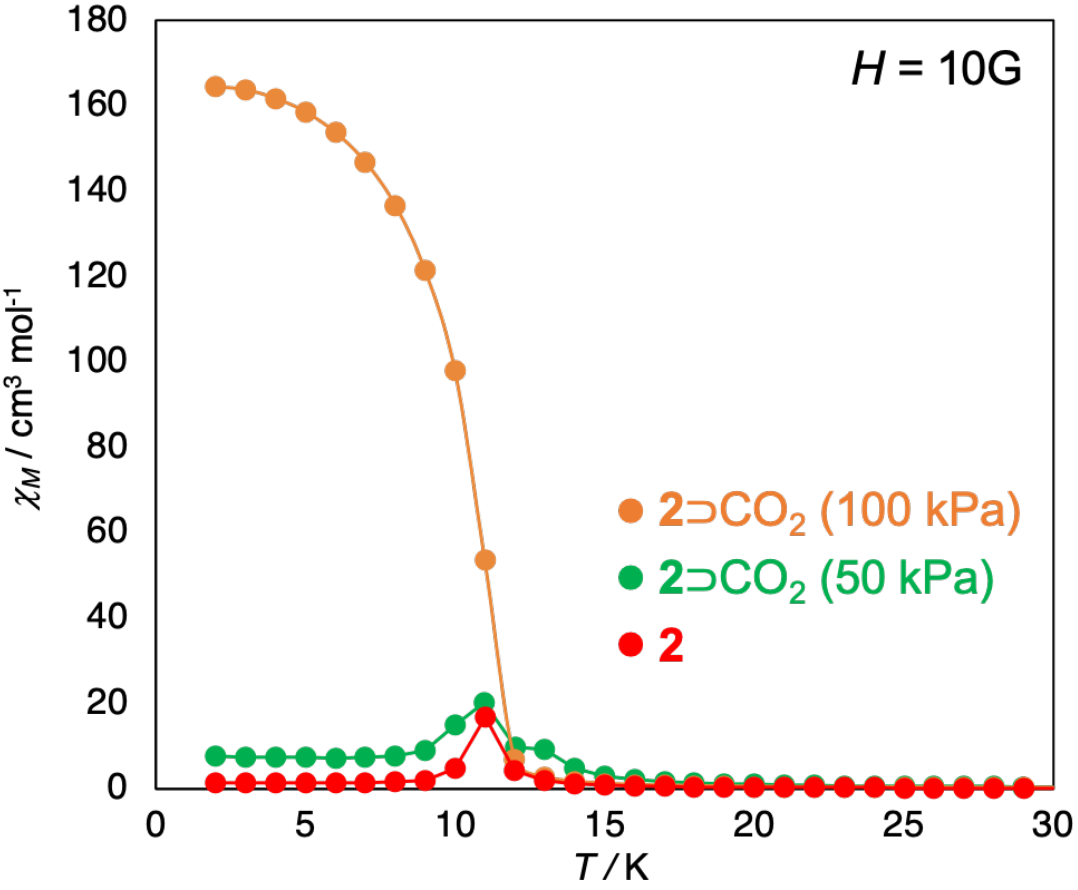

Fig. 26 Temperature dependence of χ_M *vs* *T* plots of **2** (red), **2**⊃CO_2 (50 kPa) (green), and **2**⊃CO_2 (100 kPa) (orange) under an applied magnetic field of 10 Oe.

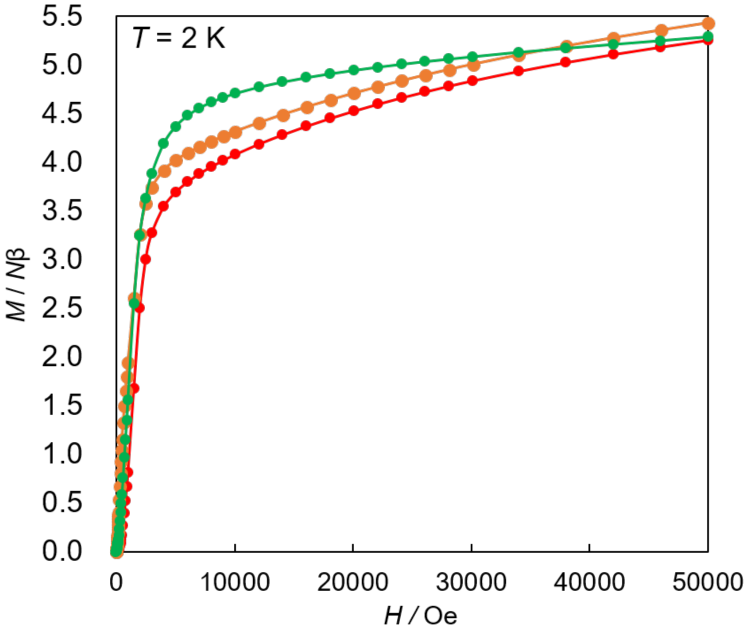

Fig. 27 Field dependence of magnetization curves of **2** (red), **2**$\supset$CO$_2$ (50 kPa) (green), and **2**$\supset$CO$_2$ (100 kPa) (orange) at 2 K.

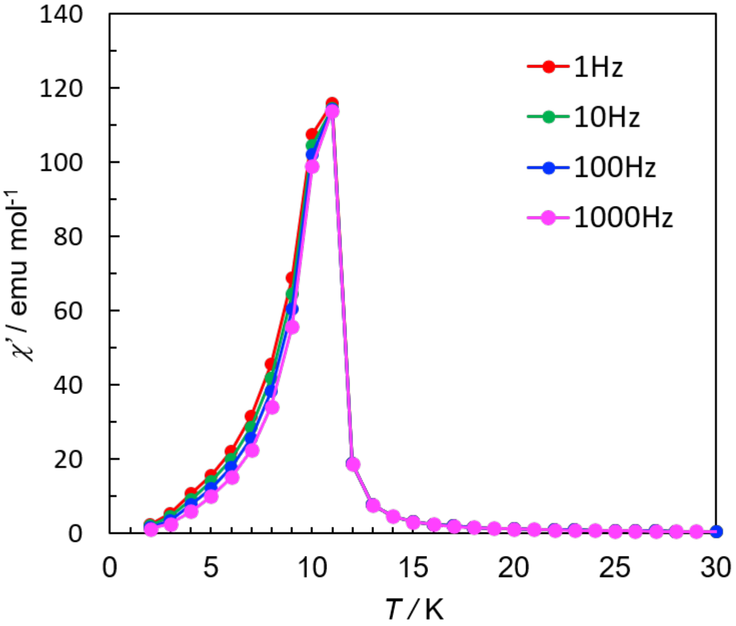

Fig. 28 Temperature dependence of χ'_{M} *vs*. T and χ''_{M} *vs*. T plots for **2**$\supset$CO$_2$ (100 kPa) measured in the frequency range of 1–1000 Hz under a zero dc field and an oscillating field of 3 Oe (temperature range: 2–30 K).

Mechanism of Guest-driven Magnetic Phase Conversion of 1 and 2

The magnetic phase of **1** is governed by intralayer and interlayer interactions.[30] In the $[\{Ni(dmen)_2\}_2\{Fe(CN)_6\}]^+$ sheet, ferromagnetic coupling operates based on the strict orthogonality between the magnetic dπ orbitals of the low-spin Fe(III) ion and the dσ orbitals of the Ni(II) ion (Fig. 29).[30,31] Furthermore, entire magnetic phase depends on through-space interlayer interactions.[62] Magnetic dipolar interactions relate to the distance and angle between the magnetic dipoles. The threshold of interlayer distance is approximately 10 Å in 2-D magnetic systems. [30,31,63,64] In the case of **1**, the *d* value changes from 10.14 Å to 11.08 Å with hydration treatment, resulting in the magnetic phase modulation from antiferro- to ferro-magnet. The correlation between the resultant *d* values and magnetic phase of **1_H$_2$O**, **1**, and **1_MeOH** is good agreement with the reported trends, suggesting that the reversible magnetic phase conversion was driven by a porosity-enabled mechanism.

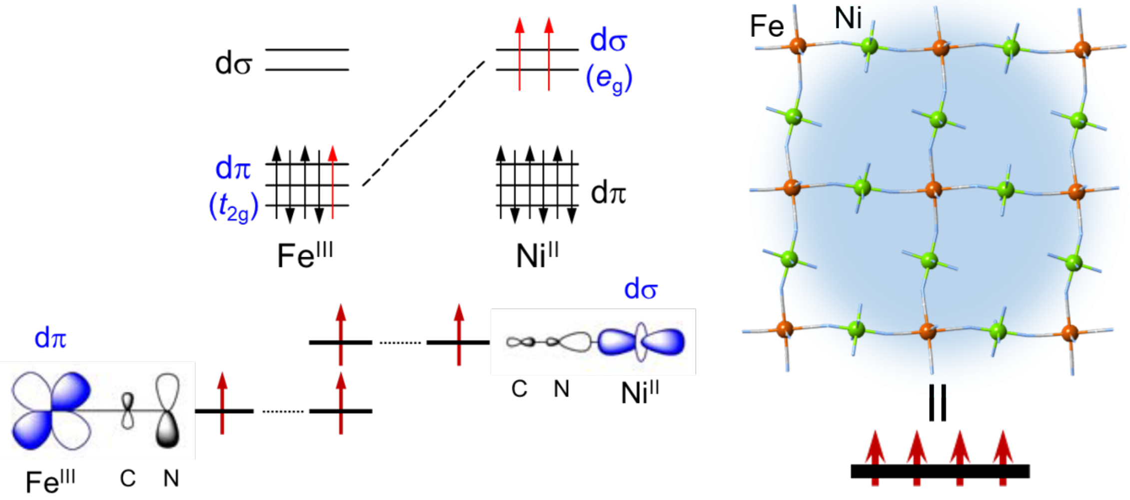

Fig. 29 Schematic illustration of ferromagnetic intralayer interaction based on the strict orthogonality between the magnetic dπ orbitals of the low-spin Fe(III) ion

In the case of **2**⊃CO_2 (50 kPa), the *d* value changes from 9.71 Å to 10.01 Å, and, the magnetic phase was not changed upon 1st CO_2 adsorption. In contrast, the *d* value of **2**⊃CO_2 (100 kPa) changes from 10.01 Å to 11.26 Å, in which the magnetic phase changes from antiferro- to ferro-magnetic ordering with 2nd CO_2 adsorption along with gate-opening behavior. The correlation between the resultant *d* values and magnetic phase of **2**, **2**⊃CO_2 (50 kPa) and **2**⊃CO_2 (100 kPa) is in good agreement with the reported trends, suggesting that the magnetic phase switching was achieved via a porosity-enabled mechanism. Thus, the resultant CO_2 -induced magnetic phase conversion plausibly related to the adsorption sites in the framework (Fig. 30). In the 1st CO_2 adsorption, **2**⊃CO_2 (50 kPa)) exhibited metamagnetic behavior similar to the activated **2** because CO_2 molecules were adsorbed in the double-layers involving the AZDC^{2-} as a pseudo pillar ligand. On the other hand, **2**⊃CO_2 (100 kPa) showed ferromagnetic behavior which was completely different from another two states, indicating that antiferromagnetic interlayer interaction was canceled due to the expanding of interlayer distance along with the gate-adsorption. Hence, CO_2 molecules were adsorbed in the interlayers in the 2nd CO_2 adsorption. Furthermore, the suggested mechanism based on the magnetic phase switching of **2** is supported by the results of CO_2 adsorption profiles and magnetic behaviors. Thus, the CO_2 molecules adsorbed in the interlayers is the origin of the manipulation of the magnetic phase in **1**.

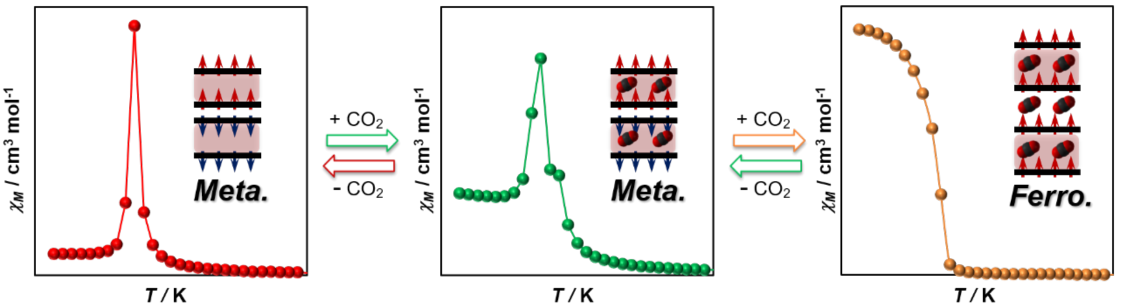

Fig. 30 Schematic illustration of the proposed mechanism CO_2 -induced magnetic phase conversion of **2**.

Conclusion

In summary, Novel porous magnets, $[Ni^{II}(dmen)_2]_2[Fe^{III}(CN)_6](A)_{0.5}\cdot 7H_2O$ (dmen = 1,1-dimethylethylenediamine, A^{2-} = 1,5-anthraquinonedisulfonate ($AQDS^{2-}$; **1_H_2O**) or = Azobenzene-4,4’-dicarboxylate ($AZDC^{2-}$; **2_H_2O**)), showing guest-driven magnetic phase conversion were rationally synthesized. These compounds possessed different packing structures depending on the pillar dianions. **1_H_2O** formed a pseudo 3-D pillared-layer type structure, in which the dianions were located at each interlayer space uniformly. On the other hand, **2_H_2O** derived a double-layer type structure having different interlayer structure. Significant structural changes with guest uptake and release were confirmed by *in situ* powder X-ray diffraction measurements in both compounds. Furthermore, *in situ* magnetic measurements under guest atmosphere revealed that the magnetic phase of these porous magnets changed depending on the guest molecules. Dehydrated samples of **1** and **2** exhibited gate-adsorption behavior owing to their flexible structure, in which the magnetic phase of the framework converted from antiferromagnetic and ferromagnetic phases because the antiferromagnetic interlayer interaction was canceled due to the expanding of interlayer distance. The number of studies on functional MOFs has increased rapidly because of their potential for application. However, establish of promising guideline for material design to gas molecules remains challenging. From this perspective, this work finally highlights that dianion-based flexible porous magnet can provide new insights into the rational design of gas-responsive functional materials.

References

1. G. J. Halder, C. J. Kepert, B. Moubaraki, K. S. Murray and J. D. Cashion, *Science*, 2002, **298**, 1762–1765.
2. B. Zhang, Z.-M. Wang, M. Kurmoo, S. Gao, K. Inoue and H. Kobayashi, *Adv. Funct. Mater.*, 2007, **17**, 577–584.
3. M. Kurmoo, *Chem. Soc. Rev.*, 2009, **38**, 1353–1379.
4. P. Dechambenoit, J. R. Long, *Chem. Soc. Rev.*, 2011, **40**, 3249–3265.
5. G. M. Espallargas and E. Coronado, *Chem. Soc. Rev.*, 2018, **47**, 533–557.
6. S. Kitagawa, R. Kitaura and S. Noro, *Angew. Chem. Int. Ed.*, 2004, **43**, 2334–2375.
7. O. M. Yaghi, M. O'Keeffe, N. W. Ockwig, H. K. Chae, M. Eddaoudi and J. Kim, *Nature*, 2003, **423**, 705–714.
8. N. Yanai, K. Kitayama, Y. Hijikata, H. Sato, R. Matsuda, Y. Kubota, M. Takata, M. Mizuno, T. Uemura and S. Kitagawa, *Nat. Mater.*, 2011, **10**, 787–793.
9. M. Wang, L. Guo and D. Cao, *Anal. Chem.*, 2018, **90**, 3608–3614.
10. M.Ohba, K. Yoneda, S. Kitagawa, *Cryst. Eng. Comm.*, 2010, **2**, 159-165.
11. S. Ohkoshi, K. Arai, Y. Sato and K. Hashimoto, *Nat. Mater.*, 2004, **3**, 857–861.
12. E. Coronado, M. Giménez-Marqués, G. Mínguez Espallargas, F. Rey and I. J. Vitórica-Yrezábal, *J. Am. Chem. Soc.*, 2013, **135**, 15986–15989.
13. M. Ohba, K. Yoneda, G. Agustí, M. C. Muñoz, A. B. Gaspar, J. A. Real, M. Yamasaki, H. Ando, Y. Nakao, S. Sakaki and S. Kitagawa, *Angew. Chem. Int. Ed.*, 2009, **48**, 4767–4771.
14. R. Turo-Cortés, C. Bartual-Murgui, J. Castells-Gil, M. C. Muñoz, C. Martí-Gastaldo and J. A. Real, *Chem. Sci.*, 2020, **11**, 11224–11234.
15. D. Maspoch, D. Ruiz-Molina and J. Veciana, *Chem. Soc. Rev.*, 2007, **36**, 770.
16. M. Atzori, S. Benmansour, G. Mínguez Espallargas, M. Clemente-León, A. Abhervé, P. Gómez-Claramunt, E. Coronado, F. Artizzu, E. Sessini, P. Deplano, A. Serpe, M. L. Mercuri and C. J. Gómez García, *Inorg. Chem.*, 2013, **52**, 10031–10040.
17. C. Martínez-Hernández, P. Gómez-Claramunt, S. Benmansour and C. J. Gómez-García, *Dalton Trans.*, 2019, **48**, 13212–13223.
18. W. Kaneko, M. Ohba and S. Kitagawa, *J. Am. Chem. Soc.*, 2007, **129**, 13706–13712.
19. Y. Yoshida, K. Inoue, K. Kikuchi and M. Kurmoo, *Chem. Mater.*, 2016, **28**, 7029–7038.
20. M. Kurmoo, H. Kumagai, K. W. Chapman and C. J. Kepert, *Chem. Commun.*, 2005, 3012–3014.

21. J. A. Rodríguez-Velamazán, M. A. González, J. A. Real, M. Castro, M. C. Muñoz, A. B. Gaspar, R. Ohtani, M. Ohba, K. Yoneda, Y. Hijikata, N. Yanai, M. Mizuno, H. Ando and S. Kitagawa, *J. Am. Chem. Soc.*, 2012, **134**, 5083–5089.
22. N. Motokawa S. Matsunaga, S. Takaishi, H. Miyasaka, M. Yamashita, K. R. Dunbar, *J. Am. Chem. Soc.,* 2010, **132**, 11943-11951.
23. N. Yanai, W. Kaneko, K. Yoneda, M. Ohba and S. Kitagawa, *J. Am. Chem. Soc.*, 2007, **129**, 3496–3497.
24. H. Yoshino, K. Yamagami, H. Wadati, H. Yamagishi, H. Setoyama, S. Shimoda, A. Mishima, B. L. Ouay, R. Ohtani, M. Ohba, *Inorg. Chem*., 2021, **60**, 3338–3344.
25. J. Zhang, W. Kosaka, K. Sugimoto and H. Miyasaka, *J. Am. Chem. Soc.*, 2018, **140**, 5644–5652.
26. H. Miyasaka, *Acc. Chem. Res.*, 2013, **46**, 248–257.
27. J. Zhang W. Kosaka, Y. Kitagawa, H. Miyasaka, *Angew. Chem. Int. Ed.,* 2019, **58**, 7351-7356.
28. J. Zhang W. Kosaka, Y. Kitagawa, H. Miyasaka, *Nat. Chem*., 2021, **13**, 191-199.
29. W. Kosaka, Z. Liu, J. Zhang, Y. Sato, A. Hori, R. Matsuda, S. Kitagawa and H. Miyasaka, *Nat. Commun.*, 2018, **9**, 5420.
30. M. Ohba and H. Zhou, *Coord. Chem. Rev.*, 2000, **198**, 313–328.
31. H. Yoshino, N. Tomokage, A. Mishima, B. Le Ouay, R. Ohtani, W. Kosaka, H. Miyasaka, M. Ohba, *Chem. Commun.,* 2021 **57***,* 5211-5214.
32. M. E. Boot-Handford, J. C. Abanades, E. J. Anthony, M. J. Blunt, S. Brandani, N. M. Dowell, J. R. Fernández, M. C. Ferrari, R. Gross, J. P. Hallett, R. S. Haszeldine, P. Heptonstall, A. Lyngfelt, Z. Makuch, E. Mangano, R. T. J. Porter, M. Pourkashanian, G. T. Rochelle, N. Shah, J. G. Yaoa, Paul S. Fennell, *Energy Environ.*, 2014, **7**, 130-189.
33. S. Chu, *Science*, 2009, **325**, 1599.
34. P.-Z. Li and Y. Zhao, *Chem. Asian J.*, 2013, **8**, 1680-1691.
35. R. Vaidhyanathan, S. S. Iremonger, K. W. Dawson, and G. K. H. Shimizu, *Chem. Commun.*, 2009, 5230-5232.
36. A. Demessence, D. M. D'Alessandro, M. L. Foo, and J. R. Long, J. *Am. Chem. Soc.*, 2009, **131**, 8784-8786.
37. K. D. Vogiatzis, A. Mavrandonakis, W. Klopper, G. E. Froudakis, *Chem. Phys. Chem.*, 2009, **10**, 374-383.
38. Y.-S. Bae, and R. Q. Snurr, *Angew. Chem.*, 2011, **123**, 11790-11801.
39. Y.-S. Bae, and R. Q. Snurr, *Angew. Chem. Int. Ed.*, 2011, **50**, 11586-11596.
40. J.-R. Li, Y. Ma, M. C. McCarthy, J. Sculley, J. Yu, H.-K. Jeong, P. B. Balbuen, and H.-C. Zhou, *Coord. Chem. Rev.*, 2011, **255**, 1791-1823.

41. K. Sumida, D. L. Rogow, J. A. Mason, T. M. McDonald, E. D. Bloch, Z. R. Herm, T.-H. Bae, and J. R. Long, *Chem. Rev.*, 2012, **112**, 724-781.
42. J. Liu, P. K. Thallapally, B. P. McGrail, D. R. Brown, and J. Liu, *Chem. Soc. Rev.*, 2012, **41**, 2308-2322.
43. B. Wang, A. P. Côté, H. Furukawa, M. O'Keeffe, and O. M. Yaghi, *Nature*, 2008, **453**, 303–308.
44. R. Banerjee, H. Furukawa, D. Britt, C. Knobler, M. O'Keeffe, and O. M. Yaghi, *J. Am. Chem. Soc.*, 2009, **131**, 3875-3877.
45. R. Vaidhyanathan, S. S. Iremonger, G. K. H. Shimizu, P. G. Boyd, S. Alavi, and T. K. Woo, *Science*, 2010, **330**, 650-653.
46. R. Vaidhyanathan, S. S. Iremonger, G. K. H. Shimizu, P. G. Boyd, S. Alavi, and T. K. Woo, *Angew. Chem.*, 2012, **124**, 1862-1865.
47. R. Vaidhyanathan, S. S. Iremonger, G. K. H. Shimizu, P. G. Boyd, S. Alavi, and T. K. Woo, *Angew. Chem. Int. Ed.*, 2012, **51**, 1826-1829.
48. X.-J. Wang, P.-Z. Li, L. Liu, Q. Zhang, P. Borah, J. D. Wong, X. X. Chan, G. Rakesh, Y. Li, and Y. Zhao, *Chem. Commun.*, 2012, **48**, 10286-10288.
49. X.-J. Wang, P.-Z. Li, Y. Chen, Q. Zhang, H. Zhang, X. X. Chan, R. Ganguly, Y. Li, J. Jiang, and Y. Zhao, *Sci. Rep.*, 2013, **3**, 1149.
50. T. M. McDonald, D. M. D'Alessandro, R. Krishna, and J. R. Long, *Chem. Sci.*, 2011, **2**, 2022-2028.
51. T. M. McDonald, W. R. Lee, J. A. Mason, B. M. Wiers, C. S. Hong, and J. R. Long, *J. Am. Chem. Soc.*, 2012, **134**, 7056-7065.
52. S. Choi, T. Watanabe, T.-H. Bae, D. S. Sholl, and C.W. Jones, *J. Phys. Chem. Lett.*, 2012, **3**, 1136-1141.
53. Boudreaux, E. A. & Mulay, L. N. *Theory and Applications of Molecular Paramagnetism.* (John Wiley & Sons, New York, 1976).
54. O. V. Dolomanov, L. J. Bourhis, R. J. Gildea, J. a. K. Howard and H. Puschmann, *J. Appl. Crystallogr.*, 2009, **42**, 339–341.
55. A. L. Spek, *J. Appl. Crystallogr.*, 2003, **36**, 7–13.
56. V. Favre-Nicolin and R. Černý, *J. Appl. Crystallogr.*, 2002, **35**, 734–743.
57. F. Izumi and K. Momma, *Solid State Phenom.,* 2007, 130, 15–20.
58. J.-R. Li, R. J. Kuppler and H.-C. Zhou, *Chem. Soc. Rev.*, 2009, **38**, 1477–1504.
59. W. H. Bragg and W. L. Bragg, *Proc. R. Soc. Lond. Ser. Contain. Pap. Math. Phys. Character*, 1913, **88**, 428–438.
60. M. Ohba, H. Ōkawa, N. Fukita and Y. Hashimoto, *J. Am. Chem. Soc.*, 1997, **119**, 1011–1019.
61. G. Rogez, C. Massobrio, P. Rabu and M. Drillon, *Chem. Soc. Rev.*, 2011, **40**, 1031.

62. R. Bourzami, S. Eyele-Mezui, E. Delahaye, M. Drillon, P. Rabu, N. Parizel, S. Choua, P. Turek and G. Rogez, *Inorg. Chem.*, 2014, **53**, 1184–1194.
63. W. Kosaka, Z. Liu and H. Miyasaka, *Dalton Trans.*, 2018, **47**, 11760–11768.
64. W. Kosaka, M. Itoh and H. Miyasaka, *Mater. Chem. Front.*, 2018, **2**, 497–504

Chapter 3

Multiple Spin State Change and Non-equilibrium State in Gaseous Alkane Clathrates

Abstract

A 3D Hofmann-type PCP {Fe(pz)[Pt(CN)$_4$]} (**1**; pz = pyrazine) consisting of pillared 2-D cyanide-bridged Fe(II)Pt(II) layers shows a cooperative spin transition (ST) behavior around room temperature and a reversible chemo-switching of spin state of Fe(II) coupling with guest adsorption. Magnetic behavior of **1** strongly depends on the guest molecules. However gaseous molecules such as O_2, N_2 and CO_2 hardly affect the magnetic behaviors because of their weak interaction with the framework. Here, we selected alkane derivatives as guest molecules which are expected to interact with pz in the framework of **1** through CH–π contacts. In addition, magnetic and structural properties of **1** with liquid alkanes adsorption were also investigated to evaluate systematic responsivity for alkanes. **1**⊃Liquid alkanes were obtained by vapor diffusion, and the clathrates showed expansion of the framework relating with alkanes adsorption. The magnetic behavior of **1**⊃Liquid alkanes exhibited hysteretic two-steps ST, and the phase transition temperature decreased as the size of alkanes increased. These results indicate that the behavior of alkanes confined in the pore affect the magnetic properties of the framework. The responsivity of gaseous alkanes was discussed based on various *in situ* measurement systems. *In situ* magnetic measurement under gaseous alkane revealed that the high-spin state of **1** was smoothly stabilized by uptaking alkanes at 298 K, which was also confirmed by *in situ* PXRD measurements. Magnetic behavior of **1**⊃Gaseous alkanes showed multi-step spin crossover which was completely different from that of guest-free **1**. In particular, **1**⊃C_3H_8 showed an extremely unique phenomenon that the $\chi_M T$ value decreases in the heating process. Correlation among alkane chain length, structure and magnetic behavior were discussed based on temperature dependence of *in situ* powder X-ray diffraction measurement.

Introduction

Research of porous coordination polymers (PCPs) or metal-organic frameworks (MOFs) achieved remarkable developments in this century.[1-4] PCPs are a new class of porous materials which consist of metal ions or clusters and organic ligands which are connected into frameworks based on coordination bonds with the aid of other interactions, such as hydrogen/metal-metal bonds, π-π, CH-π, electrostatic, and van der Waals interactions, enabling the formation flexible structures.[5-9] PCPs are utilized for a wide range of application because of the following characteristics, (i) the simple synthetic method by self-assembly of metal ions as connector and ligands as pillars, (ii) the rich chemical diversity in the basis of combination of structural components (metal ions, ligands and co-ligands), (iii) the high designability, regularity and flexibility of their frameworks based on coordination bonds, and (iv) the tunable various physical properties of the frameworks. In particular, the feature (iii) is not exhibited by other porous materials such as zeolites and activated porous carbons. Excellent regularity and tunable porous property of PCPs lead to attractive for various applications such as gas storage, separation, catalysis, and sensor.[9-14] PCPs are also expected to be a platform interlocking porosity-related functions and physical properties such as electrical conductivity,[15-17] nonlinear optics,[18-20] proton conductivity,[21-23] and magnetism.[24-26] The flexible framework of PCP shows reversible structural changes relating with guest adsorption/desorption due to host-guest interactions. Especially, magnetic interactions are susceptible to changes of the overlap integral between metal ion and ligand orbitals and are therefore suitable for evaluating guest-responsivity. In this work, we have investigated the porous and magnetic properties of PCPs in order to combine porosity-related functions and physical properties. Spin crossover (SCO) phenomenon, in which external stimuli (such as pressure, temperature, magnetic field, or light) drive an electronic conversion between two local spin states represents one of the most attractive classes of molecule-based switches.[27-34]

Herein, we prepared a 3D Hofmann-type porous PCP $\{Fe^{II}(pz)[Pt(CN)_4]\}$ (**1**; pz = pyrazine) shows a cooperative spin transition (ST) around room temperature and a reversible chemo-switching of spin state of Fe(II) coupling with guest adsorption. In the magnetic behavior of **1**, ST temperature (T_c), cooperativity of ST, and hysteresis width strongly depend on the guest molecules. However gaseous molecules such as O_2, N_2 and CO_2 hardly affect the magnetic behaviors because of their weak interaction with the framework. Here we focus on alkane derivatives as guest molecules which are expected to interact with pz in the framework of **1** through CH–π contacts. Furthermore, magnrtic and structural properties of **1** with liquid alkanes (C_nH_{2n+2}; $n = 6 - 8$) adsorption were also investigated to evaluate systematic responsivity.

Experimental Section

Materials

All chemicals were purchased from commercial sources and used without further purification.

{Fe(pz)[Pt(CN)$_4$]} (1)

This compound was prepared according to the literature method. $Fe^{II}(NH_4)_2(SO_4)_2\cdot 6H_2O$ (0.256 g, 0.653 mmol) and pyrazine (0.105 g, 1.31 mmol) were dissolved in degassed water (45 ml), and then a degassed methanolic solution (45 ml) of $K_2[Pt(CN)_4]\cdot 3H_2O$ (0.255 g, 0.675 mmol) and antioxidant ascorbic acid (0.115 g) was added to the solution under nitrogen at room temperature. After stirring for 3 days, the yellow precipitation was collected by suction filtration, washed with water and methanol and dried under ambient pressure. After heating at 403K for 6 hours, guest-free solid was prepared. The compound was confirmed to be {Fe(pz)[Pt(CN)$_4$]} (**1**) by PXRD, TGA, elemental analysis, FT-IR and magnetic measurement. Yield: 183 mg (79.3 %). Elemental analysis (%) calcd for {Fe(pz)[Pt(CN)$_4$]} ($C_8H_6N_6OFePt$): C 22.08, ; H 0.93 ; N 19.32; found: C 21.92; H 0.94; N 19.02; X-ray fluorescence analysis (%) found: Fe / Pt = 1.2

Physical Measurements

Elemental analysis of carbon, hydrogen and nitrogen for [{Fe^{II}(pz)[Pt(CN)$_4$]} (**1**; pz = pyrazine) was carried out at the division of graduate school of science in Kyushu University. Thermal gravimetric analysis (TGA) was performed using a Perkin Elmer STA6000 instrument, in the temperature range of 300–900 K, under N_2 atmosphere (heating rate: 5 K min^{-1}). PXRD patterns at room temperature were collected on a Rigaku Ultima IV spectrometer using a reflection-free sample holder (λ = 1.5418 Å). *In situ* variable-pressure powder X-ray structural analysis (VP-PXRD) were carried out using a Rigaku Smart Lab with Cu−Kα radiation (λ = 1.54178 Å) connected to BELSORP-18PLUS volumetric adsorption equipment. Adsorption and desorption isotherms were acquired using a BELSORP-MAX volumetric adsorption equipment (Microtrac BEL Corp.). The samples were dehydrated by heating at 400 K for 12 h before the measurements. *In situ* magnetic measurements were carried out using a Quantum Design MPMS-XL5R SQUID connected to an adsorption device (BELSORP-min II-PR) in the temperature range, 100 to 320 K in an applied DC magnetic field of 1000 Oe. The samples were put into a homemade sample cell, and then fixed to the end of the sample transport rod. The molar magnetic susceptibility ($\chi_M = M/H$) were corrected for the diamagnetism of the constituent atoms and the sample tube.

Responsivity of liquid-alkene for 1

The adsorption and desorption isotherms of alkanes for **1** were performed using activated sample by heating at 403 K and vacuuming for 6 hours. Compound **1** exhibited typical type I adsorption isotherms according to the IUPAC classification without hysteresis towards alkanes at 298 K. (Fig. 1). The maximum adsorption amount of C_6H_{14}, C_7H_{16} and C_8H_{16} was 0.729, 0.658 and 0.543 per unit at $P/P_0 = 1.0$, respectively. This shows the adsorbed amounts of alkanes depend on the alkyl chain length, which were attributable to the pore size (7.259×7.457×7.457 Å^3).

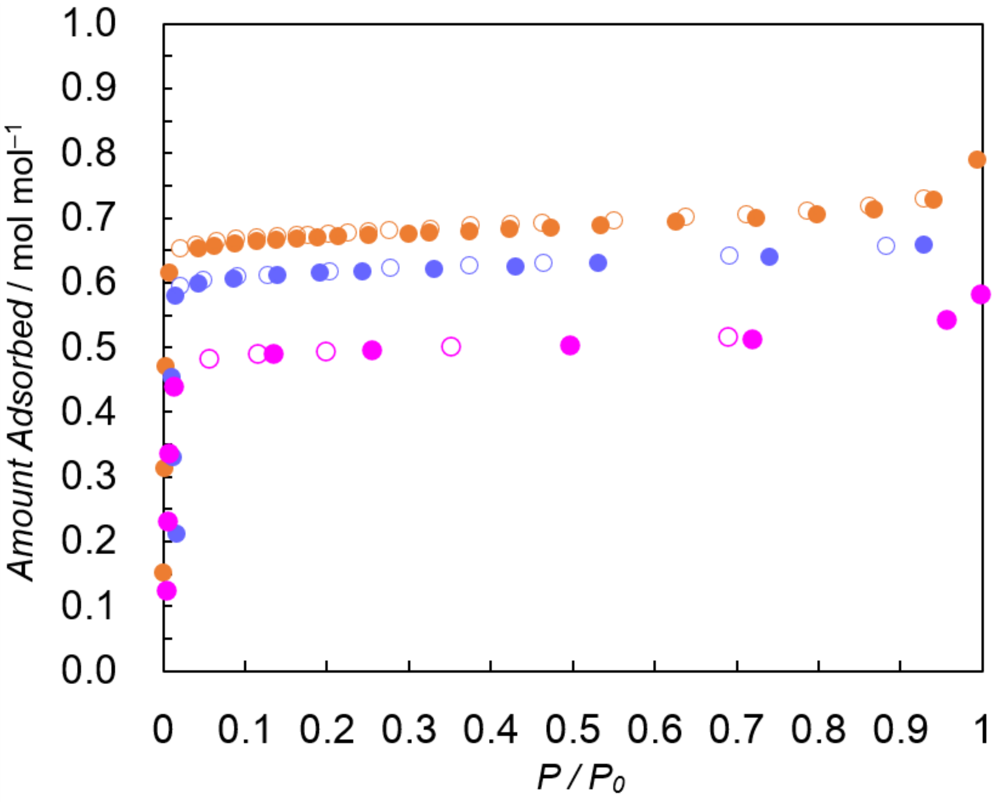

Fig. 1 Adsorption/desorption isotherms of **1** for C_6H_{14} (orange), C_7H_{16} (blue) and C_8H_{18} (pink) at 298 K. The filled and open circles display the adsorption and desorption processes, respectively.

IR spectra of **1**-GF (Guest Free) and **1**⊃Liquid alkanes was recorded using a JASCO FT/IR-4200 spectrophotometer in the range of 650–4000 cm^{-1} at room temperature (Fig. 2(a)). Before the measurement, **1** was activated at 403 K for 6 hours.**1**⊃Liquid alkanes were obtained by vapor diffusion. All compounds showed major bands assigned to the CN stretching around 2160 cm^{-1} and internal vibrations of pz between 1420, 1050 and 800 cm^{-1}. Focusing on the ν_{CN} (2160 cm^{-1}) and ν_{ring} of pz (1050 cm^{-1}), the infrared spectra of **1**⊃Liquid alkanes shifted to lower wavenumbers compared with **1** (Fig. 2(b), (c)). This indicates the expansion of the framework corresponding to alkane adsorption.

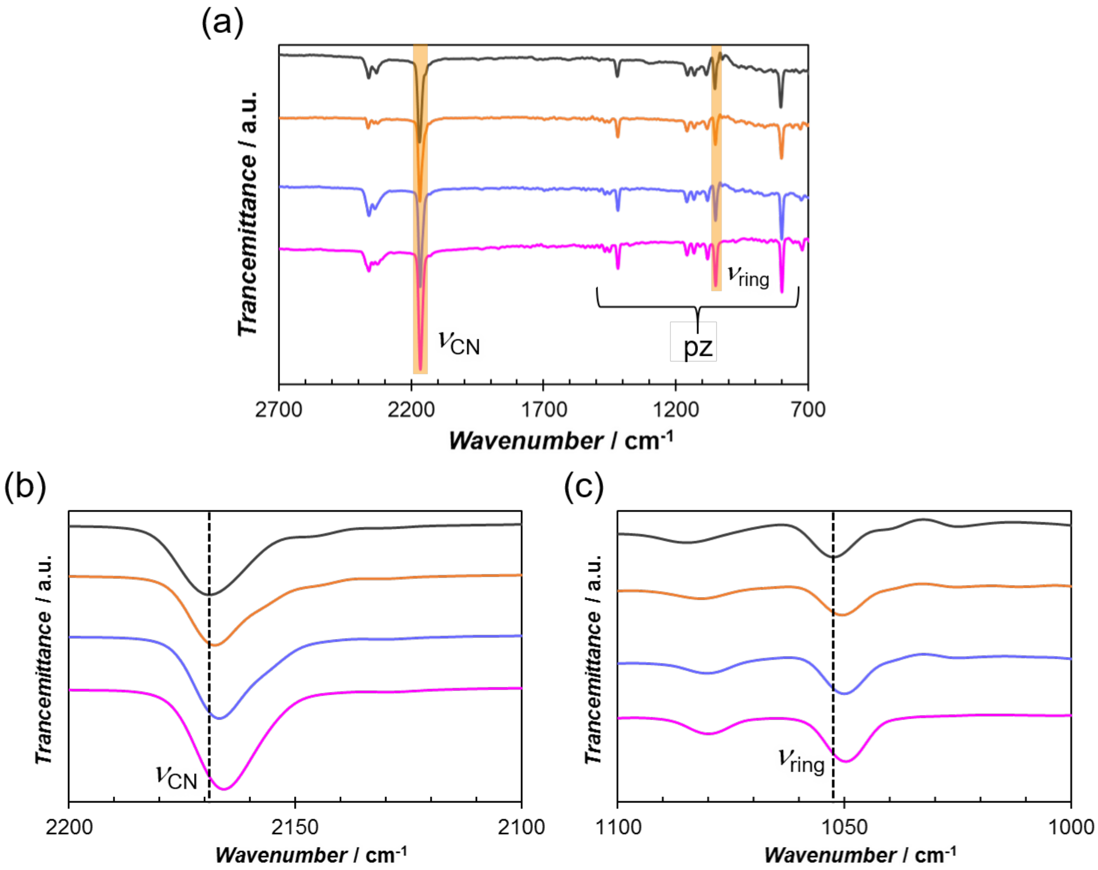

Fig. 2. IR spectra of **1**-GF (gray), **1**⊃C_6H_{14} (orange), **1**⊃C_7H_{16} (blue) and **1**⊃C_8H_{18} (pink) in the range of (a) 2700-700 cm^{-1}, (b) 2200-2100 cm^{-1},(ν_{CN}) and (c) 1100-1000 cm^{-1},(ν_{ring}).

PXRD patterns were collected on a Rigaku Ultima IV at room temperature. $\{Fe(pz)[Pt(CN)_4]\cdot 2H_2O\}$ (**1**) crystalized in the tetragonal space group *P4/mmm* in the LS and HS states. The lattice parameters in the HS and LS states were a = b = 7.457(4), c = 7.259(4) Å and V = 403.6(4) Å^3, and a = b = 7.184(6), c = 6.783(5) Å and V = 350.1(5) Å^3, respectively. Fig. 3 shows the PXRD patterns of **1**-GF and **1**⊃Liquid alkanes. Comparing the PXRD patterns of **1**-GF and **1**⊃Liquid alkanes, all samples showed similar pattern which confirmed that these compounds formed nearly the same structure. Focusing on the peak at 12.2 ° corresponding to (001) plane and at 23.8° corresponding to (200) plane, systematically peak shift to lower degree was observed. This shows the degree of peak shift depends on the size of alkanes and the framework was expanded to the direction of a- and c-axis (Fig. 4).

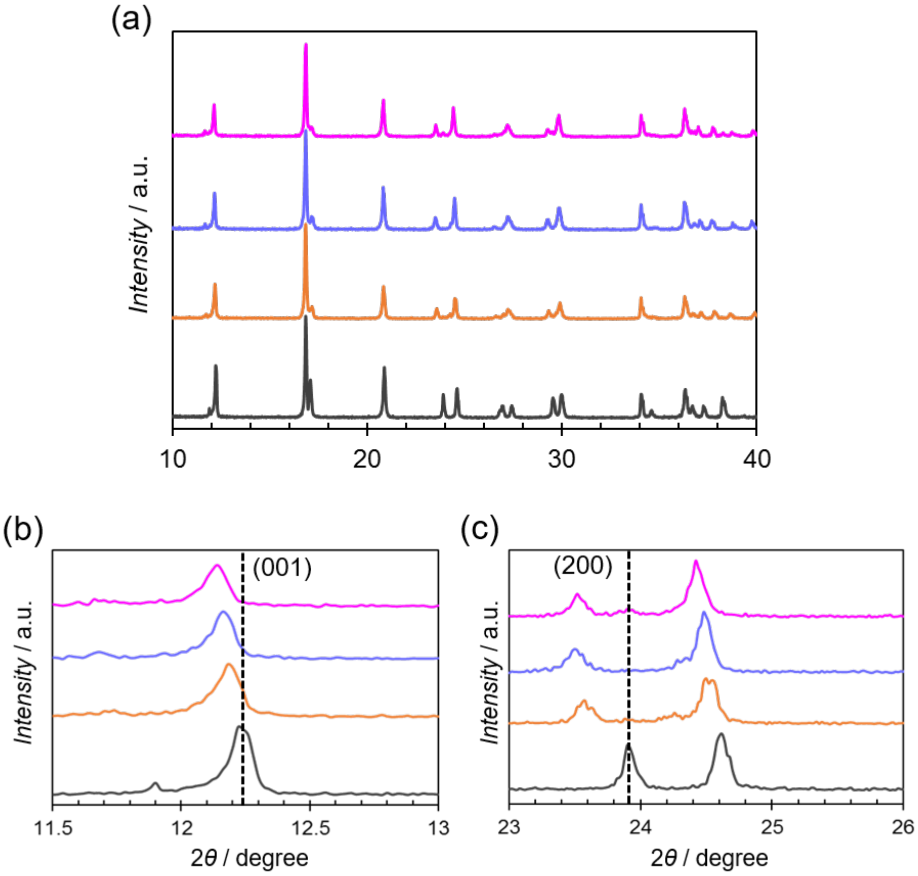

Fig. 3. PXRD patterns of **1**-GF (gray), **1**⊃C_6H_{14} (orange), **1**⊃C_7H_{16} (blue) and **1**⊃C_8H_{18} (pink) in the range of (a) 10 – 40°, 11.5 – 13.0° and (c) 23.0 – 26.0°.

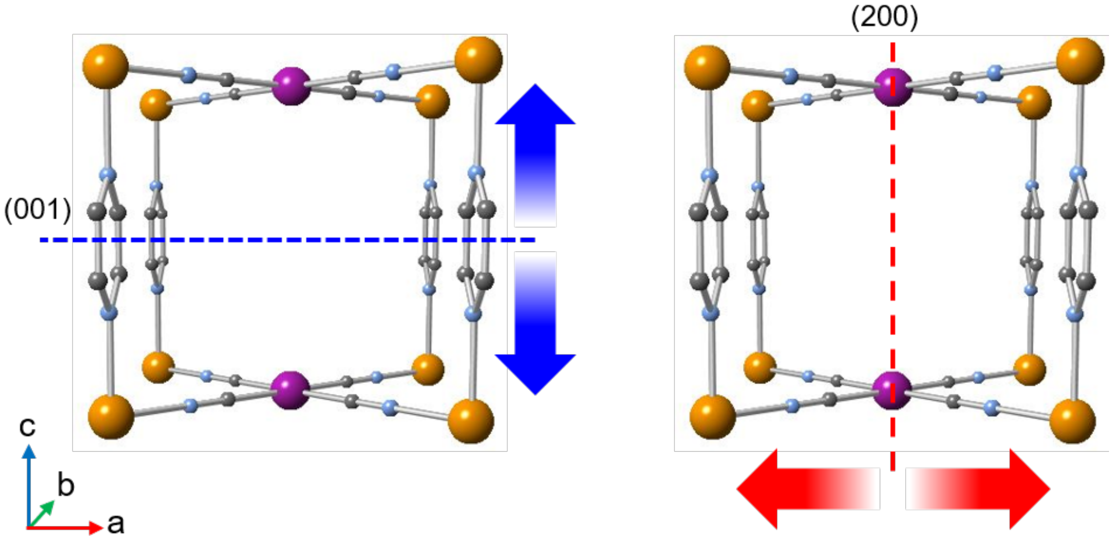

Fig. 4. Detail view of the peak corresponding to (001) plane (left) and (200) plane (right).

The magnetic behavior of 1-GF and 1 ⊃ Liquid alkanes are shown in Fig.5 in the form of $\chi_M T$ vs. T plots. Because the magnetic properties of 1 such as spin transition (ST) temperature (T_c) and hysteresis width strongly depends on the guest molecules, the magnetic measurements were carried out after activation of the samples by heating at 400 K over 6 hours.

1-GF (Guest Free)

The temperature dependence of the magnetic susceptibility of **1**-GF was recorded in the range 180–320 K (scan rate: 2 K min^{-1}) in an applied DC field of 1000 Oe (Fig. 5). The $\chi_M T$ value at 320 K is 3.52 emu K mol^{-1}, which fall into the range expected for an Fe^{II} ion in the HS state. In the cooling process, the $\chi_M T$ value remained practically constant from 320 K to the vicinity of the T_c, then showed a sharp ST to the LS state with abrupt decrease to $\chi_M T$ value within 283 K. The $\chi_M T$ values below 260 K were consistent with that for the LS state of Fe^{II} compounds, which indicated that the ST finished completely. In the heating process, the $\chi_M T$ values abruptly increased above 290 K. The $\chi_M T$ vs T curve in the heating process did not trace that in the cooling process, and the cooling and heating processed formed a hysteresis loop. The spin transition temperature ($T_c{\uparrow}$ and $T_c{\downarrow}$) were determined to be 303 K and 283 K, respectively.

1 ⊃ Liquid alkanes

After **1** was adsorbed liquid alkanes by vapor diffusion, the temperature dependence of the magnetic measurement was performed with first cooling from 320 K until 100 K and then heating from 100 K to 320 K. The magnetic behavior of **1** ⊃ Liquid alkanes exhibited hysteretic two-steps SCO which was different from **1**-GF (Fig. 5). As the size of alkanes increased, the T_c of **1** ⊃ Liquid alkane decreased. The details of the magnetic properties of each clathrate are described below. In the case of **1** ⊃ C_6H_{14}, the $\chi_M T$ value at 300 K is 3.54 emu K mol^{-1}, which is almost the same value as **1**-GF, and the $\chi_M T$ value remains constant until 210 K, where there is a rapid drop in the $\chi_M T$ value to 1.90 emu K mol^{-1}. This value remains constant until about 178 K where is a further rapid decrease in 0.17 emu K mol^{-1}, which closed to an expected value for the Fe^{II} ion in the LS state. In the heating process, two-steps spin state change was observed with hysteresis loop around 185 K and at 215 K. The hysteresis loops are 10 K in the first step and 12 K in the second step wide. The $\chi_M T$ value of **1** ⊃ C_7H_{16} at 300 K is 3.57 emu K mol^{-1}, the value remains constant until 200 K, where there is a rapid drop in the $\chi_M T$ value to 1.92 emu K mol^{-1}. This $\chi_M T$ value remains constant until about 165 K where is a further rapid decrease in 0.19 emu K mol^{-1}. In the heating process, two-steps spin state change was also observed with hysteresis loop around 160 K and at 200 K. The hysteresis loops are 10 K in the first step and 13 K in the second step wide. The $\chi_M T$ value of **1**$\supset$$C_8H_{18}$ at 300 K is 3.58 emu K mol^{-1}, the value remains constant until 190 K, where there is a rapid drop in the $\chi_M T$ value to 2.02 emu K mol^{-1}. This value remains constant until about 140 K where is a further rapid decrease in 0.20 emu K mol^{-1}. In the heating process, two-steps SCO was confirmed with hysteresis loop around 150 K and at 190 K. The hysteresis loops are 8 K in the first step and 19 K in the second step wide. The small loop observed in the high temperature region of **1**$\supset$$C_6H_{14}$ and **1**$\supset$$C_7H_{16}$ is considered to be the influence of partial desolvation of guest molecules in the pore. These results indicate that the behavior of alkanes confined in the pore affect the magnetic properties of the framework. In order to elucidate the mechanism of two-steps SCO, it is necessary to measure single crystal X-ray diffraction of the clathrates at each temperature and focus on the behavior of guest molecules such as spatial arrangement in the pore.[35]

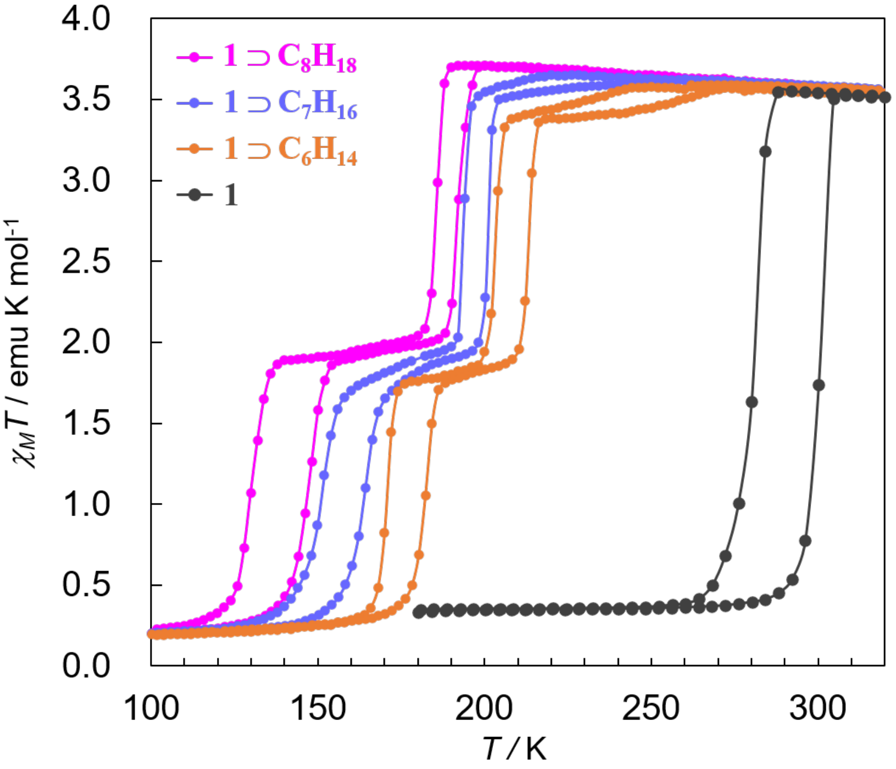

Fig. 5 $\chi_M T$ *vs* T plots of **1**-GF (gray), **1**$\supset$$C_6H_{14}$ (orange), **1**$\supset$$C_7H_{16}$ (blue) and **1**$\supset$$C_8H_{18}$ (pink) in the range of 320-100 K.

Responsivity of Gaseous alkene for 1

The adsorption and desorption isotherms of alkanes for **1** were performed in absolute pressure range of 3.0×10^{-2} to 100 kPa using activated sample by heating at 403 K and vacuuming for 6 hour**s**. Compound **1** exhibited reversible type I adsorption isotherms at 298 K. (Fig. 6(a)). The amount of adsorption of alkanes instantly reached about 1.0 molecule per 1 unit, and maximum adsorption amount of CH_4, C_2H_6, C_3H_8 and C_4H_{10} was 0.329, 1.128, 1.091 and 1.001 molecule per 1 unit at 100 kPa, respectively. This shows the adsorbed amounts of alkanes depend on the alkyl chain length, which was also observed with $\mathbf{1}\supset$Liquid alkanes. Because most gaseous molecules such as O_2, N_2, H_2 and CO are not adsorbed in **1** due to weak interaction with the framework (Fig. 6(b)), this result means that **1** showed higher affinity for alkanes than other gaseous molecules at room temperature. Focusing on the low-pressure region (~ 1.0 kPa), the adsorbed amounts of alkane increases as the carbon number increases, which displays CH-π interaction effectively operates between the framework of **1** and alkanes confined in the pore (Fig. 6(c)).

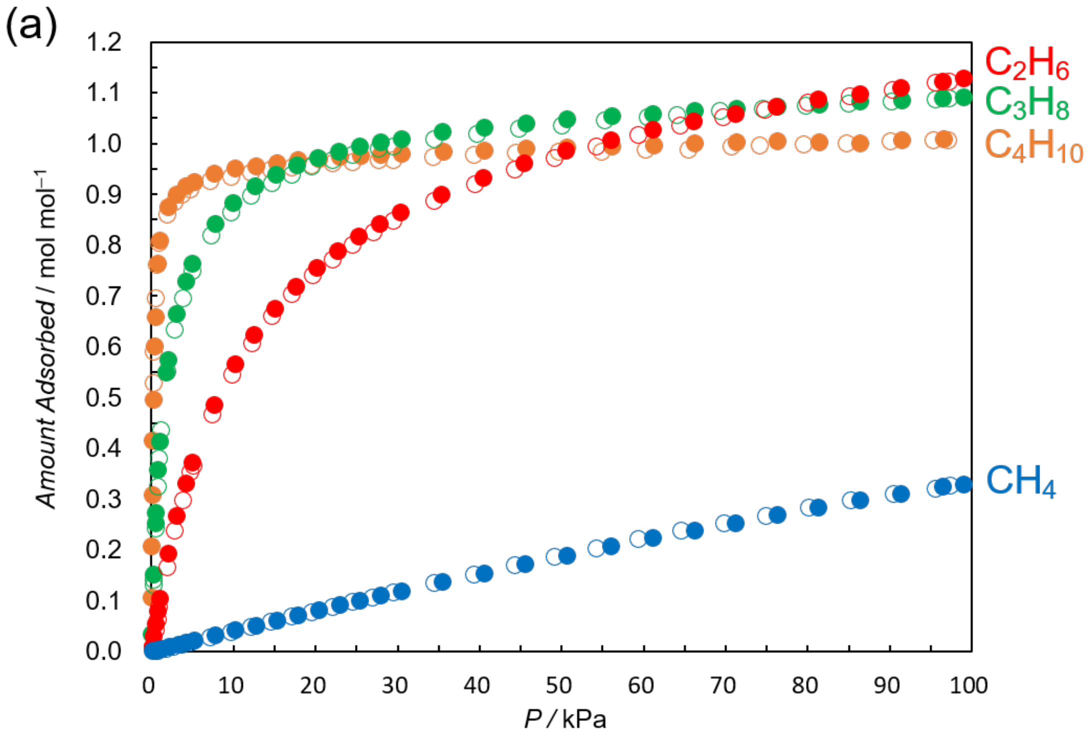

Fig. 6(a) Adsorption/desorption isotherms of **1** for CH_4 (blue), C_2H_6 (red), C_3H_8 (green) and C_4H_{10} (orange) at 298 K. The filled and open circles display the adsorption and desorption processes, respectively.

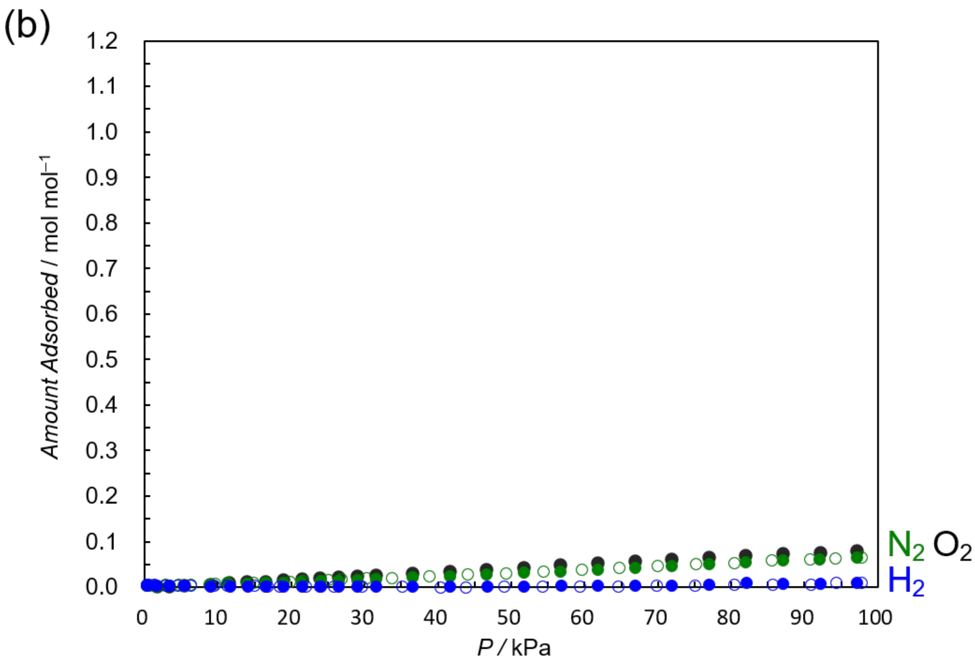

Fig. 6(b) Adsorption/desorption isotherms of **1** for H_2 (light blue), N_2 (light green), O_2 (black) and CO (brown) at 298 K. The filled and open circles display the adsorption and desorption processes, respectively.

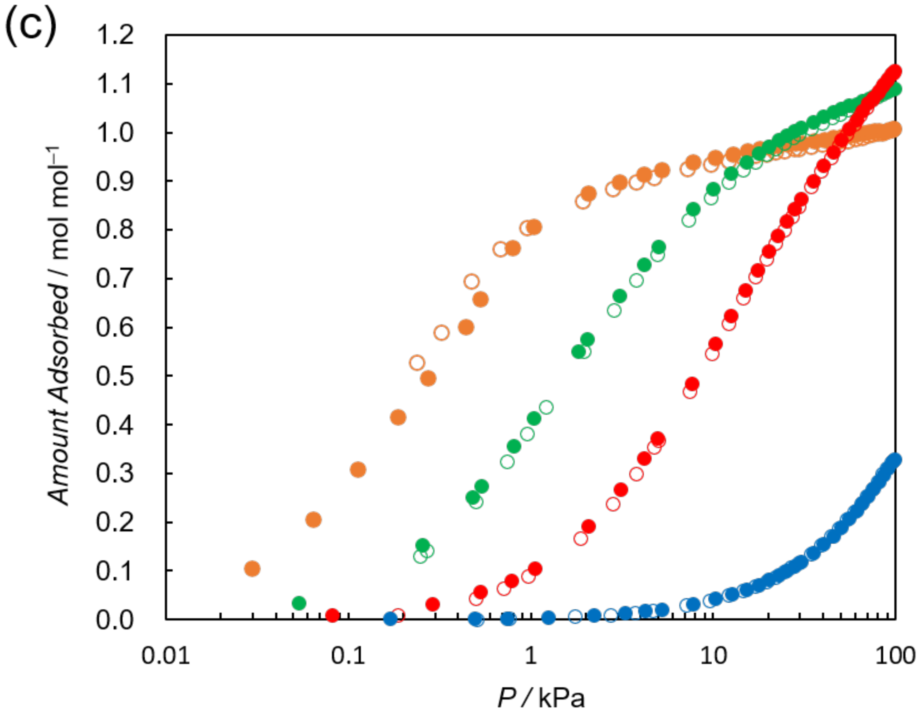

Fig. 6(c) Adsorption/desorption isotherms of **1** for CH_4 (blue), C_2H_6 (red), C_3H_8 (green) and C_4H_{10} (orange) in log scale at 298 K.

Activated **1** shows a cooperative ST behavior and a reversible color changes inside the magnetically bistable region ($T_\mathrm{c}^{\downarrow} = 283$ K, $T_\mathrm{c}^{\uparrow} = 304$ K). After activation of **1** by heating at 403 K over 6 hours, alkanes-responsivity of **1** was verified using an adsorption device (BELSORP-min II-PR). **1** in the LS state was showed smoothly color change from reddish purple to yellow with alkanes adsorption with 100 kPa at 298 K (Fig. 7), which suggests the ST from the LS state to the HS state. Thereafter, the magnetic responsivities of **1** for alkanes were investigated at 298 K through *in situ* magnetic measurement by using SQUID connected to the adsorption device (Fig. 8). The sample folder was fabricated from brass and the Pyrex glass, and a small amount of cotton was placed on the sample to prevent scattering. The magnetic susceptibility of **1** in the HS state did not change before and after alkane injection ((Fig. 9(a)). On the other hand, the $\chi_\mathrm{M}T$ value of **1** in the LS state rapidly increased and reached approximately 3.57 emu K mol^{-1} within 1 minute ((Fig. 9(b)). These results indicate the framework of **1** was stabilized in the HS state by uptaking alkanes. It is considered that the interaction between CH_4 and the framework of **1** is too weak, so that **1**$\supset CH_4$ did not show the ST at 298 K.

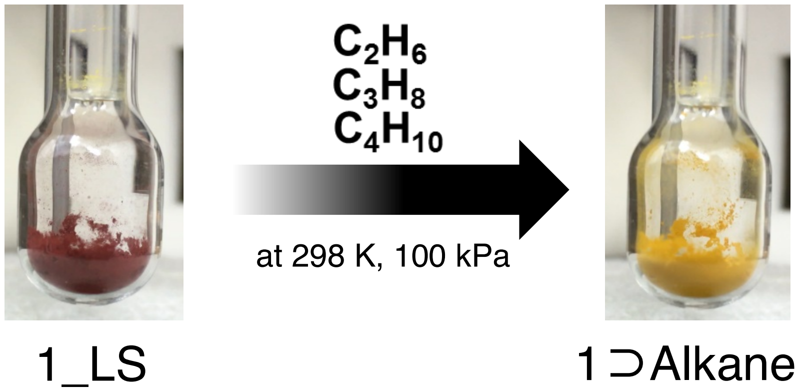

Fig. 7 Alkanes-responsivity of **1** for alkanes in the LS state at room temperature.

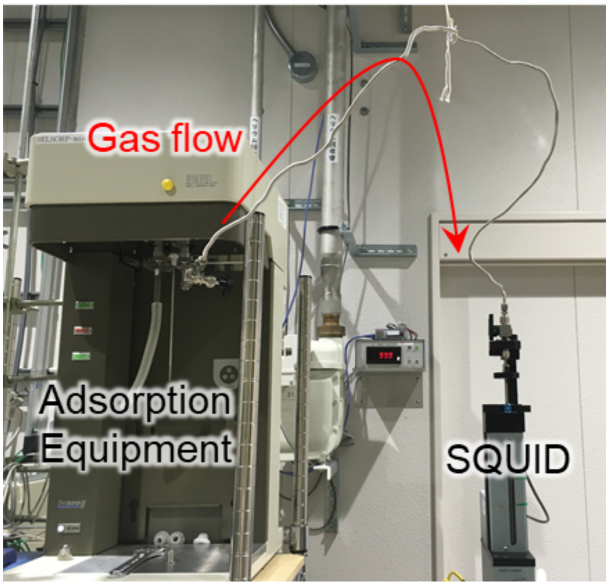

Fig. 8 *In situ* magnetic measurement system

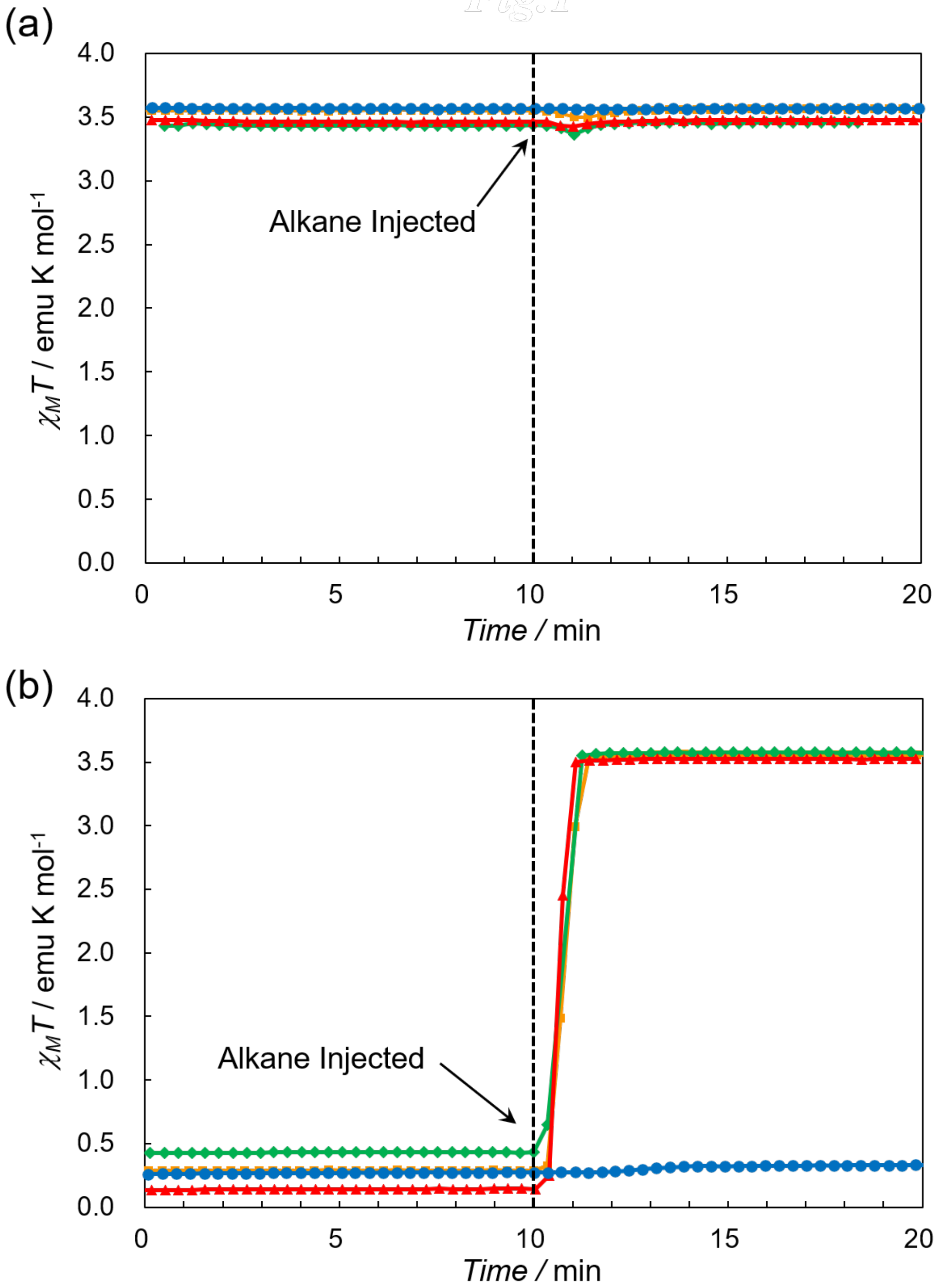

Fig. 9 Magnetic responsivity of **1** for CH_4 (blue), C_2H_6 (red), C_3H_8 (green) and C_4H_{10} (orange) in the (a) HS and (b) LS state.

The magnetic behaviors of **1**-GF and **1**⊃Gaseous alkanes are shown in Fig. 10-13 in the form of $\chi_M T$ vs. T plots. Temperature dependence of *in situ* magnetic measurement under gaseous alkanes (C_nH_{2n+2}; $n = 1 - 4$) was carried out after alkane injection at 298 K with first cooling from 298 K until 100 K and then heating from 100 K to 320 K. The **1**⊃Gaseous alkanes exhibited multi-step spin crossover behavior which was completely different from that of guest-free **1** except for CH_4, and their T_c decreased systematically enough to adsorb larger alkanes. The details of the magnetic properties of each clathrate are described below.

1⊃CH_4

The magnetic behavior of **1**⊃CH_4 was almost the same as **1**-GF because compound **1** hardly adsorbs CH_4. The ST temperature ($T_c^{\uparrow}$ and $T_c^{\downarrow}$) of **1**⊃CH_4 were determined to be 304 K and 280 K, respectively (Fig. 10).

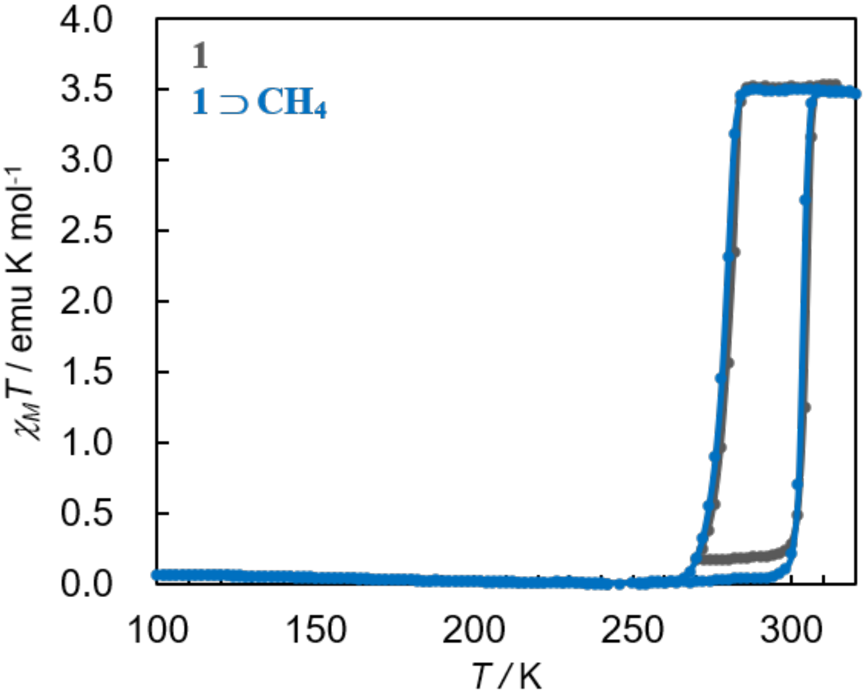

Fig. 10 $\chi_M T$ *vs* T plots of **1**-GF (gray) and **1**⊃CH_4 (blue) in the range of 320-100 K.

1$\supset C_2H_6$

1$\supset C_2H_6$ showed exhibited one-step spin state change in the cooling process; however, one-step increase of $\chi_M T$ value involving unique decrease in $\chi_M T$ value was observed in the heating process (Fig. 11). The $\chi_M T$ value at 298 K is 3.55 emu K mol^{-1}, which fall into the range expected for an Fe^{II} ion in the HS state. In the cooling process, the $\chi_M T$ value at 298 K remains constant until 170 K, where there is a rapid drop in the $\chi_M T$ value to 1.80 emu K mol^{-1} and this value remains constant until about 100 K. In the heating process, the $\chi_M T$ values abruptly increased above 265 K, and the $\chi_M T$ value at 280 K is 3.56 emu K mol^{-1}, which means the all Fe^{II} ions in the framework is HS state. In the heating process, the $\chi_M T$ value rapid drop around 188 K and reached 0.16 emu K mol^{-1} at 210 K. This value remains constant until around 250 K where there is an abrupt increase in the $\chi_M T$ value to 3.60 emu K mol^{-1} at 280 K, which indicated that the ST to the HS state finished completely.

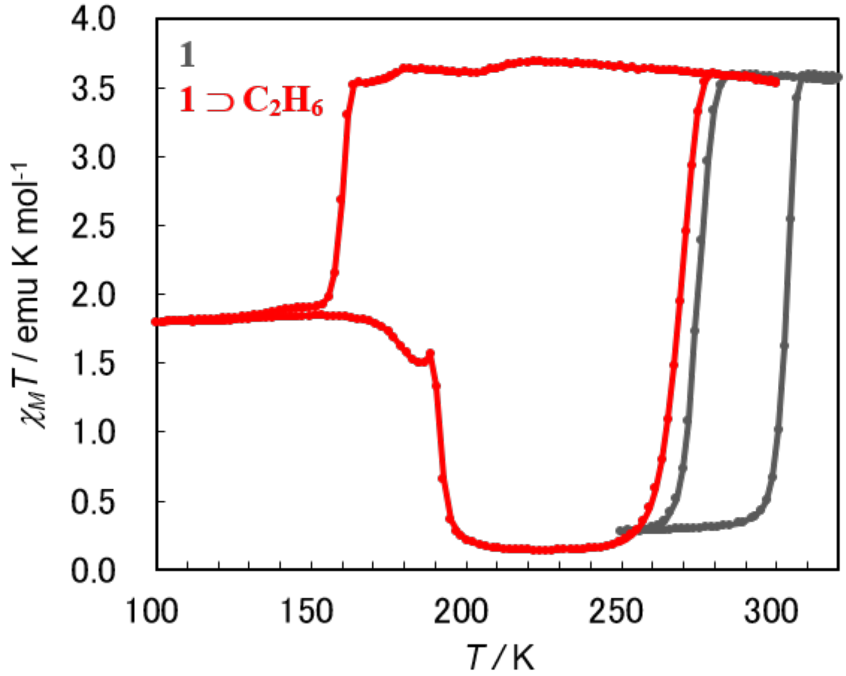

Fig. 11 $\chi_M T$ *vs* T plots of **1**-GF (gray) and **1**$\supset C_2H_6$ (red) in the range of 320-100 K.

The resultant unique decrease in $\chi_{\mathrm{M}}T$ value of **1**⊃C_2H_6 plausibly related to the change of concentration of C_2H_6 in the pore. Fig. 12 exhibited alkane adsorption and desorption isotherms at 298 K and 184 K (C_2H_6), 231 K (C_3H_8) and 273 K (C_4H_{10}). The adsorption amounts of C_3H_8 and C_4H_{10} were not changed with temperature; however, remarkable change of adsorbed amount was observed in C_2H_6. Hence, change in the density of C_2H_6 in the pore induced the unique decrease in $\chi_{\mathrm{M}}T$ value of **1**⊃C_2H_6 in the heating process (Fig. 13).

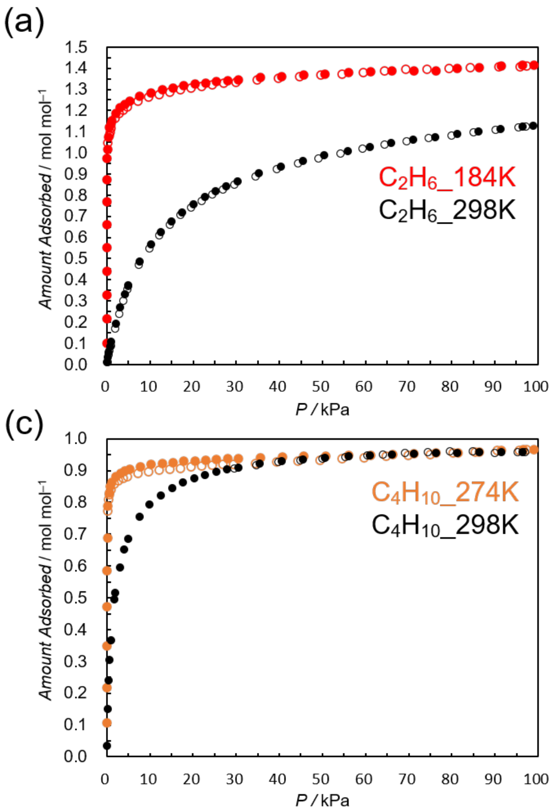

Fig. 12 Adsorption/desorption isotherms of **1** for (a) C_2H_6, (b) C_3H_8 and (c) C_4H_{10} at 298 K and low temperature.

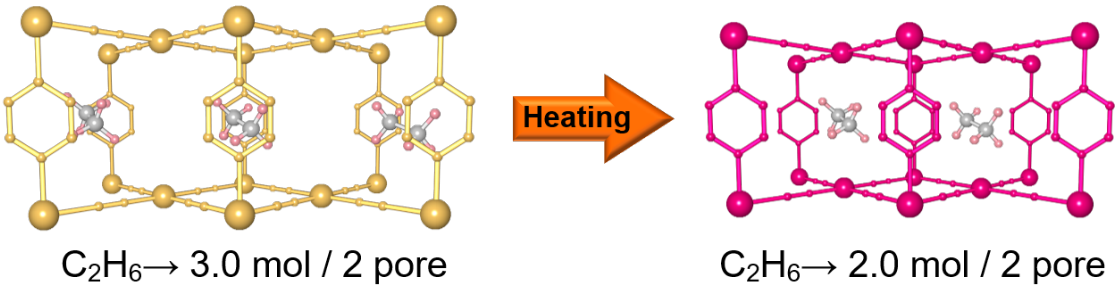

Fig. 13 Proposed mechanism of the change in the concentration of C_2H_6 in the heating process.

1$\supset$$C_3H_8$

The magnetic behavior of **1**$\supset$$C_3H_8$ was most complicated among **1**$\supset$Gaseous alkanes. **1**$\supset$$C_3H_8$ exhibited four-steps spin state changes in the cooling process. On the other hand, three-steps increase of $\chi_M T$ value including unusual phenomenon was observed in the heating process (Fig. 14(a)). The $\chi_M T$ value of **1**$\supset$$C_3H_8$ at 298 K is 3.53 emu K mol^{-1}. In the cooling process, the $\chi_M T$ value at 298 K remains constant until 210 K, where there is a rapid drop in the $\chi_M T$ value to 2.66 emu K mol^{-1} as a first spin state change. This value remains constant until about 195 K where is a further rapid decrease in the $\chi_M T$ value to 1.80 emu K mol^{-1} as a second spin state change. the $\chi_M T$ value at remains constant until 170 K, where there is a rapid drop in the $\chi_M T$ value to 0.97 emu K mol^{-1} as a third spin state change. This value remains constant until about 145 K where is the last rapid decrease in 0.15 emu K mol^{-1}, which indicates that the ST finished completely. In the heating process, two-steps spin state change was observed with hysteresis loop around 155 K and at 180 K. The hysteresis loops are 15 K in the first step and 16 K in the second step wide. After the increase in the $\chi_M T$ value of the second step, an unique phenomenon that the $\chi_M T$ value decreases in the heating process was observed (inside the dotted frame of Fig. 14(a)). The $\chi_M T$ value at 185 K is 1.81 emu K mol^{-1}. This value remains constant until about 190 K where there is a rapid drop in the $\chi_M T$ value to 0.50 emu K mol^{-1}. It is considered that the physical properties of C_3H_8 such as size and phase transition affect the magnetic behavior of the framework because the $T_c{\downarrow}$ was near the boiling point of C_3H_8 (231 K). This value remains constant until about 225 K where there is an abrupt increase in the $\chi_M T$ value to 3.50 emu K mol^{-1} at 250 K, which indicated that the ST to the HS state finished completely.

Furthermore, scan-rate dependence of *in situ* magnetic measurement of **1**$\supset$$C_3H_8$ revealed the increase in the scan rate induced a loss of decreasing part in the $\chi_M T$ value (Fig.14(b)), and generated new multiple spin states (each spin states were named as Phase 1-6 in Fig. 15). To discuss the resultant scan-rate induced spin states in terms of its energy diagram, Kissinger method was employed, leading that the activation energy for the process from Phase 3 to Phase 6 was roughly evaluated to be 28 kJ mol^{-1} (Fig.16(a)). Based on this analysis, the proposed energy diagram involving the Phase 1-6 is shown in Figure 16(b). In the slow scan rate, Phase 4 does not form but Phase 6 generates instead, likely reflecting the large activation energy required for formation Phase 6 from Phase 3. Fast scan rate can not give the enough energy for the activation energy of 28 kJ mol^{-1}, resulting in the formation of kinetically stable Phase 4 rather than Phase 6. Thus, the scan rate acts as an important factor to determine the ratio of thermodynamically stable Phase 6 and kinetically stable Phase 4.

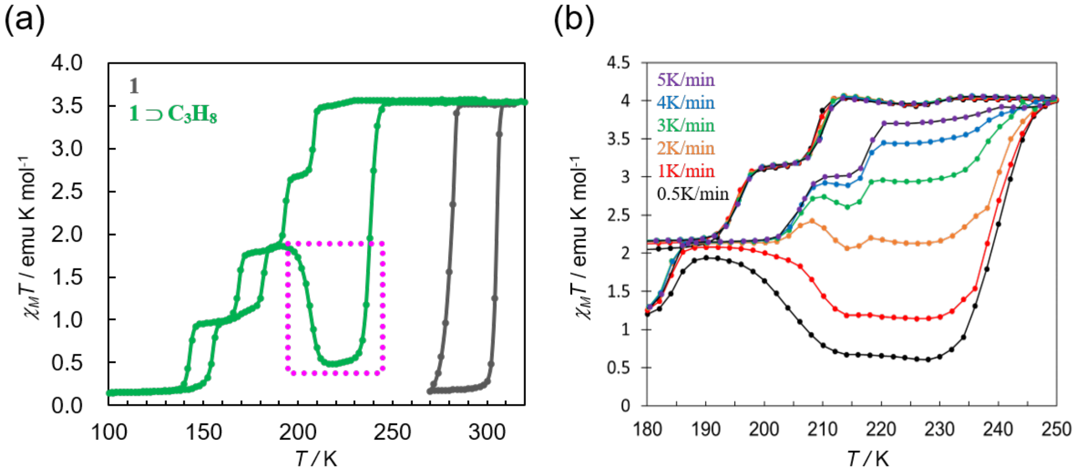

Fig. 14(a) $\chi_M T$ *vs T* plots of **1**-GF (gray) and **1**⊃C_3H_8 (green) in the range of 320-100 K. (b) scan-rate dependence of *in situ* magnetic measurement of **1**⊃C_3H_8 in the range of 0.5-5 K/min.

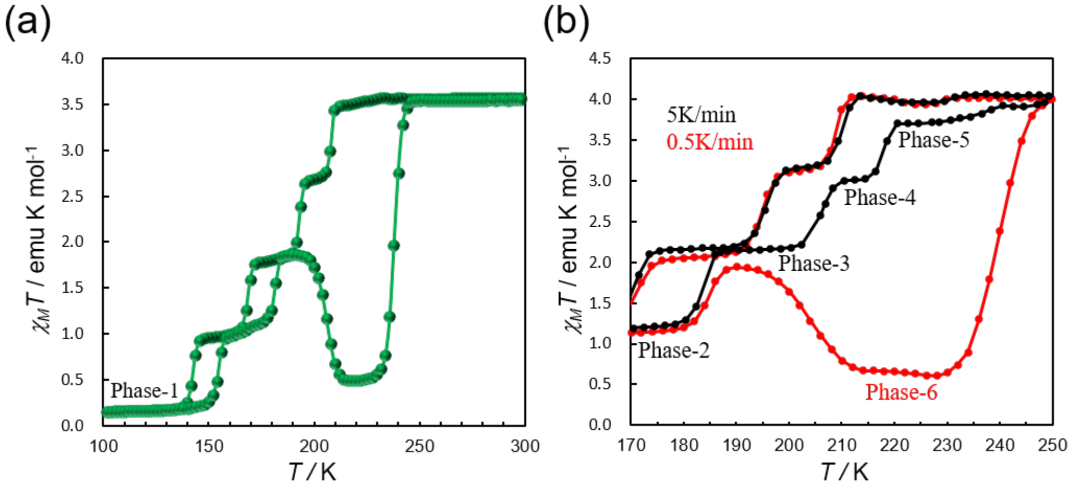

Fig. 15 $\chi_M T$ *vs T* plots of **1**-GF (gray) and **1**⊃C_3H_8 (green) in the range of (a) 320-100 K and (b) 250-170 K (scan-rate: 0.5 and 5 K/min.)

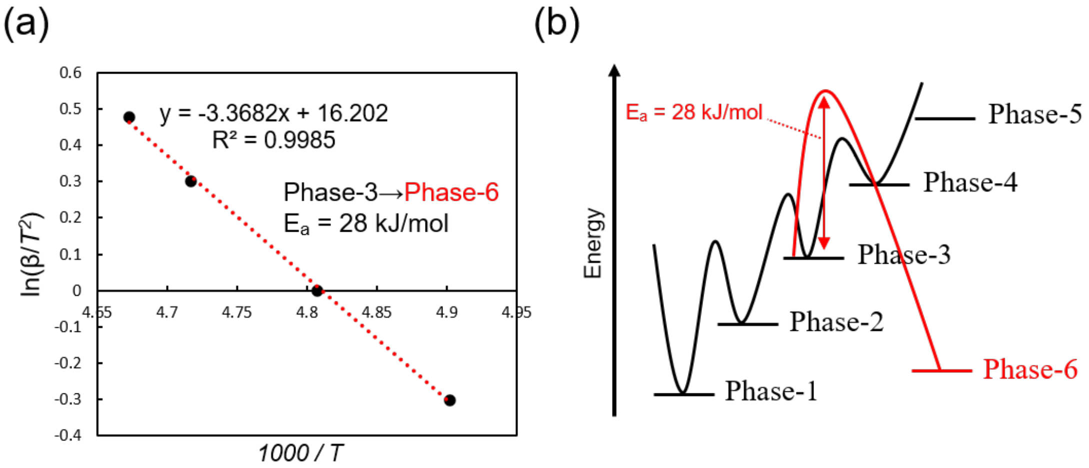

Fig. 16(a) Kissinger plots for the phase transition of Phase 3 → Phase 6. In the Kissinger method, β and T denote the heating rate and temperature, respectively. (b) An energy diagram involving Phase 1-6.

1⊃C$_4$H$_{10}$

The magnetic behavior of **1**⊃C$_4$H$_{10}$ is shown in Fig. 17**. 1**⊃C$_4$H$_{10}$ showed three-steps spin state changes in the cooling process, and two-steps spin state changes in the heating process, respectively. The $\chi_{M}T$ value of **1**⊃C$_4$H$_{10}$ at 298 K is 3.53 emu K mol^{-1}. In the cooling process, the $\chi_{M}T$ value at 298 K remains constant until 274 K, where there is a decrease in the $\chi_{M}T$ value to 3.43 emu K mol^{-1} as a first spin state change. This value remains constant until about 200 K where is a further rapid drop in the $\chi_{M}T$ value to 1.78 emu K mol^{-1} as a second spin state change. This value remains constant until about 148 K where is the last rapid decrease in 0.11 emu K mol^{-1}, which indicates that the ST to the LS state finished completely. In the heating process, two-steps spin state change was observed with hysteresis loop around 160 K and at 210 K. The hysteresis loops are 15 K in the first step and 19 K in the second step wide. The $\chi_{M}T$ value at 100 K is 0.11 emu K mol^{-1}. the $\chi_{M}T$ value remains constant until 150 K, where there is a rapid increase in the $\chi_{M}T$ value to 1.80 emu K mol^{-1} as a first spin state change. This value remains constant until about 200 K where is a further decrease in the $\chi_{M}T$ value to 3.56 emu K mol^{-1}, which indicated that the all Fe^{II} ions in the framework is HS state at this temperature.

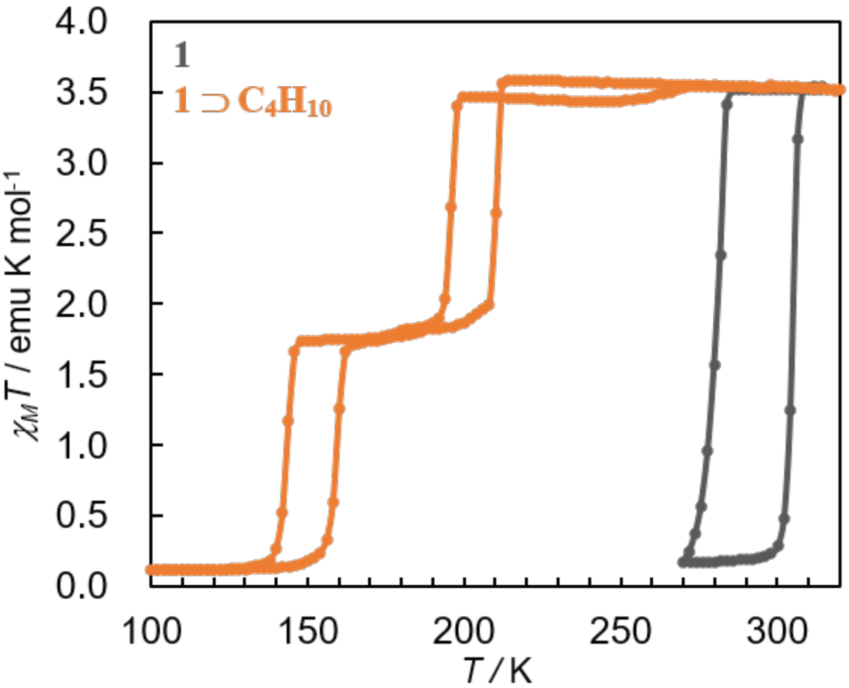

Fig. 17 $\chi_{M}T$ *vs* *T* plots of **1**-GF (gray) and **1**⊃C$_4$H$_{10}$ (orange) in the range of 320-100 K.

The resultant unique decrease in $\chi_M T$ value of **1**$\supset C_4H_{10}$ plausibly related to the order-disorder transition of C_4H_{10} in the pore with temperature change. The two-step SCO behavior has previously reported in this framework using furan molecules as a guest, which revealed that the change of location and arrangement of confined guest molecules induced the multi-steps spin state changes.[35] Also, similar magnetic behavior was observed in the liquid alkane clathrates (Fig.5), requiring additional measurement such as in situ single crystal XRD measurement.

Conclusion

In this work, we succeeded to create of multi-step spin state changes in a magnetically bistable Hofmann-type porous coordination polymer $\{Fe(pz)[Pt(CN)_4]\}$ (**1**) in association with alkanes adsorption (C_nH_{2n+2}; $n = 1 - 4$). At 298 K, the activated **1** displayed reversible type I adsorption isotherms, which suggests an effectively interaction between the framework of **1** and alkanes operates because **1** hardly adsorbs gaseous molecules at room temperature. Alkanes-responsivity and the magnetic behavior of **1** $\supset$ Gaseous alkanes were discussed based on *in situ* magnetic measurements and temperature dependence of magnetic susceptibility measurements. The $\chi_M T$ value of **1** in the low-spin (LS) state drastically increased at 298 K, which was also confirmed by *in situ* PXRD measurements. This means the high-spin (HS) state of **1** was stabilized by uptaking alkanes. Magnetic behavior of **1** $\supset$ Gaseous alkanes showed multi-step spin crossover which was completely different from that of guest-free **1**, and temperature dependence of *in situ* PXRD measurements revealed that the structural conversion is accompanied by the spin state change of the framework. In particular, **1** $\supset C_3H_8$ showed an extremely unique phenomenon that the $\chi_M T$ value decreases in the heating process. These results demonstrate that the approach of introducing gas molecules into magnetically-bistable host results in the construction of ST clathrates exhibiting unprecedented ST behaviors which cannot be obtained by conventional molecular approaches. Although the guest-responsivity in 3D Hofmann-type MOFs has been already reported by several groups including us, there are no reports that a creation of multiple stability induced by a synergistic effect between behavior of guest molecules and spin transition. This suggests that a significant effect of confined guest molecules cause interlocking of advanced physical properties of MOFs.

References

1. R. Kitaura, S. Kitagawa, Y. Kubota, T. C. Kobayashi, K. Kindo, Y. Mita, A. Matsuo, M. Kobayashi, H.-C. Chang, T. C. Ozawa, M. Suzuki, M. Sakata, and M. Takata, *Science*, 2002, **298**, 2358-2361.
2. O. M. Yaghi, M. O'Keeffe, N. W. Ockwig, H. K. Chae, M. Eddaoudi, and J. Kim, *Nature*, **2003**, 423, 705-714.
3. S. Kitagawa, R. Kitaura, and S. Noro, Angew. *Chem. Int. Ed.,* **2004**, 43, 2334-2375
4. G. Férey, *Chem. Soc. Rev.,* **2008**, 37, 191-214.
5. E. D. Bloch, W. L. Queen, R. Krishna, J. M. Zadrozny, C. M. Brown, J. R. Long, *Science*, **2012**, 335, 1606-1610.
6. T. Hu, H. Wang, B. Li, R. Krishna, H. Wu, W. Zhou, Y. Zhao, Y. Han, X. Wang, W. Zhu, Z. Yao, S. Xiang, B. Chen, *Nat. Comm.,* **2015**, 6, 7328.
7. I. Ahmed, S. H. Jhung, *Chemical Engineering Journal,* **2017**, 310 197–215.
8. B. Li, H. Wen, B. Chen, J. Phys. *Chem. Lett.,* **2014**, 5, 3468-3479.
9. M. L. Foo, R. Matsuda, Y. Hijikata, R. Krishna, H. Sato, Satoshi Horike, A. Hori, J. Duan, Y. Sato, Y. Kubota, M. Takata, S. Kitagawa, *J. Am. Chem. Soc.,* **2016**, 138, 3022−3030.
10. S. Kitagawa, K. Uemura, *Chem. Soc. Rev.*, **2005**, 34, 109-119.
11. S. Kitagawa, S. Noro, T. Nakamura, *Chem. Comun.*, **2006**, 7, 701-707.
12. M. O'Keeffe, M. Eddaoudi, H. Li, T. Reineke, O. M. Yaghi, *J. Solid State Chem.*, **2000**, 152, 3-20.
13. J. L. C. Rowsell, O. M. Yaghi, *Angew. Chem. Int. Ed.,* **2005**, 44, 4670-4679.
14. G. Férey, *Chem. Soc. Rev.*, **2008**, 37, 191-214.
15. E. Coronado, J. R. Galán-Mascarós, *J. Mater. Chem.,* **2005**, 15, 66–74.
16. S. Dorbes, L. Valade, J. A. Real, C. Faulmann, *Chem. Commun.,* **2005**, 69–71.
17. C. Faulmann, S. Dorbes, B. G. Bonneval, G. Molnár, A. Bousseksou, C. J. Gomez-Garcia, E. Coronado, L. Valade, Eur. *J. Inorg. Chem.,* **2005**, 3261–3270.
18. T. Verbiest, S. Houbrechts, M. Kauranen, K. Clays, A. Persoons, *J. Mater. Chem.,* **1997**, 7, 2175–2189.
19. O. R. Evans, W. Lin, *Acc. Chem. Res.,* **2002**, 35, 511–522.
20. S. Masaoka, D. Tanaka, H. Kitahata, S. Araki, R. Matsuda, K. Yoshikawa, K. Kato, M. Takata, S. Kitagawa, *J. Am. Chem. Soc.,* **2006**, 128, 15799–15808.

21. S. Bureekaew, S. Horike, M. Higuchi, M. Mizuno, T. Kawamura, D. Tanaka, N. Yanai, S. Kitagawa, *Nat. Mater.,* **2009**, 8, 831.
22. H. Ōkawa, A. Shigematsu, M. Sadakiyo, T. Miyagawa, K. Yoneda, M. Ohba, H. Kitagawa, *J. Am. Chem. Soc.,* **2009**, 131, 13516.
23. M. Sadakiyo, T. Yamada, H. Kitagawa, *J. Am. Chem. Soc.,* **2009**, 131, 9906.
24. G. J. Halder, C. J. Kepert, B. Moubaraki, K. S. Murray, J. D. Cashion, *Science*, **2002**, 298, 1762–1765.
25. M. Kurmoo, H. Kumagai, S. M. Hughes, C. J. Kepert, *Inorg. Chem.,* **2003**, 42, 6709–6722.
26. M. Kurmoo, *Chem. Soc. Rev.,* **2009**, 38, 1353–1379.
27. L. Cambi and A. Gagnasso, *Atti. Accad. Naz. Lincei.,* **1931**, 13, 809.
28. O. Kahn, C. J. Martinez, *Science*, **1998**, 279, 44-48.
29. A. Bousseksou, G. Molna ́ r, L. Salmon, W. Nicolazzi, *Chem. Soc. Rev.,* **2011**, 40, 3313–3335.
30. M. Nishino, K. Boukheddaden, Y. Konishi, S. Miyashita, *Phys. Rev. Lett.,* **2007**, 98. 247203.
31. J. A. Real, A. B. Gaspar, M. C. Munoz, *Dalton Trans.,* **2005**, 2062–2079.
32. P. Gutlich, A. Hauser, H. Spiering, *Angew. Chem. Int. Ed. Engl.,* **1994**, 33,2024–2054.
33. Malcolm A. Halcrow, *Chem. Soc. Rev.,* **2011**, 40, 4119–4142.
34. L. J. Kershaw Cooka, R. Mohammeda, G. Sherbornea, T. D. Robertsa, S. Alvarezb, M. A. Halcrow, *Coord. Chem. Rev.,* **2015**, 289–290.
35. D. Aravena, Z. A. Castillo, M. C. Muñoz, A. B. Gaspar, K. Yoneda, R. Ohtani, A. Mishima, S. Kitagawa, M. Ohba, J. A. Real, E. Ruiz, *Chem. Eur. J.,* **2014**, 20, 128647-12873.

Concluding Remarks

In this doctoral thesis, the author systematically studied on the guest responsive changes of physical properties in magnetic molecular clathrate based on metal-organic framework.

In Chapter 1, we described the rational design of cyanide-based amorphous MOFs $M[Ni(CN)_4]$ (**MNi**; M = Mn, Fe, Co) through regulating the water adsorption properties by changing the central metals. **MNi** exhibited an abrupt water adsorption behavior at a certain vapor pressure (P_{ads}). $L_{2,3}$- and K-edge XAFS analyses revealed that the P_{ads} for water adsorption is governed by the tetrahedral M^{2+} centers in amorphous **MNi**.

In Chapter 2, novel dianion-based porous magnets of type $[Ni^{II}(dmen)_2]_2[Fe^{III}(CN)_6](A)_{0.5}\cdot 7H_2O$ (dmen = 1,1-dimethylethylenediamine, A^{2-} = 1,5-anthraquinonedisulfonate ($AQDS^{2-}$) or = Azobenzene-4,4'-dicarboxylate ($AZDC^{2-}$)) were synthesized. These compounds possessed different packing structures depending on the pillar dianions, in which guest-selective gate-adsorption and vapor- or gas-driven magnetic phase conversion were observed owing to their flexible structures. The magnetic phases of these frameworks converted from antiferromagnetic and ferromagnetic phases because the antiferromagnetic interlayer interaction was canceled due to the expanding of interlayer distance.

In Chapter 3, we focus on a magnetically bistable Hofmann-type MOF of type $\{Fe(pz)[Pt(CN)_4]\}$ in association with alkanes adsorption. The alkane clathrates exhibited unprecedented multi-step spin state changes and which were completely different from that of guest-free compound. Moreover, scan-rate dependence of *in situ* magnetic measurement of C_3H_8 clathrate revealed the increase in the scan rate induced a loss of the $\chi_M T$ value decreasing part, and generated new multiple spin states, indicating that these magnetic behaviors are originated from the change in the density of alkane with temperature, dynamics of alkane, order-disorder transformation of alkanes in the pore.

These works highlight that unique guest responsivity of molecular clathrate based on functional MOFs toward expanded the concept of guest responsive spin state switching to the synergetic transition with coupling the spin transition and dynamics of confined guest molecules. This strategy using guest molecules as inherent variables would give a new dimension for designing responsive and functional molecular materials.

Acknowledgement

All the studies in this thesis have been conducted under supervision of Professor Masaaki Ohba from April 2016 to September 2021 at the Department of Chemistry, Graduated School of Science, Kyushu University.

The author would like to express the deepest appreciation to Prof. Masaaki Ohba for his guidance and encouragement. The author could progress in these studies owing to his clear direction. The author learned many things not only science but also philosophy and ethics from him.

The author would like to thank Associate professor Ryo Ohtani and Assistant Professor Benjamin Le Ouay. The author learned how to progress in research and write papers logically from them.

The author would like to thank Prof. Susumu Kitagawa, Prof. Hitoshi Miyasaka, Prof. Hiroki Wadati, Prof. Kunihisa Sugimoto, Dr. Ken-ichi Otake, Dr. Wataru Kosaka, Dr. Kohei Yamagami, Dr. Shogo Kawaguchi, Dr. Eisuke Magome, Dr. Hiroyuki Setoyama, Ms. Hirona Yamagishi for their kind support to progress in this research.

These studies are financially supported by JSPS Research Fellowships for Young scientists (No. 19J12589).

Finally, the author gives a special thanks to all members of Ohba group for their kind support.

Haruka Yoshino
Department of Chemistry
Graduate School of Science
Kyushu University
September 2021

List of Publications

1. "Coordination Geometry Changes in Amorphous Cyanide-Bridged Metal−Organic Frameworks upon Water Adsorption "
   H. Yoshino, K. Yamagami, H. Wadati, H. Yamagishi, H. Setoyama, S. Shimoda, A. Mishima, B. Le Ouay, R. Ohtani, M. Ohba
   Inorg. Chem., **2021**, *60*, 3338-3344.

2. “Guest-Selective and Reversible Magnetic Phase Switching in a Pseudo-Pillared-Layer Porous Magnet”
   H. Yoshino, N. Tomokage, A. Mishima, B. Le Ouay, R. Ohtani, W. Kosaka, H. Miyasaka, M. Ohba
   Chem. Commun., **2021**, *57*, 5211-5214.

Other Publications

1. "Regulation in Long-range Magnetic Ordering in 2-D Honeycomb Network of $[(NBu_4)][M^{II}Fe^{III}(ox)_3]$ (M^{II} = Mn, Fe, Co, Ni and Cu) Family "
   H. Ōkawa, A. Mishima, **H. Yoshino**, M. Ohba
   Chem. Lett., **2018**, *47*, 444-447.

2. 「ジアニオンを用いたダブルレイヤー型多孔性磁性体の CO_2 による磁気秩序相変換」
   芳野　遼
   Bull. Jpn. Soc. Coord. Chem., **2018**, *124*, 122-124.

3. "The Electronic State of Hydrogen in the α Phase of the Hydrogen-Storage Material $PdH(D)_x$: Does a Chemical Bond Between Palladium and Hydrogen Exist?"
   S. Dekura, H. Kobayashi, R. Ikeda, M. Maesato, **H. Yoshino**, M. Ohba, T. Ishimoto, S. Kawaguchi, Y. Kubota, S. Yoshioka, S. Matsumura, T. Sugiyama, H. Kitagawa
   Angew. Chem. Int. Ed., **2018**, *57*, 9823-9827.

4. "Vapor Switching of Luminescence Mechanism in a Re(V) Complex"
   K. Sasaki, H.Yamate, **H. Yoshino**, H. Miura, Y. Shimoda, K. Miyata, K. Onda, R. Ohtani, M. Ohba
   Chem. Commun., **2020**, *56*, 12961-12964.

5. "Host-guest Interaction Modulation in Porous Coordination Polymers for Inverse Selective CO_2/C_2H_2 Separation"
   Y. Gu, J. Zheng, K. Otake, M. Shivanna, S. Sakaki, **H. Yoshino**, M. Ohba, S. Kawaguchi, Y. Wang, F. Li, S. Kitagawa
   Angew. Chem. Int. Ed., **2021**, *60,* 11688-11694.

6. "Guest-tunable Excited States in a Cyanide-bridged Luminescent Coordination Polymer"
   K. Sasaki, **H. Yoshino**, Y. Shimoda, M. Saigo, K. Miyata, K. Onda, K. Sugimoto, H.Yamate, H. Miura, B. Le Ouay, R. Ohtani, M. Ohba
   Inorg. Chem., **2021**, *60*, 6140-6146.

7. “Crystalline assembly of metal-organic polyhedra driven by ionic interactions with polyoxometalates”
   B. Le Ouay, **H. Yoshino**, K. Sasaki, Y. Ohtsubo, R. Ohtani, M. Ohba
   Chem. Commun., **2021**, *57*, 5187-5190.

8. “A Cyanido-bridged Luminescent Coordination Polymer composed of Janus-type Layers and its Two-dimensional Negative Thermal Expansion”
   K. Sasaki, **H. Yoshino**, J. Kitano, B. Le Ouay, R. Ohtani, M. Ohba
   Chem. Lett., **2021**, *50*, 1577-1580.